Free-Surface Microflows and Particle Transport

Dissertation

zur Erlangung des akademischen Grades eines
Doktors der Naturwissenschaften,

vorgelegt der
Mathematisch–Naturwissenschaftlichen Fakultät
der Universität Augsburg

von

Michael Schindler

aus Basel

Augsburg, im April 2006

Erster Gutachter: Prof. Dr. Peter Hänggi
Zweiter Gutachter: Prof. Dr. Achim Wixforth
Dritter Gutachter: Prof. Dr. Roland Netz
Tag der mündlichen Prüfung: 29. Mai 2006

Im Andenken an meinen Vater,
der mir als Mensch und Wissenschaftler
ein Vorbild ist.

Contents

Appendices

1. Introduction

For theoretical and mathematical physics, the description of fluid flow has always been an important source of inspiration. Going back to the times of Maxwell, it has led to the field concept and thus made the description of electromagnetism possible. Then, in the twentieth century, the nonlinearity of the Navier–Stokes equation has given physicists and mathematicians a very hard time – which lasts until today. Still, a "mathematical theory which will unlock the secrets hidden in the Navier–Stokes equations"[1] is one of the famous Millennium Problems. During the past decades, complex fluids such as non-Newtonian polymer solutions have gained more and more interest, but this is by far not the last topic that the Navier–Stokes equation has inspired.

In recent years, microfluidic setups have fascinated many scientists (Squires and Quake, 2005; Stone and Kim, 2001; Stone et al., 2004). Microfluidics opens a door towards the physical and mathematical treatment of biological systems, ranging from details of polymer dynamics in flows (Schlagberger and Netz, 2005; Doi and Edwards, 1986) over the mechanics and flow in thin blood vessels and cells (Sackmann, 2004) up to creatures living and walking on water surfaces (Hu et al., 2003; Bush and Hu, 2006), to name only a few. Its potential use for miniaturising standard chemistry setups seems tremendous (see Stone and Kim 2001 and references therein). Using and understanding microfluidic systems in practice, however, often implies a change of paradigm. On typical length scales up to $100\,\mu$m, water does not behave as we are used to from everyday life. It appears to be viscous like honey, its interface with the surrounding air is stiff and hard such that one could walk on it like water a strider. And, last but not least, all movement is subject to fluctuations, leading to well-known phenomena such as Brownian motion.

A promising new technique for manipulating small amounts of water and other liquids has been developed recently by Wixforth et al. (2004). They actuate droplets of water with so-called *surface-acoustic waves* (SAWs) which are waves of mechanical elongation at the surface of a crystalline material, illustratively understood as a tiny earthquake. When such a wave comes into contact with water, it gets damped and gives rise to a streaming in the fluid. The photographs in Figures 1.1 and 1.2 give an immediate impression of the resulting flows. The driving force, which is caused by the SAW, gives rise to an internal streaming pattern, as is made visible in Figure 1.1. A strong SAW may deform and move the droplet as a whole, as is depicted in Figure 1.2.

---

[1] see e.g. http://www.claymath.org/millennium/Navier-Stokes_Equations/

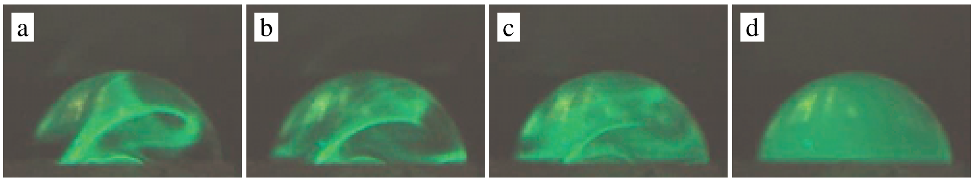

Figure 1.1. A resting water droplet, which is mixed by a weak SAW. The snapshots are taken at consecutive times from (a) to (d). The SAW approaches the droplet from the left and is damped by the influence of the viscous fluid. This gives rise to the internal streaming pattern. A spot of colour dye on the substrate is slowly dissolved and makes the flow visible. (Pictures from C. Strobl and A. Wixforth)

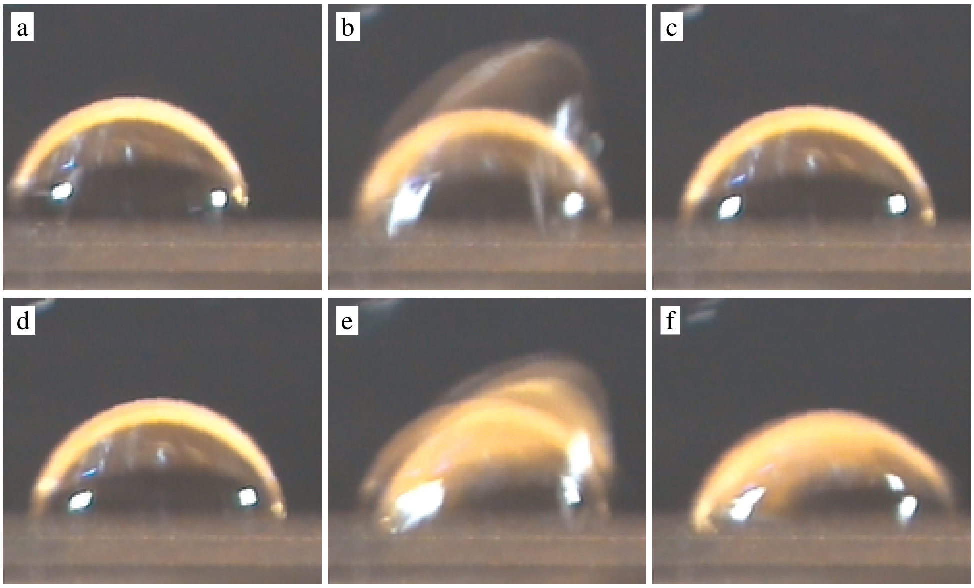

Figure 1.2. A "jumping" droplet containing 50nl of water, on a flat substrate. The photographs are taken at consecutive times from a film. Thus, several snapshots overlap in each picture. In the middle pictures (b) and (e), a powerful pulsed SAW arrives from the left and deforms it strongly. When the SAW is turned off, the droplet relaxes into its initial spherical shape at a slightly shifted position. (Pictures from C. Strobl and A. Wixforth, see also Wixforth et al. 2004)

This new manipulation method opens a wide range of applications and fundamental problems. Several lab-on-a-chip applications become realisable, such as the ability to transport, mix and separate droplets of some nanoliters volume, as well as the replication of DNA in small droplets, and more (see Guttenberg et al. 2004; Rathgeber et al. 2005; Sritharan et al. 2006; Strobl et al. 2004; Guttenberg et al. 2005; and http://www..advalytix.com). The experimental setup is accessible from many sides, which is convenient regarding both the injection of particles into the fluid and the observation of their motion. From a theoretical side, SAW-driven microflows imply several aspects raising fundamental questions, some of which remain unsolved already for several decades. The jumping motion of the droplet, as in Figure 1.2, might allow a closer look on the problem of a moving contact-line. What boundary condition is imposed on the flow at the substrate in the vicinity of the contact line? Does the droplet in Figure 1.2 glide, roll or rather jump – or is it a combination of all three motions? The driving mechanism by the SAW itself is not fully understood either. It is currently under investigation by the experimental physics group of A. Wixforth and the mathematics group of K. Siebert, see Gantner et al. (2006) for recent achievements. Another fundamental question concerns the thermodynamics of a fluid in motion, for which an equilibrium description is not applicable anymore. Such a fluid comprises fluctuating velocities and forces. Describing their statistical properties in the presence of boundaries, such as rigid immersed particles, is a demanding challenge. *Altogether, the present thesis will have to describe and to combine several interesting and important aspects of the microflows.*

The focus of the thesis is on the description of stationary SAW-driven microflows with free surfaces and the motion of particles therein. Different geometries of the fluid will be considered, such as droplets and water channels, confined partly by the flat substrate at the bottom, partly by free surfaces. For the actuation mechanism we will assume a qualitative characterisation of the acoustic streaming effect by the SAW. The very details of the SAW will not be treated here. The typical length scales of the systems is between ten an hundred micrometers. In such small systems, the boundaries tend to dominate the behaviour of the flow. Above all, we will confront ourselves with *free surfaces*, which introduce a nonlinearity and thus are considerably more difficult to treat than ordinary boundary conditions for viscous flow.

For the extensive specification of the flows in the mentioned geometries, *in Chapter 2* we will derive a numerical algorithm which is capable of calculating the shape of a curved free surface together with the surrounding flow causing the deformation. A key element of our analysis is the variational formulation of the equations describing both the flow and the geometry of the curved free surface. This formulation allows the derivation of an algorithm which is more stable than previously existing ones, due to the fact that the discrete representation of the free surface adapts some properties of a rubber band. A highlight of Chapter 2 will be the numerical solution of the flow inside a small droplet. The qualitative properties of its deformation yield an improved insight into the nature of the driving forces by the SAW.

In Chapter 3 we will use the numerically obtained free-surface flows to investigate their potential application concerning particle accumulation. The benefit of the free-surface numerics here is twofold. On one hand, the calculated velocity fields are utilised for the combined advective and diffusive transport of small particles. Here, we will focus on the effects by the boundaries on the accumulation of particles. On the other hand, what we have learned about the SAW from the droplet deformations, will prove useful to understand an accumulation effect in the volume. This effect is based on the different impacts of the velocity and the pressure fields on differently sized particles.

In the following sections of this chapter we will introduce those aspects of the SAW-driven microflows which are of most interest here. We start with the description of the flow, governed by free surfaces, and then qualitatively characterise the driving mechanism by the SAW. The third section of this chapter motivates a closer look on the ability of such microflows to generate directed transport of particles. The following two chapters then contain the detailed treatments of the free surface and of the particle transport.

1.1. The flow in microfluidic setups

Throughout this thesis, we will use tensor notation for fields in arbitrary curvilinear coordinates. This considerably simplifies the differential-geometric notation in Chapter 2, where the flow around curved free surfaces is described. For the formulation of the Navier–Stokes equations in curvilinear coordinates we refer to Aris (1989). Indices that are preceded by a comma denote covariant derivatives, and a repeated index that occurs both in co- and contravariant position is summed over. The metric tensor of the underlying coordinate system in space is denoted by g_{ij}.

1.1.1. The Stokes equations

The equation that describes a general flow of an incompressible fluid is known as the Navier–Stokes equation. It is a nonlinear equation in the velocity components, reading

$$\rho \partial_t v^i + \rho v^j v^i{}_{,j} = \sigma^{ij}{}_{,j} + f^i \,, \tag{1.1}$$

where v^i is the velocity field of the flow and ρ the mass density of the fluid. The stress that a fluid element experiences from its surroundings is given by the stress tensor σ^{ij}, and f^i is an externally applied body force that drives the flow. The stress tensor may be split into the isotropic contribution of the local-equilibrium pressure p and into a viscous part, containing the symmetrised derivatives of the velocity field,

$$\sigma_{ij} = -p g_{ij} + 2\eta e_{ij} \quad \text{with} \tag{1.2}$$

$$e_{ij} = \frac{1}{2}\left(v_{i,j} + v_{j,i}\right) . \tag{1.3}$$

The tensor e_{ij} is called the rate-of-strain tensor, and η denotes the viscosity. The condition for the fluid being incompressible is that the velocity is a solenoidal vector field, i.e. with zero divergence,

$$v^i_{,i} = 0 \,. \tag{1.4}$$

In microfluidics, the nonlinear term in the Navier–Stokes equation is often much smaller than the viscous term and can therefore be neglected. The validity of this approximation is better when the ratio of inertial forces and viscous forces, which is called the *Reynolds number*

$$\mathit{Re} := \frac{\rho \bar{v} \bar{x}}{\eta} \,, \tag{1.5}$$

is smaller. Here, $\bar{v}$ and $\bar{x}$ denote the typical scales of the velocity and of the length on which the velocity changes. Both are small in microfluidics. The length scale of velocity changes is smaller than the system size, between $10\,\mu$m and $100\,\mu$m. The typical velocity of the SAW-driven flow is found in the experiments to be between $10\,\mu\mathrm{m/s}$ and $1\,\mathrm{mm/s}$. This leads to Reynolds numbers between $Re = 10^{-4}$ and $Re = 0.1$. We will therefore omit the nonlinear term of the Navier–Stokes equation. Furthermore, the flow of water on the given length- and velocity scales is found to be overdamped. When the driving force f^i is switched off, then the flow ceases nearly immediately (Purcell, 1977). Below, the focus of the thesis will thus be reduced to stationary flows with vanishing Reynolds number, which are described by the stationary *Stokes equation*

$$0 = -p_{,i} + \eta v_{i,jk} g^{jk} + f_i \,. \tag{1.6}$$

We will refer to both equations, (1.4) together with (1.6) as the *Stokes equations*. The solutions of the Stokes equations exhibit several remarkable properties. One of them is that the flow is laminar and reversible. The streamlines of a laminar flow are locally straight and parallel. The global streamline pattern, however, may be complicated. Material lines of the fluid, when evolved together with the flow, may fold into even more complicated structures. If the sign of the flow is reversed, however, the complicated material lines will be restored to their initial shape. The overdamped behaviour of water on small length scales and the linearity of the Stokes equations have grave implications on small living organisms trying to propel themselves through the fluid. How life at small Reynolds numbers looks like, for example to bacteria, can be found in the illustrative survey of Purcell (1977, 1997).

Another property of the Stokes equations is that they may conveniently be split into independent equations for the pressure and for the velocity. In order to explain this concept, we make use of the Helmholtz–Hodge decomposition for vector fields and split the body force f^i into a conservative part, i.e. the gradient of a potential Φ, plus a non-conservative rest, i. e. the rotation of a vector potential, (cf. Abraham et al., 1988),

$$f_i = f_i^{(\mathrm{c})} + f_i^{(\mathrm{nc})} \quad \text{with} \quad f_i^{(\mathrm{c})} = -\Phi_{,i} \,. \tag{1.7}$$

The velocity field, which is solenoidal, yields only the rotatory part when it is decomposed in the same way. Accordingly, the Stokes equation is split into a gradient part and a rotatory part,

$$0 = -p_{,i} - \Phi_{,i} \quad \text{and} \tag{1.8 a}$$

$$0 = \eta \Delta v_i + f_i^{(\mathrm{nc})}. \tag{1.8 b}$$

The conservative part $f_i^{(\mathrm{c})} = -\Phi_{,i}$ and the non-conservative part $f_i^{(\mathrm{nc})}$ of the driving force are thus seen to cause very different effects. The first gives rise to a pressure field, while the latter drives the velocity field. Note that the decomposition (1.7) is not unique. Generally, if the force contains a so-called *harmonic* part which is both divergence-free and rotation-free, then it depends on the boundary conditions whether the force causes a pressure, a flow, or both. For example, a homogeneous gravitational force cannot drive any flow in a confined vessel, it is entirely compensated by the pressure gradient. In an unbounded domain, such as in a periodically continued fluid channel or in a thin film on an inclined surface, gravitation may cause a flow.

The fluid domain V may be bounded by rigid walls and by free surfaces. The Stokes equations (1.4) and (1.6) are complemented by boundary conditions at the different parts of the boundary ∂V. Both types of boundaries, rigid and free, coincide with material lines of the flow, consisting always of the very same fluid elements, which are stretched and contracted during their temporal evolution. In the direction normal to the boundary, the velocity field is then given by the velocity of the surface. This is the *kinematic* boundary condition, reading for an immobile surface,

$$N^i v_i = 0\,, \tag{1.9}$$

where N^i denotes the normal vector.

At sticky walls, also the velocity tangential to the surface is given by the velocity of the surface itself. This boundary condition is called *no-slip* condition. For immobile walls, it reads

$$T^i_{(\alpha)} v_i = 0\,, \tag{1.10}$$

where the vector $\mathbf{T}_{(\alpha)}$ is the αth tangential vector to the surface.

1.1.2. Flows with free surfaces

The shape of a free surfaces, which occurs in the microfluidic setups as well as in everyday life, is determined by a force balance. On one side, there is the stress which is exerted by a viscous fluid at its surface, reading $-\sigma_{ij}N^j$ for a normal vector pointing out of the fluid. The surrounding air is assumed to have vanishing viscosity compared to the fluid, thus providing the stress $-p_0 N_i$ only via the constant ambient pressure. Any difference between these two stresses must be caused by the surface tension γ of the free surface, yielding the stress balance

$$\sigma_{ij}N^j + p_0 N_i = \gamma\kappa N_i + \gamma_{,\alpha} T_i^{(\alpha)}\,. \tag{1.11}$$

In the first term on the right-hand side, κ denotes the curvature of the free surface. This term accounts for the surface tension. The last term contains $\gamma_{,\alpha}$, which is the gradient of the surface tension along the surface. This term is responsible for so-called Marangoni instabilities, where temperature gradients deform a free surface and thus give rise to a flow. A detailed interpretation of all terms in the stress balance (1.11) are given below, in Section 2.2. The free surface may meet the walls in a *contact line*. There, additional requirements are to be met, such as a prescribed contact angle, or the position of the contact line. In the latter case, the contact line is *pinned*.

The description of free-surface flows differs in one important aspect from flows in confined channels and from unbounded flows. Usually, differential equations like the Navier–Stokes equations are to be solved in a prescribed volume. For free-surface flows, the determination of this volume is part of the problem. We have to solve an equation in a volume that depends on the solution of the equation. Of course, the equations in the volume, together with the boundary conditions can be reformulated in non-Cartesian reference coordinates, such that they are to be solved in a given set of these new coordinates. The complication of this method is that these coordinates are unknown and themselves part of the problem. Since in general the free surface is curved, the coordinates are non-Cartesian, curvilinear coordinates. This makes both the Stokes equations and the boundary conditions strongly nonlinear in the coordinates, as can already be seen in the formulation of the Stokes equations (1.4) and (1.6). The metric tensor g_{ij}, which is simply the Kronecker symbol δ_{ij} when using Cartesian coordinates, depends quadratically on the derivatives of the old coordinates with respect to the new ones. The inverse tensor g^{ij} depends on the new coordinates in an even more complicated way. For reference see Aris (1989) or Section 2.2.1 below, where the same nonlinearity will be explicated for the metric tensor of the free surface.

For this reason, free-surface flows require advanced numerical methods. While the numerical treatment of viscous flow, bounded by rigid walls with an inflow region, and an outflow region, is a standard task which can be done with the help of commercially available software, it is more complicated with free-surface flows. The task of finding a stable numerical technique for free-surface flows can be summarised as the formulation of an algorithm which reduces the nonlinear occurrence of curvilinear coordinates as much as possible. However, these nonlinearities can never be avoided completely.

1.1.3. The microfluidic parameter regime of surface deformations

In the balance condition (1.11) for the stress at the surface, there are two independent sources of deformation, one is the pressure, the other is viscous stress. Their importance compared to the tension forces is measured by the *capillary number* and the *Bond number*,

$$Ca := \frac{\eta\bar{v}}{\gamma}\,, \tag{1.12}$$

$$Bo := \frac{\bar{f}^{(\mathrm{c})}\bar{x}^2}{\gamma}\,. \tag{1.13}$$

The latter is defined in a slightly more general way than usual, not only for a homogeneous conservative gravitation force but for arbitrary conservative forces. In a confined system with stationary boundaries and vanishing Reynolds number, we can make use of the rotatory part of Stokes' equation (1.8 b). The typical velocity scale is then expressed in terms of the non-conservative part of the driving force, namely $\bar{v} = \bar{x}^2\bar{f}^{(\mathrm{nc})}/\eta$. This allows an alternative definition of the capillary number similar to that of the Bond number,

$$Ca := \frac{\bar{f}^{(\mathrm{nc})}\bar{x}^2}{\gamma}\,. \tag{1.14}$$

The two dimensionless numbers *Ca* and *Bo* reflect the very different effects of the conservative and the non-conservative parts of the driving on the deformation of the free surface, respectively.

A third source of deformation is the gradient of the surface tension along the free surface. Except when dealing with the variational derivation of the free-surface stress-balance we will neglect these terms, assuming that the surface tension is a constant parameter. The surface tension is known to depend on the local temperature, but neither on the pressure nor on the velocity. We will not consider the temperature field in our calculations.

1.1.4. Limit of infinite surface tension

The free-surface flow problem comprises to sub-problems which cannot be solved independently. On one hand, the free-surface shape is to be determined, such that the flow can be calculated in the domain bounded by that shape. On the other hand, the surface is deformed by the flow. In the limit of an infinite homogeneous surface tension, however, these two sub-problems decouple. In this limit, the flow cannot deform the free surface any more. Already for a very large tension, or for an adequate external body force, both *Ca* and *Bo* are negligible. The stress balance at the free surface then reduces to the Laplace–Young condition with a constant pressure p,

$$-\,p + p_0 = \gamma\kappa\,. \tag{1.15}$$

The free surface thus has the same curvature κ everywhere. The combined problem of finding a stationary flow and the stationary position of the free surface now decomposes into two parts. First, the position and shape of the surface can be determined according to (1.15) together with the position of the contact line or the contact angles. The free surface is found to be a circle in two spatial dimensions. In three dimensions, a surface with constant curvature may be a sphere, but its shape generally depends on the shape of the contact line as well. After the surface has been determined, the flow field can be calculated.

To summarise the procedure here for later use also with smaller surface tension, the equation which determines the surface shape is the projection of the stress balance onto the *normal* direction. The remaining boundary conditions, the kinematic one together with the *tangential* projections of (1.11) are used for the flow field. These boundary conditions can also be regarded as *perfect-slip* boundary conditions, describing fluids which glide over a rigid wall without friction,

$$v^i\,N_i = 0\,, \tag{1.16 a}$$

$$T^i\,(v_{i,j} + v_{j,i})\,N^j = 0\,. \tag{1.16 b}$$

The tangential components of the normal stress must vanish, while the component in normal direction, reading $N^i\,\sigma_{ij}\,N^j$, is compensated by the wall to an arbitrary extent and does not appear in the boundary condition.

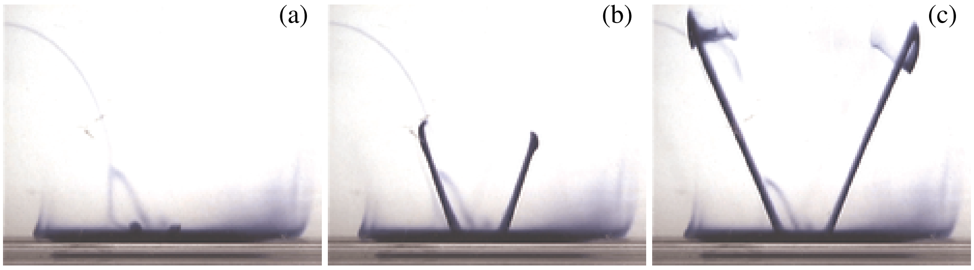

Figure 1.3. Two coloured fluid jets are caused by an inter-digital transducer at the bottom of a well which is covered by colour dye. The fluid is contained in a cuvette of the dimensions $54\text{mm} \times 10\text{mm} \times 23\text{mm}$. The part shown in the pictures is approximately $18\,\text{mm}$ wide. Between the snapshots, time spans of $0.16\,\text{s}$ and $0.48\,\text{s}$ have elapsed. The long and thin form of the coloured fluid fingers together with their growth direction strongly indicates that the direction in which the SAW forces the fluid coincides with the orientation of the fingers. The length scale on which the SAW-force decays appears to be several millimetres, which is long compared with the wavelength of the SAW. (Pictures from Z. Guttenberg and A. Wixforth.)

In Section 2.3.1 we will return to the question whether it is possible to determine a free-surface flow in two separate steps, namely finding the correct shape of the free surface and calculating the corresponding flow. There, the assignment of boundary conditions to the two sub-problems will pose the central issue of the numerical implementation. In order to show that there is not much hope to obtain free-surface flow fields analytically, Appendix A presents the analytical solution for the simple geometry of an infinitely long half cylinder. In this example, the fluid is bounded partly by a no-slip substrate, partly by a free surface in the limit of infinite surface tension.

1.2. Acoustic streaming

The considered microflows are driven by surface-acoustic waves (SAW). These are Rayleigh waves of a mechanical elongation at the surface of a crystalline material. The SAWs are emitted by so-called inter-digital transducers, which are structures of many interlaced parallel electrodes on a piezoelectric substrate. When an oscillatory voltage is applied to them, the inverse piezoelectric effect generates an initial deformation of the crystal surface, which then propagates on the surface away from the transducer (Strobl, 2001). As long as the SAW runs over the surface of the substrate, it is hardly damped. When it rushes into a water droplet, however, it looses energy while giving rise to an internal streaming pattern in the fluid. This mechanism is called *acoustic streaming*.

For a detailed description of the acoustic streaming effect, the works by Eckart (1948) and by Nyborg (1965) serve as a starting point. The general framework of their theories on acoustic streaming is the following. The effect takes place on two separate time scales. On the short time scale, which is determined by the frequency of the SAW, the motion of the interface between the substrate and the fluid is resolved. On this scale, water does not perform an incompressible flow but has to be described by the equations of *compressible* fluid dynamics which consider the mass-density of the fluid not as a constant but as part of the problem. Compared to the stress tensor (1.2) in the previously formulated Navier–Stokes equations, the stress then contains an additional term accounting for the compressibility. The condition (1.4) is replaced by an equation for the conservation of mass. A further equation of state relates density and pressure. The SAW, which is a wave on the substrate surface only, causes a sound wave running from the substrate into the fluid. This sound wave is subject to viscous damping along its path in the fluid. Furthermore, the nonlinear terms in the compressible Navier–Stokes equation give rise to higher harmonic pressure and velocity fields, oscillating at all multiples of the initial frequency. The emerging time-independent contribution is the wanted streaming velocity field which can be observed in the experiment.

There are typical time, length, and velocity scales in an SAW-driven system which are imposed by the SAW directly. These are the wavelength of the SAW ($23\,\mu\mathrm{m}$) and the period of its temporal oscillations ($7.5 \times 10^{-9}\,\mathrm{s}$). Other scales are given by the material constants, such as the sound velocities in the substrate (approx. $3.5 \times 10^3\,\mathrm{m/s}$) and in water ($1.5 \times 10^3\,\mathrm{m/s}$). Further scales follow from the reaction of the fluid on the SAW. They can only be obtained *a posteriori* from experimental observations. To be mentioned are the amplitude of the SAW (approx. $1\,\mathrm{nm}$), the damping length of the SAW under the fluid (approx. four wavelengths), the damping length of the sound wave in the fluid (several millimetres), and the typical velocity of the resulting stationary flow with magnitudes up to approximately $1\,\mathrm{mm/s}$.

From the frequency and the amplitude of the SAW one obtains the maximal velocity of the substrate surface as $0.5\,\mathrm{m/s}$. This velocity is at least three orders of magnitude larger than the typical stationary velocity, and three orders of magnitude smaller than the sound velocities of the materials. Thus, the velocity scales are clearly separated. The time scales are found to be separated even better, if one considers the generated streaming flow as truly stationary. The length scales, however, do not provide such a clear picture. The wavelength of the SAW and the length on which the SAW is damped by the fluid are both of the same order of magnitude as the system size. Only the amplitude of the SAW is several orders of magnitude smaller, and the damping length of the sound wave is much larger.

An important parameter for the theoretical description of the acoustic streaming effect is the Reynolds number of the velocity on the short time scale. It can be estimated by the above mentioned maximal velocity of the substrate surface together with the wavelength of the SAW as the typical length scale. This yields a value of $Re \approx 10$ for the fast velocities. The Reynolds number of the slow flow field can be estimated to be in the range of 10^{-4} to 0.1, where a velocity between $10\,\mu\mathrm{m/s}$ and $1\,\mathrm{mm/s}$ together with a typical length of $10\,\mu\mathrm{m}$ to $100\,\mu\mathrm{m}$ has been assumed, see also Section 1.1.1. The slow velocity field on the large time scale is therefore assumed to be a solution of the Stokes equations (1.4) and (1.6). The average flow performs an average motion just like an incompressible fluid, driven by an external body force. *This body force effectively describes the whole driving mechanism of the SAW.*

As candidates for a detailed explanation of the acoustic streaming effect in SAW-driven setups, the theories by Eckart (1948) and Nyborg (1965) have been considered. Both approaches have successfully been employed to describe acoustic streaming in other systems. They treat the viscous damping and the nonlinearities in the Navier–Stokes equation as small perturbations of an undamped acoustics. The undamped sound wave is described by the terms $\partial_t \mathbf{v}$ and ∇p in the Navier–Stokes equation, together with the equation for mass conservation. The terms $\eta \Delta \mathbf{v}$ together with its compressible counterpart account for the damping, and the nonlinearity is introduced by $\rho(\mathbf{v} \cdot \nabla)\mathbf{v}$. A dimension analysis with the typical scales in the system corroborate that both perturbations are small, compared to the undamped acoustics. On top of this requirement, both Eckart (1948) and Nyborg (1965) treat the nonlinearity as a much smaller perturbation than the viscous damping, which corresponds to a Reynolds number much smaller than unity, $Re \ll 1$. In contrast, we found this Reynolds number of the compressible flow on the short time scale to be $Re \approx 10$. Whether a more rigorous multi-scale analysis (according to the outline by Bender and Orszag 1978) of the problem is possible, cannot be judged here. A detailed numerical analysis of the problem is currently under consideration by Siebert et al. (see also Gantner et al., 2006).

In the discussions of free-surface flows and particle transport in the following chapters, we will require only a qualitative notion of the driving force by an SAW in order to describe the actuation. Figure 1.3 reveals the main features of this force. The three photographs were taken successively, from (a) to (c). We see that the flow pattern transports coloured dye in two finger-like structures from the bottom of the well into the volume. Although we cannot directly see the force which is acting here, it is apparently localised in two narrow channels. The width of the active region can be estimated from Figure 1.3 to be smaller than $0.3\,\mathrm{mm}$. Other experiments indicate that it is only about $70\,\mu\mathrm{m}$ wide. This width is mainly given by the damping length of the SAW under the fluid, but other parameters, such as the global shape of the water domain, might also have some impact. Its length is more difficult to estimate. Starting with picture 1.3b the colour fingers develop a mushroom-like form, indicating that the driving force cannot prevent the immediate back-flow of the fluid anymore. Thus, we are convinced that the driving force has not lost a significant part of its initial strength up to situation (b) of Figure 1.3. The length of the colour fingers in the respective photograph, namely $6\,\mathrm{mm}$, serves as an estimate for the decay length of the force which drives the flow. This is much larger than the typical system size of a microfluidic system.

It will be discussed in Chapter 3 that there is a difference between the velocity of the particles and that of the carrier media. In principle, it is not obvious that in Figure 1.3 we really see the flow of the water. Since the colour dye consists of particles which are extremely small, however, there should be indeed no sensible difference between the flow of the water and the flow of the colour dye.

For the chapters below, we thus arrive at the following qualitative picture of the driving force caused by the SAW. It is localised in a narrow channel and drives the fluid parallel to the main orientation of this channel. Its decay length in channel direction is at least comparable to the system size. Finally, the angle of the driving force may not be specified very well. As the pressure wave in the fluid may be reflected by the boundaries, this angle may depend on the global shape of the boundaries present.

1.3. Transport of small particles

One reason for the investigation of microfluidic systems is the hope to use specially designed flow patterns as a tool for particle transport. The ability to transport particles in a specified way opens the possibility to concentrate them in a certain region of the flow. A necessary prerequisite for such an accumulation is that the particle motion is different from the motion of the fluid. The particle trajectories should not coincide with the material lines of the flow. If the motion of a particle depends on a specific property of the particle, such as its size, its chirality or its aspect ratio, then we may expect different particles to react differently on a flow. Many applications are then possible. For example, if a flow exhibits far separated regions which attract particles with different properties, it is then possible to sort them. In case that there exists a narrow attractor for particles, it induces a local increase of the particle density, leading to an accumulation effect. Several mechanisms for such accumulation or separation techniques have been reported during the last years (Omurtag et al., 1996; de Gennes, 1999; Strook et al., 2003; Gorre-Talini et al., 1997; Marquet et al., 2002; Eichhorn et al., 2002; Eijkel and van den Berg, 2006; Huang et al., 2004). These methods employ various means of driving the microfluidic flows, some of which are miniaturised setups consisting of channels, pumps and valves, while others employ driving mechanisms that are adapted to the microfluidic parameter regime (Stone et al., 2004; Ajdari, 2000; Daniel et al., 2005; John et al., 2005).

In this thesis, we concentrate on an accumulation and separation method which is based on the thermal fluctuation in the fluid, namely the *drift ratchet* by Kettner et al. (2000). This system and possible modifications are introduced in the following paragraphs.

1.3.1. Particle transport in closed channels: the drift ratchet

An interesting fluidic device which is able to sort small spherical particles by their size is the *drift ratchet* (Kettner et al., 2000). This setup consists of many parallel thin channels in a silicon wafer. Such a channel is a few micrometers wide and is assumed to be infinitely long. Its diameter varies periodically in an asymmetric way as depicted in Figure 1.4a. An externally applied pressure gradient, which varies periodically in time, pumps water back and forth through these pores. Small particles, such as micro-beads are carried along by the flow, when they are immersed in the water. The particles and the fluid perform a motion back and forth through approximately two unit cells of the channel. In contrast to the average water flow which vanishes due to the periodic driving, Kettner et al. (2000) find that the average displacement of the particles grows with time. One reason for this effect is the asymmetry of the channel under spatial inversion. The average motion of a particle therefore depends on the orientation of the channel. Moreover, the average velocity of a particle depends on its size, exhibiting even opposite directions for differently sized particles. Thus, an efficient separation is achieved for specific pumping parameters. The central property of the drift ratchet, namely that the asymmetry of the pores causes a preferred drift direction of particles, has been verified experimentally for $0.32\,\mu$m-beads (Matthias and Müller, 2003; Matthias, 2002).

The conclusion that under far-from-equilibrium conditions, periodicity in combination with spatial asymmetry is generally sufficient for the manifestation of a systematic particle transport is well known as the *ratchet effect*. References on this and similar effects can be found in the works by Reimann and Hänggi (2002); Reimann (2002); Astumian and Hänggi (2002); Jülicher et al. (1997); Hänggi et al. (1990); Gammaitoni et al. (1998). The mentioned requirements are all satisfied in the *drift ratchet*. Standard ratchets are one-dimensional and employ an externally applied periodic potential as their driving. The form of this potential, which in many cases is taken as a sawtooth, has been named *ratchet shape*. The driving in the drift ratchet, however, is not due to a potential but due to the water flow. The shape of the channel boundary has some similarity with a ratchet shape. It has the same reflection asymmetry, but its influence on the particle transport is much more complex than that of an asymmetric force. Kettner et al. (2000) explain the ratchet effect as caused by the asymmetry of the shape of the channel in combination with the far-from-equilibrium situation created by the periodically alternating pressure gradient and thermal fluctuations. They propose an understanding of the particle current as a combined effect, comprising first the thermal diffusion of a particle between streamlines of different speeds, similar to the Taylor dispersion (Taylor, 1953), and second the collision of particles with the boundaries. For big particles, Kettner et al. (2000) suggest that many collisions with the asymmetric channel boundary take place, leading to a preferred motion in the direction in which the pore looks like a series of funnels (this is the direction from left to right in Figure 1.4a). For small particles, which tend into the opposite direction, the interplay of thermal and deterministic effects seems too complicated to allow an intuitive explanation.

A striking aspect of the drift ratchet and similar setups is that their sorting mechanism is based on the thermal fluctuations. An ordinary sieve strictly takes out particles bigger than a predefined size. Alternatively, with the aid of an electric field one may separate particles according to their charge. Such separating devices apply well-defined forces which act differently according to a specific property of the particles that are to be sorted. In the drift ratchet, however, it is the random noise itself which sorts the particles. This complicates its understanding considerably, but raises hope for promising new applications. Especially when soft material is to be sorted, mechanical and chemical sieving devices are prone to modify and damage the particles. A further aspect is that for conventional sieving techniques down-scaling is non-trivial. Thermal fluctuations, which are present all the time in small systems, make down-scaled sieving techniques inefficient. Sorting with the aid of this thermal noise thus appears as a promising alternative.

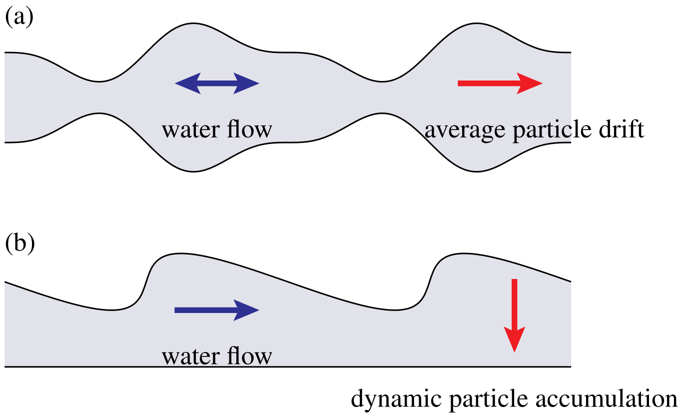

Figure 1.4. Panel (a) depicts the boundary shape of the drift ratchet. Panel (b) shows one alternative for the active region in the middle of an eight-shaped flow in Figure 1.5. Both shapes indicate two elementary cells which are meant to be periodically continued to the left and to the right. In the narrow channel of the drift ratchet (a), water is pumped back and forth. The resulting average drift of immersed particles is *parallel* to the main flow direction in the channel. In panel (b), the water flow is stationary, always in one direction. Particles are advected by the flow, mainly along the channel. In a periodically closed channel, however, a drift *perpendicular* to the main flow can be expected due to the asymmetry of the channel shape.

1.3.2. Particle transport in open channels

The major motivation of the present thesis is to deepen the understanding of the mechanisms of the drift ratchet and to explore the potential realisation of a similar effect in the SAW-driven microfluidic setups with free surfaces. From an experimental point of view, the “flat fluidics” with the SAW is preferable to the micro-pores in silicon. Pumping water through such thin pores requires extremely high pressures. The reason are the sticky channel boundaries, where the flow velocity vanishes. The highest velocity is found in the middle of the channel, but it cannot be very high since the boundaries are not far. Free surfaces are different in this respect. The velocities may be highest at the free surface, where the distance to the wall is greatest. It will thus be our aim in Chapter 3 to compare the different influences of free boundaries and sticky walls on the transport properties of particles.

In order to analyse the boundary effects of the particles, we consider the setup depicted in Figure 1.5, which has successfully been employed by Strobl et al. (2006) for sorting particles with the aid of electric forces. An eight-shaped wetting geometry is prescribed on a flat, otherwise non-wetting substrate. The form of the water channel over the wetting area of the substrate assumes the same form. The channel is kept together by the surface tension of the water–air interface. Two inter-digital transducers, located near two corners of the shape, emit SAWs which cause a stationary flow in the channel. The main flow direction follows the two loops of the eight-shape. In the middle part, where these two loops meet, the flow exhibits a family of streamlines starting and ending in stagnation points on the left and the right sides of the boundary. Since streamlines coincide with

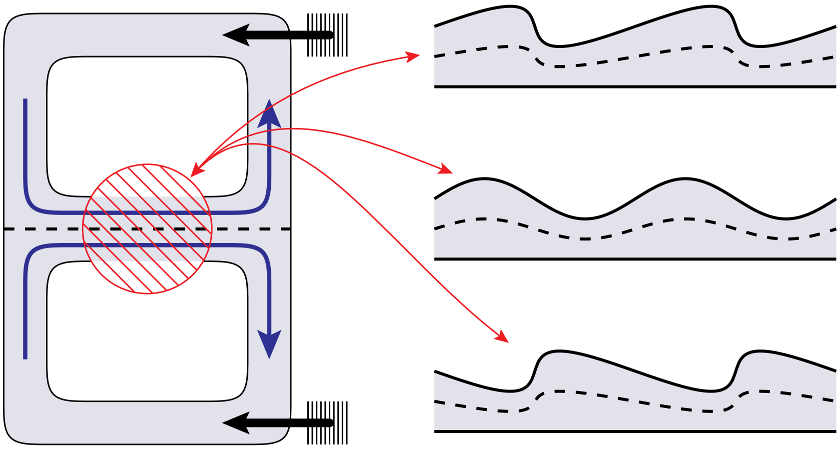

Figure 1.5. A schematic view on a microfluidic setup for sorting particles (Strobl et al., 2006). The sketch at the left side illustrates a water channel, shaped like the number 8, which is held in its form by prescribed wetting properties on the flat substrate. The channel is confined by the surface tension of the water–air interface. The water is driven by the SAWs which are emitted by the two inter-digital transducers illustrated as blocks of several parallel lines. The water streams along the two halves of the eight-shape and exhibits a family of streamlines which separate them. This defines two separate *basins* of water. Along the separating streamlines, which are indicated by the dashed line, these basins touch, thereby allowing immersed particles to transfer from one basin into the other. The probability of a particle to cross the separating streamline depends on the shape of the fluid channel in the region where the two basins meet. This region is marked with a hatched circle. Three different alternatives for the shape in the middle part of the channel are depicted at the right. The boundary shapes exhibit one straight and one curved boundary at the two different halves of the eight-shape. Due to this broken reflection symmetry we may expect particles to cross the separating streamlines, as indicated by the dashed curves. Two of the indicated shapes posses another broken reflection symmetry, similar to a ratchet shape. This may have additional effects on the separating properties of the channels.

material lines in stationary flows, these streamlines completely separate the fluid in the upper loop from the lower one. This defines two separate *basins* of water. Particles, when immersed in this flow, do not generally follow the streamlines and thus might be able to cross the separating streamlines and pass from one basin into the other. This leads to a *relative accumulation* of particles in one of the basins, if they were originally equally distributed.

The flow in the outer parts of the loops in Figure 1.5 is laminar. Nothing special happens to a distribution of particles, only thermal noise smooths the distribution a bit. The interesting part is the separating streamline in the middle of the eight-shape. This zone is marked by a hatched circle in Figure 1.5. In order to make particles cross the separating streamline, we have to make sure that they do not follow the streamlines completely. This will be achieved by using differently curved boundaries of the channel, as indicated in the right part of Figure 1.5. The influence of asymmetric boundaries on the particle transport is similar as in the drift ratchet. Since the boundaries are not symmetric under reflection, and since a far-from-equilibrium situation is guaranteed by the non-vanishing flow at room temperature, we may expect a reaction of particles on the boundary shape similar to the drift ratchet. A steady drift, however, cannot be expected. What we try to achieve is the transport *perpendicular* to the main flow direction, whereas in the drift ratchet it is *parallel* to it, see Figure 1.4. Because the water basins are confined in perpendicular direction, all we may expect is an *accumulation* of particles on one side. This accumulation will reach its steady state after a while, and the drift will fade.

2. Computing stationary free-surface flows

The detailed discussion of free-surface flows in non-trivial geometries, requires a numerical treatment. The present chapter contains the derivation of a numerical algorithm for computing flow patterns with stationary free surfaces, governed by the Stokes equations (1.4) and (1.6) together with the boundary conditions (1.9) and (1.11). For a numerical solution of these equations, we need to write them in a different form. This requirement is motivated in the first section, where the concept of finite-elements discretisation is introduced. In the following section, we proceed with the variational formulation of the equations in a continuous notation. Especially the physical nature of the stress balance (1.11) at the free surface needs an extensive treatment. As the free surface is curved, it becomes necessary to employ a differential-geometric description, which can then conveniently be used for the variation. A key element in the discretisation of the resulting continuous equations is a novel stabilisation technique for the computational mesh at the boundary. We find that a discretised free surface can partly be described as a rubber blanket. Such a description has the advantage that the mesh at the boundary is regularised automatically.

At the end of the chapter, we present numerical results in two spatial dimensions. As the main application, we consider SAW-driven droplets, which are pinned on the substrate and are deformed by their internal flow pattern. The form and the mechanism of the driving by the SAW is not known precisely, so that only qualitative properties can be obtained from the analysis of Figure 1.3 in Section 1.2. The numerical results, however, will allow a conclusion on the nature of the driving by the SAW.

2.1. Basic finite-element discretisation

Many different numerical approaches to solve the Navier–Stokes equations can be found in the literature (see Deville et al., 2002; Schwarz, 1986, 1991, to name only a few). Generally, the idea behind all of them is to reduce a partial differential equation together with its boundary conditions to a large system of algebraic equations. The solution vector of this system contains the *degrees of freedom* (DOFs) which parameterise a discrete approximation to the solution function of the differential equations. A *finite-element* discretisation $\widehat{u}$ of a function u is achieved using N node-based ansatz functions ϕ_d

together with the N-dimensional vector $\vec{u} = (u_1, \dots, u_N)$ containing the DOFs,

$$\widehat{u}(\mathbf{x}) = \sum_{d=1}^{N} u_d \, \phi_d(\mathbf{x}) \,. \tag{2.1}$$

The ansatz functions ϕ_d are defined on the elements of a computational mesh. Here, they are assumed to be unity at exactly one node of the mesh and to vanish at all others. This choice of the ansatz functions makes the DOFs u_d to be the solution values at the nodes of the mesh. Throughout this thesis, we will use first- and second-order approximating ansatz functions. They are either linear functions of the reference coordinates of the underlying element, or quadratic ones. The ansatz functions are smooth inside each element and continuous at their boundaries. Therefore, they yield a piecewise smooth continuous approximation of the solution function u. An overview over the commonly used types of finite elements can be found in the book by Deville et al. (2002).

In the finite-element method, a differential equation is solved only in a weak sense: The equations are *tested*, i.e. integrated together with a test function. An equation is then said to hold *in a weak sense* if the integrated equation holds for all elements of an appropriate set of test functions. The choice of the set of test functions plays a crucial role in the discretisation of a problem. If the test functions are chosen to be the ansatz functions, one refers to the *Galerkin* variant of the finite-element method. This variant is known to be the preferable method for differential equations which can be obtained as Euler–Lagrange equation of a known functional (Carey and Oden, 1986; Zienkiewicz and Taylor, 2000). As an illustration, we search for a stationary point of the functional

$$F := \int\limits_V \mathcal{F}\big(u(\mathbf{x})\big) \, dV(\mathbf{x}) \tag{2.2}$$

with respect to a variation of u. The function $\mathcal{F}$ is assumed to be smooth. The continuous Euler–Lagrange equation then reads

$$0 = \frac{\partial \mathcal{F}}{\partial u}\big(u(\mathbf{x})\big) \,. \tag{2.3}$$

The weak formulation of this equation coincides with the variation of F with respect to u,

$$0 = \delta F[\delta u] = \int\limits_V \frac{\partial \mathcal{F}}{\partial u}\big(u(\mathbf{x})\big) \, \delta u(\mathbf{x}) \, dV(\mathbf{x}) \,, \tag{2.4}$$

where δu denotes the test function. We compare the variation $\delta F[\delta u]$ with the variation of the discretised functional $\widehat{F}$, which is defined as the integral of $\mathcal{F}$, but which is evaluated at the discretised function $\widehat{u}$. Hence, the discretised functional is a function of the N-dimensional vector containing the DOFs, $\vec{u} = (u_1, \dots, u_N)$, and the variation in the Euler–Lagrange equation (2.4) is turned into a set of partial derivatives,

$$0 = \frac{\partial \widehat{F}}{\partial u_d} = \int\limits_V \frac{\partial \mathcal{F}}{\partial u}\big(\widehat{u}(\mathbf{x})\big) \, \phi_d(\mathbf{x}) \, dV(\mathbf{x}) \,. \tag{2.5}$$

The comparison of the continuous version (2.4) of the weak Euler–Lagrange equation with the discrete one (2.5) indicates that the ansatz functions ϕ_d adopt the role of the test functions δu. This equivalence between ansatz functions and test functions is the content of Galerkin's formulation of the finite-element method. The same is true for more general functionals $F(u, u_{,i})$ that also depend on derivatives of u. We then obtain the discretised Euler–Lagrange equations from their continuous form by means of the replacement

$$\delta u \mapsto \phi_d \,, \tag{2.6 a}$$

$$\delta u_{,i} \mapsto (\phi_d)_{,i} \,. \tag{2.6 b}$$

Below, we will make use of these replacement rules when discretising the update equation for the free-surface position and the Stokes equations.

In many applications a computer program is used to obtain a solution of the algebraic system of equations (2.5). If the continuous problem (2.3) is linear in the solution function, then (2.5) is linear as well and can be solved with standard iterative methods (Meister, 1999). A system of nonlinear algebraic equations requires more consideration which depends on the specific equations in question.

Imposing boundary conditions the natural way

One of the standard methods to account for boundary conditions in finite-element implementations is to use a conveniently weighted integral of the boundary condition over the surface. This integral occurs naturally from an integration by parts if the functional depends on the derivatives of the solution function. A simple example will elucidate the method. Consider the Poisson equation with Neumann boundary conditions,

$$\Delta u = f \quad \text{in } V, \tag{2.7 a}$$

$$\mathbf{N} \cdot \boldsymbol{\nabla} u = g \quad \text{on } \partial V. \tag{2.7 b}$$

In discretised form, after integration with a test function ϕ_d and integration by parts, (2.7 a) can be written as the set of equations

$$-\int\limits_V \boldsymbol{\nabla}\phi_d \cdot \boldsymbol{\nabla} u \, dV + \oint\limits_{\partial V} \phi_d \mathbf{N} \cdot \boldsymbol{\nabla} u \, dA = \int\limits_V f \, \phi_d \, dV \,, \tag{2.8}$$

where the index d runs over all degrees of freedom. In the *natural* implementation of the Neumann boundary condition, one replaces the above surface integral of the weighted left-hand side of (2.7 b) by the corresponding weighted integral of the boundary values g,

$$-\int\limits_V \boldsymbol{\nabla}\phi_d \cdot \boldsymbol{\nabla} u \, dV = -\oint\limits_{\partial V} \phi_d \, g \, dA + \int\limits_V f \, \phi_d \, dV \,. \tag{2.9}$$

Here, we have written the boundary integral on the right-hand side, indicating that it contributes to the equation for u as an inhomogeneity. A computer algorithm for the problem (2.7) has two options. It can either use the discretisation (2.8) for the Poisson equation in the volume and satisfy the boundary condition (2.7 b) by other means. Or it directly implements the natural discretisation (2.9) of the whole problem as a single system of equations. Certainly, the latter way is the preferable one.

This convenient way of implementing a boundary condition requires that a weak formulation of the problem in such a way that the terms involved in the boundary condition naturally appear in a weighted surface integral. A Dirichlet boundary condition, which specifies the values of u at the boundary, cannot be implemented in this way.

Concerning boundary conditions at a free surface, the question arises whether such a natural implementation exists. To give an answer to this question, we first need a weak formulation of the equations. It will be given in the next section. There, we will find the boundary integral over the normal stress,

$$\oint_{\partial V} \phi_d \, \sigma_{ij} N^j \, dA \,, \tag{2.10}$$

naturally occurring in the variational description of the Stokes equations. Therefore, a so-called *traction boundary condition*, namely

$$\sigma_{ij} N^j = g_i \quad \text{on } \partial V, \tag{2.11}$$

which imposes a certain stress g_i at the boundary, can be implemented in the natural way. The perfect-slip condition (1.16), however, cannot. It differs from the traction boundary condition in that the normal projection of (2.11) is not required. Instead, the kinematic boundary condition (1.16 a) is to be enforced. We conclude that the perfect-slip boundary condition for the given problem of an incompressible Stokes flow cannot be implemented in a natural way.

Previous work and other approaches to free-surface discretisations

Various numerical approaches for determining free-surface shapes have been proposed in the past. Their suitability for a given physical problem depends on the specific properties of the problem in question, such as the typical scales, whether the setting is time-dependent or not, and whether non-trivial driving forces are involved. In his PhD thesis, Brinkmann (2002) considers the stability of surface shapes in *static* situations, i. e. without flow. He utilises the program *surface evolver*[2] (Brakke, 1992) for minimising the free energies of the surface and of contact lines. Myshkis et al. (1987) provide a comprehensive survey of analytic methods and results, starting with free surfaces in static settings

---

[2] available on-line from http://www.susqu.edu/brakke/evolver/evolver.html

and continuing with small oscillations of ideal and viscous fluid shapes and self-gravitating liquids. Classical free-surface problems, such as the Stefan problem and Muskat's problem have been treated analytically and numerically by Crank (1984). He provides variational formulations and numerical techniques, not involving surface tension. Friedman (1982) treats the mathematics of free-surface flows, providing inequalities for classical problems such as the Stefan problem and fluidic jets. He does also not include the parameter regime of surface-tension dominated boundary shapes.

The numerical algorithms tackling the free-surface flow problem can roughly be classified into two groups: Either a fixed computational mesh is employed together with a function describing the position of the free surface, or the computational mesh is moved together with the fluid domain, yielding a sharp surface representation by element boundaries.

An established method of the first kind is the *continuum method*, proposed by Brackbill et al. (1992). They circumvented the discretisation of the stress-balance (1.11) by introducing a body force which is concentrated near the free surface. The body force incorporates the effect of surface tension. We have tested this method, which is implemented in the commercially available fluid-dynamics program *FLUENT* using a *volume-of-fluid* discretisation. For a macroscopic system this technique worked fine. When the system was scaled down to the microfluidic parameter regime, however, the method failed. In a simple test example, we found that approximation errors of the free-surface boundary condition contributed to the force balance in the Navier–Stokes equation and were amplified in an uncontrolled manner. The reason for the numerical errors lies in the discretisation near the free surface. As the surface is not discretised as a sharp boundary, the body force representing the surface tension is located not only on the boundary but must be smeared out. This typically gave rise to a spurious velocity field which even occurred when we started the iteration with the *known solution*. Problems with this method have also been reported by Renardy and Renardy (2002) and by Popinet and Zaleski (1999). Lafaurie et al. (1994) find the spurious velocities to be of the order of the ratio γ/η, which is the dominant velocity scale in microfluidic systems. Consequently, the existing continuum method appears to be inappropriate for the microfluidic parameter regime.

Another approach of the first kind has recently been proposed by Smolianski (2005). He uses finite elements and a level-set description for the free surface and calculates curvatures by derivatives of the distance function. Although his method employs a better discretisation than the above mentioned volume-of-fluid technique, he still encounters spurious velocity fields proportional to the ratio γ/η.

Methods of the second kind, representing the free surface by a sharp interface, are expected to work better in the microfluidic parameter regime. Algorithms of this class are often referred to as "moving mesh" or "ALE" (Hughes et al., 1981) methods and generally require more involved techniques, keeping the computational mesh feasible and not too distorted. The above mentioned *surface evolver* (Brakke, 1992) is one example of such an algorithm. Another technique of the second kind which has successfully been employed for tension-dominated free-surface problems is the boundary-element method

(Pozrikidis, 1992; Zinchenko et al., 1997). The dimensionality of the equations is reduced to the dimensionality of the surface, thus providing the basis for an efficient implementation. The method employs Green functions for the homogeneous Stokes equations, as will also be used in Chapter 3, and as is outlined in Appendix D. Unfortunately, the reduction of dimensionality can only be performed for Stokes equations with conservative body forces, that can be absorbed into the pressure term (Pozrikidis, 1992). In the present section, we allow for non-conservative body forces which are of particular experimental relevance concerning the driving by the SAW.

Pioneering works for the finite-element implementation of the full free-surface problem were published by Scriven and co-workers (Saito and Scriven, 1981; Kistler and Scriven, 1983; Scriven, 1960). They used spines to parameterise the movement of the computational mesh in coating flows and implemented Newton's method for a Galerkin approximation scheme. This work was later continued under the designation "total linearization method" by Cuvelier and co-workers (Cuvelier and Schulkes, 1990; Cuvelier et al., 1986). Their description requires a height function for the free-surface position, which makes it necessary to use well-adapted coordinate systems like polar cylindrical or spherical ones. Whether a finally obtained free-surface shape will overhang must be known in advance.

In the present chapter, we extend the works of Scriven and Cuvelier to arbitrary surface geometries. In our description, the parametrisation of the free surface is given directly by the boundary parametrisation of finite elements. Hence, neither spines nor a height function are needed. To properly take intrinsic curvatures of the free surface into consideration, all equations are formulated in a fully covariant form.

2.2. Variational formulation of the stress balance at a free surface

As stated above, for a finite-element discretisation we require a weak variational formulation of the free-surface flow problem with vanishing Reynolds number. In the following, this formulation will be derived in continuous notation with the aid of the calculus of variations. The discretisation will then be treated in the next section.

Especially the stress balance (1.11) is of concern here. It combines all variables of the problem, the pressure p, the velocity v_i, and some attributes of the surface itself, namely the curvature κ and the normal vector N_i. These variables generally have different ansatz functions. Thus, the question arises which ansatz functions should be used for testing the free-surface boundary conditions. In a continuous description, we will therefore search for a weak formulation of the stress balance as the variation of a functional.

Section 2.2.1 introduces the required aspects of differential geometry for a proper description of the curved free surface. This description allows us to express the right-hand side of the boundary condition (1.11) in weak variational form in Section 2.2.2. The

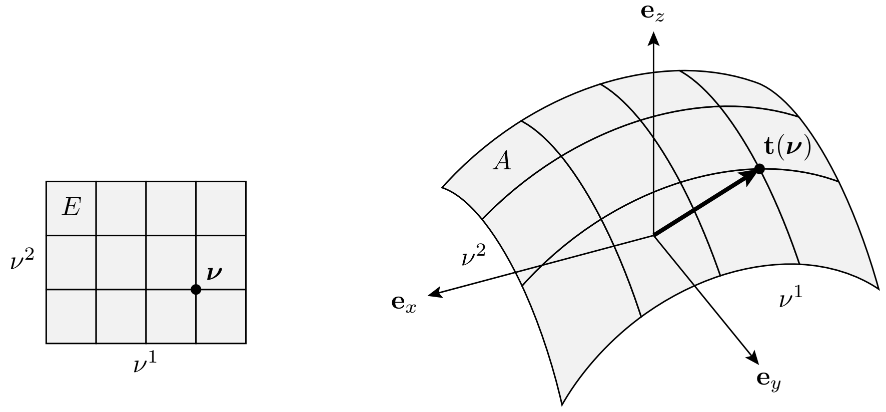

Figure 2.1. A sketch of the coordinate system on a two-dimensional surface A, which is embedded into three-dimensional space. The surface coordinates $\boldsymbol{\nu}$ are mapped from the reference domain E (left) onto the surface A (right) via the parametrisation vector $\mathbf{t}(\boldsymbol{\nu})$.

left-hand side then follows in Section 2.2.3. At this point of the derivation, the requested weak formulation of the stress balance is given by the equality of two different variations of two functionals. In Section 2.2.4 we then show that a combined variation in terms of a single functional encounters serious problems.

2.2.1. Differential geometry of a surface

A smooth surface in D-dimensional space may be parameterised by $D-1$ surface coordinates ν^α $(\alpha = 1, \dots, D-1)$ which determine the coordinates $t^i(\boldsymbol{\nu})$ of points on the surface in D-dimensional space. Both surface and space coordinates are illustrated in Figure 2.1. In the numerical studies below, we will restrict ourselves to $D=2$. The general framework, however, remains valid in higher dimensions $D \geq 2$. The surface coordinates $\boldsymbol{\nu}$ are taken from the parameter set $E \subset \mathbb{R}^{D-1}$. With $\boldsymbol{\nu}$ running through E, the whole free surface A is covered,

$$t^i \colon E \to \mathbb{R} \colon \boldsymbol{\nu} \mapsto t^i(\boldsymbol{\nu}) \,, \tag{2.12}$$

$$A = \{\mathbf{e}_{(i)} t^i(\boldsymbol{\nu}) \mid \boldsymbol{\nu} \in E\} \,. \tag{2.13}$$

Here, $\mathbf{e}_{(i)}$ is the ith basis vector in space. The connection between surface and space coordinates is described by the surface-derivatives of the parametrisation functions (cf. Aris, 1989, p. 215),

$$t^i_\alpha(\boldsymbol{\nu}) := t^i_{,\alpha}(\boldsymbol{\nu}) = \frac{\partial t^i}{\partial \nu^\alpha}(\boldsymbol{\nu}) \,. \tag{2.14}$$

Understood as a contravariant D-dimensional space-vector, the quantity $t^i_{,\alpha}$ represents the ith spatial component of the αth tangent vector $\mathbf{T}_\alpha$. At the same time, the mixed tensor $t^i_{,\alpha}$ is a covariant surface-vector. We will therefore omit the comma wherever it is not strictly necessary to indicate a derivative. The components of the metric tensor $a_{\alpha\beta}$

of the surface are obtained from the scalar products (in D-dimensional space) of the vectors $\mathbf{T}_\alpha$, reading

$$a_{\alpha\beta} = g_{ij}\, t^i_\alpha\, t^j_\beta\,. \tag{2.15}$$

The metric tensor $a_{\alpha\beta}$, its determinant $a = \det(a_{\alpha\beta})$, and its inverse $a^{\alpha\beta}$ are all nonlinear functions of the tangential vector components t^i_α. Their explicit forms for one- and two-dimensional surfaces are given in Appendix B. The normal vector of a two-dimensional surface is given by the normalised cross-product of the two tangent vectors,

$$N_i = \frac{1}{2}\varepsilon_{ijk}\,\varepsilon^{\alpha\beta}\, t^j_\alpha\, t^k_\beta\,, \tag{2.16}$$

where $\varepsilon_{\alpha\beta}$ and ε_{ijk} are the completely antisymmetric tensors in two and three dimensions, respectively. The change of the αth tangent vector along the surface in the βth direction is expressed by the covariant surface-tensor $b_{\alpha\beta}$ of the second fundamental form of the surface. This tensor therefore comprises second surface-derivatives of the parametrisation functions t^i,

$$b_{\alpha\beta} = t^i_{,\alpha\beta} N_i\,. \tag{2.17}$$

The trace of the tensor $b_{\alpha\beta}$ defines the curvature κ of the surface,

$$\kappa = a^{\alpha\beta} b_{\alpha\beta}\,. \tag{2.18}$$

By convention, the curvature of a sphere with outward pointing normal vector is negative.

2.2.2. The thermodynamic stress terms: without flow

In the particular case that only conservative forces $f^{(c)}_i = -\Phi_{,i}$ are involved, the fluid rests ($v^i = 0$) and can reach thermodynamic equilibrium with its environment. For this *static* system the terms in the stress balance (1.11) can consistently be formulated in terms of the minimisation of a free energy. The Stokes equation (1.6) reduces to $0 = -p_{,i} - \Phi_{,i}$ and is solved by

$$p(\mathbf{x}) = \Phi_0 - \Phi(\mathbf{x})\,. \tag{2.19}$$

The arbitrary offset Φ_0 of the potential will be set to zero in the following. Given the pressure, the stress balance (1.11) without viscous terms becomes

$$\mathbf{0} = (\gamma\kappa - p_0 - \Phi)\mathbf{N} + \gamma_{,\alpha}\mathbf{T}^\alpha\,. \tag{2.20}$$

This boundary condition can be obtained from a minimisation of the contribution to the free energy by the free surface A. The surface free-energy is given by the integral of the tension γ,

$$F_{(\gamma)} := \int\limits_A \gamma\, dA\,, \tag{2.21}$$

where dA denotes the infinitesimal surface area. Additionally, the volume V of the fluid has to stay constant. In order to take this condition into account, we introduce a

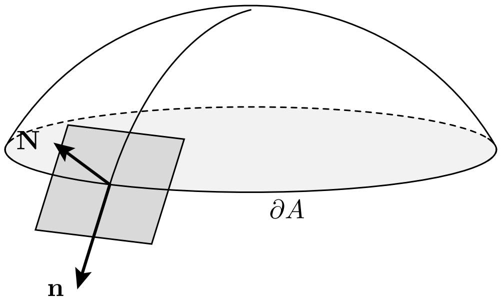

Figure 2.2. An illustration of the normal vectors $\mathbf{N}$ and $\mathbf{n}$. The vector $\mathbf{N}$ is orthogonal to the surface A, pointing out of the volume V, while $\mathbf{n}$ is orthogonal to the contact line ∂A and parallel to the surface. $\mathbf{n}$ points out of the free surface into the substrate.

Lagrange multiplier λ. Thus, we have the Euler–Lagrange equation for a minimal $F_{(\gamma)}$ with constant volume,

$$0 = \delta F_{(\gamma)}[\delta\mathbf{t}] + \lambda \delta V[\delta\mathbf{t}]\,. \tag{2.22}$$

The variation $\delta F_{(\gamma)}[\delta\mathbf{t}]$ expresses the change of $F_{(\gamma)}$ due to changes of the parametrisation vector $\mathbf{t}$. We will further use the notation $\delta F_{(\gamma)}/\delta t^i$, defined by the relation

$$\delta F_{(\gamma)}[\delta\mathbf{t}] =: \int\limits_A \frac{\delta F_{(\gamma)}}{\delta t^i} \delta t^i \, dA + \int\limits_{\partial A} \frac{\delta F_{(\gamma)}}{\delta t^i} \delta t^i \, dL\,, \tag{2.23}$$

where $\delta F_{(\gamma)}[\delta\mathbf{t}]$ is expressed in terms of δt^i only, and no surface-derivatives of δt^i occur. The integration over the boundary ∂A stems from an integration by parts over the surface. Since $\delta F_{(\gamma)}$ is a scalar, the quantity $\delta F_{(\gamma)}/\delta t^i$ must be a covariant vector in space. It is called the *Euler–Lagrange vector* (Lovelock and Rund, 1975).

The applied conservative body force $f_i^{(\mathrm{c})} = -\Phi_{,i}$ adds another term to the functional corresponding to the mechanical property of the system trying to minimise its potential energy

$$F_{(\Phi)} := \int\limits_V \Phi(x)\, dV = - \int\limits_V p(x)\, dV\,. \tag{2.24}$$

The Euler–Lagrange equations for minimising the free energy functional

$$F := F_{(\gamma)} + \lambda V + F_{(\Phi)} \tag{2.25}$$

consists of the terms $\delta F_{(\gamma)}[\delta\mathbf{t}]$, $\lambda\delta V[\delta\mathbf{t}]$, and $\delta F_{(\Phi)}[\delta\mathbf{t}]$. All three variations are performed by varying the parametrisation vector $\mathbf{t}$ of the surface. The calculation in Appendix B leads to the following terms, if $\mathbf{t}$ is varied only on the free surface and not on the rigid substrate:

$$\delta F_{(\gamma)}[\delta\mathbf{t}] = \int\limits_A \gamma\, t_i^\alpha \delta t_\alpha^i \, dA \,, \tag{2.26}$$

$$\delta V[\delta\mathbf{t}] = \int\limits_A N_i \delta t^i \, dA + \frac{1}{D} \oint\limits_{\partial A} \delta t^i (N_k t^k n_i - n_k t^k N_i) \, dL \,, \tag{2.27}$$

$$\delta F_{(\Phi)}[\delta\mathbf{t}] = \int\limits_A \Phi \, N_i \delta t^i \, dA = - \int\limits_A p \, N_i \delta t^i \, dA \,. \tag{2.28}$$

The boundary ∂A corresponds to the contact line where substrate, fluid, and air meet each other. The vector $\mathbf{n}$ in (2.27) is the tangential vector of the surface which is orientated normal to the contact line. This vector has surface components n^α and spatial components $n^i = t_\alpha^i n^\alpha$. Its orientation is defined such that it points into the substrate, as illustrated in Figure 2.2. In equation (2.26) we have used the mixed contravariant surface- and covariant space-vector t_i^α, which is defined as

$$t_i^\alpha := g_{ij} \, a^{\alpha\beta} \, t^j_{,\beta} \,. \tag{2.29}$$

The change of the surface free-energy (2.26) can be integrated by parts in order to remove the surface-derivative from the variation δt^i, see Appendix B for the details. Making use of the definition of the curvature (2.18), we obtain

$$\delta F_{(\gamma)}[\delta\mathbf{t}] = - \int\limits_A \gamma \, \kappa \, N_i \delta t^i \, dA - \int\limits_A \gamma_{,\alpha} t_i^\alpha \delta t^i \, dA + \oint\limits_{\partial A} \gamma \, n_i \delta t^i \, dL \,. \tag{2.30}$$

The surface-integrals from equations (2.27), (2.28), and (2.30) can now be collected to yield the stress balance in the static case,

$$\mathbf{0} = - \left. \frac{\delta F}{\delta \mathbf{t}} \right|_A = (\gamma\kappa - \lambda + p)\mathbf{N} + \gamma_{,\alpha} \mathbf{T}^\alpha \,. \tag{2.31}$$

Comparing this equation with (2.20), we find complete agreement if we identify the Lagrange multiplier λ with the ambient pressure p_0. The free-energy functional (2.25) can be rewritten in the usual thermodynamic form containing the pressure,

$$F = \int\limits_A \gamma \, dA - \int\limits_V p \, dV + p_0 \int\limits_V dV \,. \tag{2.32}$$

Note that the pressure $p(x)$ has been introduced already in the decomposition of the stress tensor (1.2) as a variable of local thermodynamic equilibrium. The form of (2.32), which essentially leads to $\delta F = \gamma \delta A - (p - p_0) \delta V$, corroborates this notion of the pressure.

2.2.3. The dynamic stress terms: viscous flow

The static terms in the stress balance have been reproduced in equation (2.31) by making use of the conservative part of the force. The remaining contributions to the Stokes equations, namely the viscous stress and the non-conservative forces, are still missing. We now recapitulate how these terms can be understood as the result of a variational principle. In a stationary system the temporal change of the kinetic energy at a point in the fluid due to *viscous dissipation* is (cf. Landau and Lifschitz, 1966)

$$\frac{d}{dt}\frac{1}{2}\rho v^2 = -2\eta e_{ij} e^{ij}\,. \tag{2.33}$$

The flow gains kinetic energy from the *external driving* at a rate

$$f_i^{(\mathrm{nc})} v^i\,. \tag{2.34}$$

In a stationary system that is bounded by rigid immobile walls, the variational principle which is attributed to Helmholtz and Korteweg (see Lamb 1932, p. 618 and von Helmholtz 1869) states that the Stokes equations yield those velocity and pressure fields that render the functional

$$P_{(\eta)} := \int\limits_V (\eta e_{ij} e^{ij} - f_i^{(\mathrm{nc})} v^i)\, dV \tag{2.35}$$

minimal. Note that the full external driving (2.34) is used, whereas only half of the dissipated power (2.33) enters the functional. Vice versa, the first variation of $P_{(\eta)}$ with respect to the velocity variable becomes

$$\delta P_{(\eta)}[\delta \mathbf{v}] = \int\limits_V (2\eta e^{ij} \delta v_{i,j} - f_i^{(\mathrm{nc})} \delta v^i)\, dV \tag{2.36}$$

$$= -\int\limits_V (2\eta e^{ij}_{,j} + f^i_{(\mathrm{nc})}) \delta v_i \, dV + \oint\limits_{\partial V} 2\eta e^{ij} N_j \delta v_i \, dA\,. \tag{2.37}$$

It vanishes for all variations of the velocity, if the integrands of the volume and of the surface contributions vanish separately. In this way, one recovers the rotatory part of the Stokes equation (1.8 b) and the viscous forces that are needed for the variational formulation of the free-surface stress balance (1.11). Now, we can write the full stress balance condition (1.11) in the form

$$\left.\frac{\delta P_{(\eta)}}{\delta \mathbf{v}}\right|_A = -\left.\frac{\delta F_{(\gamma)}}{\delta \mathbf{t}}\right|_A - \left.\frac{\delta F_{(\Phi)}}{\delta \mathbf{t}}\right|_A - p_0 \left.\frac{\delta V}{\delta \mathbf{t}}\right|_A\,. \tag{2.38}$$

This equation reveals that the two terms in the stress balance equation (1.11) have different physical origins. Both surface tension and pressure are of thermodynamic (or rather of thermo-“static”) nature, while the viscous stress originates from dynamic considerations. The right-hand side results from minimising the free energy, as in the static case. The left-hand side, however, stems from minimising a power. Formally, the static and dynamic origins are expressed by the different variations $\delta \mathbf{t}$ and $\delta \mathbf{v}$ in (2.38).

Both Stokes equations in variational form

Although the variational formulation (2.38) of the free-surface stress balance correctly displays the different physical origins of the dynamic and the static contributions, its derivation is not quite satisfactory. In order to explain this concern, we return to the role of the pressure. In (2.38) both pressure terms, namely $\delta F_{(\Phi)}$ and $p_0 \delta V$ appear on the static side of the variation. Nevertheless, it is likewise possible to obtain the pressure terms from a dynamic variation with respect to $\delta \mathbf{v}$. The functional

$$P := P_{(\eta)} + \int\limits_V (p_0 v^i_{,i} - p v^i_{,i} + \Phi_{,i} v^i)\, dV \tag{2.39}$$

$$= \int\limits_V \left[(p_0 g^{ij} - p g^{ij} + \eta e^{ij}) v_{i,j} - f^i v_i\right] dV \tag{2.40}$$

depends on both, pressure and velocity variables. The corresponding first variations are

$$\delta P[\delta p] = -\int\limits_V v^i_{,i} \delta p \, dV \,, \tag{2.41}$$

$$\delta P[\delta \mathbf{v}] = \int\limits_V \left[(p_0 g^{ij} + \sigma^{ij}) \delta v_{i,j} - f^i \delta v_i\right] dV \tag{2.42}$$

$$= -\int\limits_V (\sigma^{ij}_{,j} + f^i) \delta v_i \, dV + \oint\limits_{\partial V} (p_0 g^{ij} + \sigma^{ij}) N_j \delta v_i \, dA \,. \tag{2.43}$$

This variant of the variation is certainly preferable to the form of equation (2.37). It yields both Stokes equations in their weak form, the incompressibility condition, tested with δp in (2.41), and the balance of linear momentum, tested with $\delta \mathbf{v}$ in the volume integral of (2.43). It contains the full external driving force with its conservative and non-conservative parts. At the surface, it provides the whole normal stress, tested also with $\delta \mathbf{v}$. Instead of (2.38), the stress balance at the free-surface now reads

$$\left.\frac{\delta P}{\delta \mathbf{v}}\right|_A = -\left.\frac{\delta F_{(\gamma)}}{\delta \mathbf{t}}\right|_A \,. \tag{2.44}$$

Equation (2.44) gives an understanding of the equilibration mechanism. The system tries to minimise P by changing its velocity, competing against the surface tension in $F_{(\gamma)}$, which should also be minimal by changing the surface position. However, there is a mutual dependence of $\mathbf{v}$ and $\mathbf{t}$ via the kinematic boundary condition. Velocity and surface cannot be changed independently.

Consequences for the discretisation

If we assume a Galerkin discretisation of the equations (2.41) and (2.43), we then find that the incompressibility equation is tested with the ansatz functions of the pressure, and the Stokes equation with those of the velocity. A celebrated mathematical theorem, referred to as the inf–sup condition, or Ladyzhenskaya–Babuska–Brezzi (LBB) requirement, states that a stable discretisation is obtained if the incompressibility equation is tested with functions of one order less than the Stokes equation. Thus, in the framework of equations (2.41) and (2.43), this requirement means that the pressure has to be approximated one order less than the velocity variable. From a physical perspective, this is not astonishing because the pressure and the derivatives of the velocity together constitute the very same quantity, namely the stress tensor. In the numerical implementation below, we will use a first-order approximation for the pressure and a second-order approximation for the velocity.

The variation with respect to different variables in (2.44) poses a problem for the numerical implementation of the free-surface flow. There, a weak formulation of the problem will be required, which means that the stress balance (1.11) is integrated together with a test function. The question of the proper choice of test functions remains. The left-hand side of the stress balance (2.44) is naturally tested with $\delta\mathbf{v}$, leading to the surface-variation term $\delta v^i \sigma_{ij} N^j$ in equation (2.43). The right-hand side of equation (2.44), however, indicates testing with $\delta\mathbf{t}$, providing the term $\gamma\kappa N_i \delta t^i$, see equation (2.30).

In the discretisation, it is possible to circumvent this inconsistency of the weak formulation of the stress balance by using the same test functions for $\delta\mathbf{t}$ and $\delta\mathbf{v}$. On the level of a Galerkin finite-element implementation, this requires also the ansatz functions for the velocity field and for the surface parametrisation to be of the same order. It was stated by Bänsch (1998, p. 42, see also citations 49 and 50 therein) that a second-order approximation of the surface parametrisation yields a “good discrete curvature,” whereas a first-order one does not. The same can be seen below in Figure 2.5. We have now been able to substantiate Bänsch’s numerical observation with the underlying physical mechanism, namely the different physical origins of the terms in equation (2.44). The argument is similar to that of the LBB requirement for the approximation of the Stokes equations.

2.2.4. Completely dynamic formulation

With equation (2.44), we have obtained the stress balance condition at the free surface in terms of the variation of two different functionals. We now search for a combined functional which allows to express the boundary condition as a single variation. This search succeeds only partly. For the numerical treatment in the next section, we will therefore revert to the description (2.44) of the stress balance at the free surface. Nevertheless, the following rather technical aspects are of interest for a detailed understanding of the variational treatment of free surfaces.

In equation (2.44), the static and dynamic aspects of the stress balance are represented by the two variations with respect to $\delta\mathbf{t}$ and $\delta\mathbf{v}$. The physical dimensions of $\mathbf{t}$ and $\mathbf{v}$ differ by a time, and so do the dimensions of the free energy $F_{(\gamma)}$ and the power P. A combined description requires the variables to have equal dimensions. Consequently, we must either differentiate $\mathbf{t}$ with respect to the time, or integrate $\mathbf{v}$ over the time. As the Stokes equations directly follow from the variation δP in the volume, we do not modify P and $\mathbf{v}$, but rather consider the derivatives of $F_{(\gamma)}$ and $\mathbf{t}$ with respect to time.

The change of the free energy due to a free surface changing in time is expressed in terms of the parametrisation velocity $\dot{\mathbf{t}}$,

$$\dot{F}_{(\gamma)}(\dot{\mathbf{t}},\mathbf{t}) := \int\limits_A \gamma\, \dot{t}^i_{,\alpha}\, t^\alpha_i \, dA \tag{2.45}$$

$$= -\int\limits_A \gamma\kappa\, \dot{t}^i N_i \, dA - \int\limits_A \gamma_{,\alpha} t^\alpha_i \dot{t}^i \, dA + \oint\limits_{\partial A} \gamma \dot{t}^i n_i \, dL \,, \tag{2.46}$$

where an integration by parts yields the second identity (2.46). Both the normal and the tangential projections of the parametrisation velocity enter the functional $\dot{F}_{(\gamma)}$ via the terms $\dot{t}^i N_i$ and $t^\alpha_i \dot{t}^i$, respectively. With the aid of the full time-dependent kinematic boundary condition

$$v^i N_i = \dot{t}^i N_i \,, \tag{2.47}$$

the normal component of $\dot{\mathbf{t}}$ in (2.46) can be replaced by the normal component of the velocity field $\mathbf{v}$. We obtain a functional depending also on $\mathbf{v}$,

$$\dot{F}_{(\gamma)}(\mathbf{v},\dot{\mathbf{t}},\mathbf{t}) := -\int\limits_A \gamma\kappa v^i N_i \, dA - \int\limits_A \gamma_{,\alpha} t^\alpha_i \dot{t}^i \, dA + \oint\limits_{\partial A} \gamma \dot{t}^i n_i \, dL \,. \tag{2.48}$$

A similar functional, but with constant surface tension, has been considered by Skalak (1970). He proves that the stationary point of (2.48) with respect to a variation of $\mathbf{v}$ minimises $\dot{F}_{(\gamma)}$. Another variant of the functional (2.45) is defined if one substitutes $\dot{\mathbf{t}}$ by $\mathbf{v}$,

$$P_{(\gamma)}(\mathbf{v},\mathbf{t}) := \int\limits_A \gamma\, v^i_{,\alpha}\, t^\alpha_j \, dA \,. \tag{2.49}$$

This functional has been considered by Ho and Patera (1991), aiming at a “variational” formulation of the free-surface boundary conditions in the full time-dependent Navier–Stokes equations.[3] Compared to (2.45), in (2.49) not only the normal component of the parametrisation velocity $\dot{\mathbf{t}}$ is replaced by the velocity field $\mathbf{v}$, but also the tangential components. Hence, the two functionals $P_{(\gamma)}$ and $\dot{F}_{(\gamma)}$ do not represent the same physical quantity.

The three functionals in (2.45), (2.48), and (2.49) indeed provide some of the terms required in the weak stress-balance condition. The first variation of $\dot{F}_{(\gamma)}$ with respect to $\dot{\mathbf{t}}$

---

[3] According to the notion of *variational* used in this thesis they rather provide a *weak* formulation. Moreover, Finlayson (1972) shows that the stationary nonlinear Navier–Stokes equation cannot be obtained as the Euler–Lagrange equation of a functional, when varied with respect to the velocity field.

reads

$$\delta\dot{F}_{(\gamma)}[\delta\dot{\mathbf{t}}] = \int\limits_A \gamma\, t_i^\alpha \delta\dot{t}^i_{,\alpha}\, dA \tag{2.50}$$

$$= -\int\limits_A \delta\dot{t}^i(\gamma\kappa N_i + \gamma_{,\alpha} t_i^\alpha)\, dA + \oint\limits_{\partial A} \gamma n_i \delta\dot{t}^i\, dL\,. \tag{2.51}$$

The free-surface stress balance (2.44) can therefore be written as

$$\left.\frac{\delta P}{\delta \mathbf{v}}\right|_A + \left.\frac{\delta \dot{F}_{(\gamma)}}{\delta \dot{\mathbf{t}}}\right|_A = \mathbf{0}\,, \tag{2.52}$$

which again requires two different variations. The first variation of $\dot{F}_{(\gamma)}(\mathbf{v}, \dot{\mathbf{t}}, \mathbf{t})$ with respect to $\mathbf{v}$ reads

$$\delta\dot{F}_{(\gamma)}[\delta\mathbf{v}] = -\int\limits_A \gamma\kappa N_i \delta v^i\,. \tag{2.53}$$

It does not contain the surface gradient of the surface tension. Only the third functional, $P_{(\gamma)}$ provides exactly what is needed to write (2.44) in terms of the variation of a single functional with respect to a single variable, namely

$$\left.\frac{\delta(P + P_{(\gamma)})}{\delta \mathbf{v}}\right|_A = \mathbf{0}\,. \tag{2.54}$$

There is, however, a serious *caveat* against the calculation above. In order to explain our concerns, we return to the physical situation that is described by the functionals (2.45), (2.48), and (2.49). Since the velocity at the boundary is not restricted to be tangential, all three functionals describe a fully time-dependent free surface. However, a *moving* free surface with considerable surface tension typically leads to an unsteady flow. Stationary flows can easily be obtained with free surfaces without surface tension, such as material lines of the flow. Stationary flows can also be expected for time-independent free surfaces. For moving surfaces with tension, however, there are only very few special situations which result in a stationary flow, if there are any.

We arrive at the following dilemma: If one of the three functionals above is taken to describe a time-dependent free surface, then the resulting time-dependent flow in the volume is not described by P anymore. If, on the other hand, P is taken for granted, then we are missing a condition for the stationarity of the free surface – and thus for the flow. This condition, which must be obtained from the functionals above, reads

$$\dot{t}^i N_i = 0\,. \tag{2.55}$$

Up to now we have not made use of the argument $\mathbf{t}$ of the functionals. Let us see, whether the stationarity condition can be found as the first variation with respect to $\mathbf{t}$, reading for $\dot{F}_{(\gamma)}$,

$$\begin{aligned}\delta\dot{F}_{(\gamma)}[\delta\mathbf{t}] = &\int\limits_A \delta t^i N_i \Big\{2\gamma K \dot{t}^i N_i - \gamma(\dot{t}^i N_i)_{,\alpha\beta} a^{\alpha\beta} - \gamma_{,\alpha} a^{\alpha\beta}(\dot{t}^i N_i)_{,\alpha} \\ &\qquad - \gamma\kappa \dot{t}^\alpha_{,\alpha} - \gamma \dot{t}^\alpha \kappa_{,\alpha} + \gamma \dot{t}^\alpha_{,\beta} b^\beta_\alpha - \gamma_{,\alpha} b^\alpha \beta \dot{t}^\beta\Big\}\, dA \\ + &\int\limits_A \delta t^i t^\alpha_i \Big\{ - \gamma\kappa(\dot{t}^i N_i)_{,\alpha} + \gamma_{,\alpha}\kappa \dot{t}^i N_i - b^\beta_\alpha \gamma_{,\beta} \dot{t}^i N_i \\ &\qquad - \gamma\kappa b^\beta_\alpha \dot{t}_\beta - \gamma_{,\alpha} \dot{t}^\beta_{,\beta} + \gamma_{,\beta} \dot{t}^\beta_{,\alpha}\Big\}\, dA \\ + &\oint\limits_{\partial A} \delta t^i (\cdots)\, dL\,.\end{aligned} \tag{2.56}$$

K denotes the Gaussian curvature of the surface, being the determinant of the tensor $b_{\alpha\beta}$ of the second fundamental form. From (2.56) we obtain D further equations for the parametrisation velocity at the boundary, namely the curly braces in equation (2.56) set to zero. The first is due to the position variation in normal direction, the other in tangential directions, which are independent of each other. Note that the tangential components of the parametrisation velocity, given by the terms $\dot{t}^\alpha$, do not alter the position of the surface. The time-dependent parametrisation can always be chosen such that $\dot{t}^\alpha$ vanishes. We may therefore omit them in (2.56) without loss of generality and write the new boundary conditions as

$$0 = 2\gamma K \dot{t}^i N_i - \gamma(\dot{t}^i N_i)_{,\alpha\beta} a^{\alpha\beta} - \gamma_{,\alpha} a^{\alpha\beta}(\dot{t}^i N_i)_{,\alpha}\,, \tag{2.57 a}$$

$$0 = -\gamma\kappa(\dot{t}^i N_i)_{,\alpha} + \gamma_{,\alpha}\kappa \dot{t}^i N_i - b^\beta_\alpha \gamma_{,\beta} \dot{t}^i N_i\,. \tag{2.57 b}$$

When $\dot{t}^i N_i = 0$, these equations are fulfilled. The other way holds at least for constant γ: Since neither the curvature κ nor the Gaussian curvature K can be assumed to vanish, the second equation (2.57 b) renders $(\dot{t}^i N_i)$ constant. The first equation (2.57 a) then yields the stationarity condition (2.55). Hence, the D boundary conditions in (2.57) collapse into one single equation, namely the required stationarity condition (2.55).

The argumentation for $\dot{F}_{(\gamma)}$ fails for the functional $P_{(\gamma)}$. The variation of $P_{(\gamma)}$ has the same form (2.56), only the parametrisation velocity $\dot{t}^i$ is substituted by the flow velocity v^i. The resulting D boundary conditions therefore contain the tangential velocity v^α, which cannot be argued to vanish. Above, equation (2.54) made the functional $P_{(\gamma)}$ preferable to $\dot{F}_{(\gamma)}$ in both variants (2.45) and (2.48), because it yielded the stress balance at the free surface as a single variation. We now found that $P_{(\gamma)}$ is not able to yield the necessary stationarity condition (2.55).

The variation with respect to $\mathbf{t}$ is not yet complete. The change of the volume contribution P due to changes of the surface positions is still missing. It reads

$$\delta P[\delta\mathbf{t}] = \int\limits_A \delta t^k N_k \big[(p_0 g^{ij} - p g^{ij} + \eta e^{ij}) v_{i,j} - f^i v_i\big]\, dA\,. \tag{2.58}$$

The term in brackets is added to the right-hand side of equation (2.57 a) and destroys its interpretation as the desired stationarity condition. Note that the right-hand side of (2.58) contains a quadratic term in the derivatives of the velocity. This term can generally not be compensated by one of the definitions (2.46), (2.48) or (2.49), which are all linear in the velocity.

We have to conclude that a minimisation principle with neither of the functionals $(P + \dot{F}_{(\gamma)})$ and $(P + P_{(\gamma)})$ yields the stationary free-surface problem.[4] For the algorithmic formulation below, we thus revert to the variational description given in (2.44). This implies that we must use the same approximation order for the discretisation of the velocity and of the parametrisation of the surface.

2.2.5. Second variations

The search for the correct shape of the free surface requires the solution of equation (2.44) which is nonlinear in the parametrisation of the surface. One way to find the solution of a nonlinear equation is a Newton–Raphson iteration (Bronstein et al., 1995). We will utilise this method in our algorithm and therefore need a second variation of both the surface free energy F and the power P with respect to the parametrisation of the free surface. With the aid of the calculus of variations in Appendix B, the second variation of $F_{(\gamma)}$ is obtained as

$$\delta^2 F_{(\gamma)}[\delta\mathbf{t}, \delta\mathbf{t}] = \delta\bigg(\int\limits_A \gamma\, t_i^\alpha\, \delta t_\alpha^i\, dA\bigg)[\delta\mathbf{t}] \tag{2.59}$$

$$= \int\limits_A \gamma\, \delta t_\alpha^i \delta t_\beta^j \left(N_i N_j a^{\alpha\beta} + t_i^\alpha t_j^\beta - t_i^\beta t_j^\alpha\right) dA\,. \tag{2.60}$$

In contrast to the first variations, a transformation into the tensor form $\delta^2 F_{(\gamma)}/\delta\mathbf{t}\delta\mathbf{t}$ is not possible here. No integration by parts can remove the derivatives from both test functions

---

[4] The stress balance (2.44) as a variation of a single functional with respect to a single variable would have eased the consistent finite-element formulation of the free-surface stress balance and the development of a stable numerical algorithm. Below, in equation (2.63) we will require the mutual dependence of viscous stress and parametrisation when calculating second variations of the functionals. These mutual dependencies are not known without a combined functional. A single functional would also help to really understand the dissipative mechanisms in the stationary stress balance. It is astonishing that both the static free surface shape and the viscous flow can be obtained from individual minimisations, while both together cannot. Moreover, the description of the free surfaces given here might then be extended from pinned contact-lines to steadily moving ones, similar to the analysis by Hadjiconstantinou and Patera (2000).

δt^i and δt^j at the same time. The second variation of P is found to be

$$\delta^2 P[\delta\mathbf{v},\delta\mathbf{t}] = \delta\Big(\int_A \sigma_{ij} N^j \delta v^i \, dA\Big)[\delta\mathbf{t}] \tag{2.61}$$

$$= \int_A \delta v^i \sigma_i^j \delta t^k_\alpha (N_j t^\alpha_k - t^\alpha_j N_k)\, dA + \int_A \delta v^i N^j \, \delta\sigma_{ij}[\delta\mathbf{t}]\, dA \,. \tag{2.62}$$

The last integral contains the change of the fluidic stress at the boundary due to changes of its position, denoted by $\delta\sigma_{ij}[\delta\mathbf{t}]$. This term cannot be expressed in analytic form. The changes of the shape are communicated to the flow fields via the boundary conditions (1.9) and (1.11). At the same time, the flow fields satisfy the Stokes equations in the volume. This very indirect response of the stress tensor on the changes of shape cannot be expressed explicitly.

One might argue that the indirect response of the stress tensor on the changes of the boundary positions is a second-order response and should therefore be neglected. That this is not necessarily the case can be shown for the pressure part of the stress tensor: Above, we have used the pressure in both the dynamic and the static variation, which led to the equivalent variational formulations of the free-surface stress balance (2.38) and (2.44). The pressure contribution in the second variation (2.61) with respect to the mixed variables $[\delta\mathbf{v},\delta\mathbf{t}]$ can therefore be replaced by the second variation $\delta^2 F_{(\Phi)}[\delta\mathbf{t},\delta\mathbf{t}]$. This is of the same order as the terms $\delta^2 F_{(\gamma)}[\delta\mathbf{t},\delta\mathbf{t}]$ in (2.59). We therefore include the pressure term for the generally unknown change of the stress tension due to changes of the shape. Here, we take the pressure field, which is generated by the external body force and does not have to fulfil any boundary conditions, as quite independent of the precise shape of the surface. The change of the pressure is then well approximated by its gradient together with the change of the surface,

$$\delta\sigma_{ij} \approx -g_{ij}\, p_{,k}\, \delta t^k \,. \tag{2.63}$$

This approximation becomes exact in the static case without flow. The variation of the viscous contributions in (2.63) with respect to the parametrisation of the free surface is not known to us. It would follow from a formulation of the free-surface problem in terms of a single functional, which is not available.

2.3. Finite-element discretisation in two dimensions

Seeking for a numerical solution of the free-surface Stokes problem, we choose the weak formulation in terms of equations (2.41), (2.43), and (2.44). In the volume, the Stokes equations with external driving force read

$$0 = \frac{\delta P}{\delta p}\bigg|_V \quad \text{and} \quad \mathbf{0} = \frac{\delta P}{\delta \mathbf{v}}\bigg|_V \,. \tag{2.64 a,b}$$

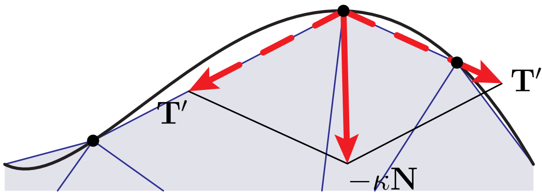

Figure 2.3. A visualisation of the tension forces $-\delta F_{(\gamma)}$ from (2.26) in the weak variational description of the free-surface stress condition. The smooth curve, which represents a one-dimensional free surface, is approximated by the sides of first-order finite elements. The elements provide the mesh for solving the flow equations. At the boundary nodes, the tangential vectors are not continuous. Thus, neither a normal vector nor a curvature can be calculated. The situation can be improved only gradually but not generally by employing second-order finite elements. For the weak formulation (2.26) of the tension forces, a smooth representation of the surface is not needed anymore. The formulation is such that for a node the contributions of the adjacent finite-element sides are given by their respective tangential vectors, scaled by the surface tension. The directions of the pulling forces, indicated by dashed arrows, are the normalised tangent vectors. The solid arrow indicates the direction and the magnitude of the resulting force, which is an approximation of the normal vector, scaled by the curvature κ of the surface. From the continuous equations (2.26) and (2.30) it can be seen that this approximation becomes exact in the limit of short element sides.

At the boundary, the surface-stress boundary condition (1.11) is given in variational form by equation (2.44),

$$\left.\frac{\delta P}{\delta \mathbf{v}}\right|_A = -\left.\frac{\delta F_{(\gamma)}}{\delta \mathbf{t}}\right|_A .$$

Additionally, the kinematic boundary condition (1.9) must be satisfied, which cannot be derived from variational principles in the present framework. We will therefore impose it in its strong form (1.9).

A discretisation by finite elements requires a computational mesh together with piecewise smooth ansatz functions. We choose the ansatz functions to be node-based functions yielding unity at exactly one node of the computational mesh, and zero at all others. The functions that can be approximated in this way are continuous, but not everywheredifferentiable. We use first-order ansatz functions $\psi_d(\mathbf{x})$ for the pressure and second-order ansatz functions $\phi_d(\mathbf{x})$ for the Cartesian velocity components,

$$u(\mathbf{x}) = \sum_d u_d\,\phi_d(\mathbf{x})\,, \qquad v(\mathbf{x}) = \sum_d v_d\,\phi_d(\mathbf{x})\,, \tag{2.65 a}$$

$$p(\mathbf{x}) = \sum_d p_d\,\psi_d(\mathbf{x})\,. \tag{2.65 b}$$

We recall that also the geometry of the free surface, bounding the fluid, is part of the problem. Thus, the positions of the mesh nodes themselves are to be calculated. For the Cartesian components of points inside the finite elements and on their boundaries, we introduce the variables r and s, approximated with ansatz functions χ_d,

$$r(\mathbf{x}) = \sum_d r_d\,\chi_d(\mathbf{x})\,, \qquad s(\mathbf{x}) = \sum_d s_d\,\chi_d(\mathbf{x})\,. \tag{2.66}$$

These two functions, although they appear to be quite redundant when read as $r(x,y)=x$ and $s(x,y)=y$, are nevertheless needed to obtain the Cartesian components of the mesh nodes. Since our ansatz functions are node-based, the coordinates (x_d, y_d) of the dth node coincide with the values (r_d, s_d) that can be calculated with. Equation (2.66) thus provides the geometry of the finite elements, which consist of a set of nodes together with a set of ansatz functions. They parameterise the boundaries and the volume between the nodes. Unless stated otherwise, we will use second-order ansatz functions χ_d for the approximation of the geometry of finite elements, yielding second-order finite elements. An important consequence of using ansatz functions for the geometry of the finite elements is that the parametrisation of the mesh is only piecewise smooth, when understood as the mapping from reference coordinates onto Cartesian coordinates. The reference coordinates are defined independently for each finite element. As a consequence, the boundaries of the mesh are not smooth at the nodes. This fact has severe implications for the discrete representation of a free surface, as is illustrated in Figure 2.3. The sides of the elements are parameterised by first-order, i. e. linear ansatz functions. The tangential vector is discontinuous at the boundary nodes, therefore neither normal vectors nor the curvature can be calculated. The curvature of the original smooth curve rather collapses into the corners at the boundary nodes. The linear approximation in Figure 2.3 has been chosen to demonstrate this in a distinct way. A second-order approximation improves the approximation significantly, but cannot relieve the problem with the corners. Still, the curvature of a second-order element side provides only a poor approximation of the "true" curvature of the original curve.

The dependence of the curvature on the second surface-derivatives of the parametrisation t^i can be replaced by a product of two first derivatives, one of them being a tangential vector, see equation (2.26). By using this trick, we avoid the explicit use of the curvature κ in the free-surface stress balance, which stems from (2.30). Then, a piecewise smooth approximation of the surface suffices, such as the one in Figure 2.3. In contrast to the curvature, the tangential vectors in (2.26) can easily be calculated using finite elements. The integration by parts of the curvature term has been used in different contexts in the literature (Brakke, 1992; Dziuk, 1991; Zinchenko et al., 1997; Bänsch, 1998).

From a physics perspective, the formulation (2.26) of the tension terms is the more natural one, compared to (2.30). From (2.26), one directly deduces that forces pulling along the tangential direction attempt to minimise the facet area of an element. The pulling forces of adjacent elements add up to the tension force which is proportional to the curvature. Figure 2.3 depicts this for first-order elements.

2.3.1. Separating the algorithm into two steps

As pointed out in the introduction, for free boundaries a twofold problem must be solved: (i) The unknown fluid domain V is to be determined and (ii) the Stokes equations (1.4) and (1.6) are to be solved within V, using the boundary conditions (1.9) and (1.11).

The latter both depend on the shape of V via the normal vector and the curvature at the boundary. Both parts cannot be processed independently. In principle, there exist two options to deal with this combined problem. The first is to implement a single numerical system of coupled algebraic equations for both, the flow variables p and v^i, together with the geometry variables t^i. We will not follow this direction but rather solve two smaller systems of equations consecutively, one for the flow variables, depending on the current domain V, and a second one for the parametrisation of the boundary. We have chosen this approach because the problem is linear in the flow variables and highly nonlinear in the geometry variables t^i. Nonlinearities are unavoidable in the geometric description of the free surface. In our approach, the nonlinearities are confined to one relatively small subsystem.

The nonlinearity of the boundary condition can explicitly be seen in the definition of the surface metric (2.15). The Jacobi determinant $\sqrt{a}$ and the inverse metric $a^{\alpha\beta}$ are nonlinear functions of the parametrisation as well. They occur in the strong formulation (1.11) as well as in the variational formulation (2.44), and also in the different terms of the weak variational formulation in equations (2.26)–(2.28) and (2.37). The nonlinearity is not a consequence of an unnecessarily complicated parametrisation, but of the intrinsic property of the free surface being curved. A linear parametrisation describes flat surfaces only. Numerical algorithms for solving nonlinear equations are subject to various problems. First, the uniqueness of a solution is not granted in nonlinear systems. Instead, the particular solution found by an algorithm may depend on the initial state. Another problem concerns stability. A solution can only be approached step-wise, and there is no guarantee that the system finds its way from the initial state to a solution.

Our approach, namely to confine the nonlinearities into one of the sub-problems, makes it necessary to process the whole algorithm as a succession of two steps. In one step, the velocity and the pressure fields are determined. This step requires the solution of the Stokes equations, which are *linear* in the velocity and pressure variables. The other step performs the *nonlinear* search for a better boundary shape. In the following, the two numerical systems which perform the two steps will be called *fluidic system* and *geometric system*, respectively.

For the linear fluidic system, D boundary conditions uniquely determine the solution. In D-dimensional space, the equations (1.9)–(1.11) pose $D+1$ boundary conditions, which is one too many for the linear fluidic system to be fully determined. The remaining boundary condition is therefore used for updating the parametrisation of the free surface (Cuvelier and Schulkes, 1990). There has been a controversy which boundary condition should be used for updating the surface. One possible candidate is the kinematic boundary condition (1.9). The general procedure in this case is that the stress balance condition (1.11) determines the flow field, while the resulting velocity v^i at the boundary is employed to move the surface. A different possibility utilises the stress balance condition for the flow field and moves the free surface according to the resulting normal stress. Saito and Scriven (1981) claim that when the capillary number falls below unity, an iteration by the normal stress converges well and a kinematic iteration eventually fails. As the capillary number rises beyond unity, the performances of the two iteration schemes are reversed. The main challenge for a numerical algorithm is therefore the proper assignment of specific boundary conditions to the two sub-systems in order to make them solvable, uniquely determined, and robust. It is clear that the no-slip boundary condition (1.10) at sticky walls applies only to the fluidic system. The free-surface boundary condition still needs further consideration.

In Section 1.1.4, the assignment of boundary conditions to the fluidic and the geometric problem has been addressed in the limit of infinite surface tension. In this limit, the mutual dependence of the two problems is removed completely. The assignment of boundary conditions must then be chosen such that the flow obeys a perfect-slip condition, while the normal projection of the stress-balance yields the Laplace–Young equation, which determines the shape of the free surface. In the microfluidic parameter regime, the surface tension is not infinite but large, leading to capillary and Bond numbers up to the order of unity, see Section 1.1.3. We therefore expect the two sub-problems to be decoupled sufficiently if the assignment of the system is the same as in the limit of infinite surface tension. This is the central assumption, on which the presented algorithm rests. The normal component of the stress balance is thus assigned to the geometric system, while the perfect-slip condition (1.16) is imposed on the flow.

The fluidic system

The fluidic system is implemented according to the variational formulation of the Stokes equations (2.64) in the volume. The weak variational formulation can be obtained from the volume integrals in equations (2.41) and (2.43),

$$0 = -\int\limits_V v^i_{,i}\, \delta p \, dV \,, \tag{2.67}$$

$$\begin{aligned} 0 &= -\int\limits_V (\sigma^{ij}_{,j} + f^i)\, \delta v_i \, dV \\ &= -\int\limits_V f^i \delta v_i \, dV + \int\limits_V \sigma^{ij} \delta v_{i,j} \, dV - \oint\limits_{\partial V} \sigma^{ij} N_j \, \delta v_i \, dA \,. \end{aligned} \tag{2.68}$$

These equations are subject to the slip boundary conditions, which consist of the kinematic boundary condition (1.9) and the tangential projections of the stress balance (1.11). According to the variational formulation (2.44), the latter can be written as

$$\mathbf{T} \cdot \left. \frac{\delta P}{\delta \mathbf{v}} \right|_A = 0 \,, \tag{2.69}$$

because for constant surface tension the variation of $F_{(\gamma)}$ is always orthogonal to the surface. Equation (2.69) allows us to write this part of the slip boundary condition in a weak variational form

$$\int\limits_A \sigma_{ij}\, N^j\, \delta v^i\, dA = 0\,. \tag{2.70}$$

According to the LBB requirement, we approximate the pressure variable with the first-order ansatz functions ψ_d and the Cartesian components of the velocity field independently with the second-order ansatz functions ϕ_d. Together with the approximation (2.65) of the solution functions and with the discretisation rule (2.6), which here becomes

$$\delta p \mapsto \psi_d\,, \tag{2.71}$$

$$\mathbf{e}_x \cdot \delta\mathbf{v} \mapsto \phi_d\,, \qquad e_x^i \delta v_{i,j} \mapsto (\phi_d)_{,j}\,, \tag{2.72 a,b}$$

$$\mathbf{e}_y \cdot \delta\mathbf{v} \mapsto \phi_d\,, \qquad e_y^i \delta v_{i,j} \mapsto (\phi_d)_{,j}\,, \tag{2.72 c,d}$$

the Stokes equations in the volume are cast into the linear system of equations for the DOFs, which are grouped into the vectors $\vec{u}$, $\vec{v}$, and $\vec{p}$,

$$\begin{pmatrix} K_{uu} & 0 & K_{up} \\ 0 & K_{vv} & K_{vp} \\ K_{pu} & K_{pv} & 0 \end{pmatrix} \begin{pmatrix} \vec{u} \\ \vec{v} \\ \vec{p} \end{pmatrix} = \begin{pmatrix} L_u \\ L_v \\ 0 \end{pmatrix}\,. \tag{2.73}$$

The first two rows correspond to the Stokes equation, while the last row is the discretisation of the incompressibility condition. The block matrices K and vectors L are given by

$$[K_{uu}]_{de} = [K_{vv}]_{de} = \eta \int\limits_V \nabla\phi_d \cdot \nabla\phi_e\, dV - \eta \oint\limits_{\partial V} \phi_d \mathbf{N} \cdot \nabla\phi_e\, dA\,, \tag{2.74 a}$$

$$[K_{up}]_{de} = -\int\limits_V (\partial_x\phi_d)\psi_e\, dV + \oint\limits_{\partial V} \phi_d\psi_e N_x\, dA\,, \tag{2.74 b}$$

$$[K_{vp}]_{de} = -\int\limits_V (\partial_y\phi_d)\psi_e\, dV + \oint\limits_{\partial V} \phi_d\psi_e N_y\, dA\,, \tag{2.74 c}$$

$$[K_{pu}]_{de} = -\int\limits_V \psi_d \partial_x \phi_e\, dV\,, \tag{2.74 d}$$

$$[K_{pv}]_{de} = -\int\limits_V \psi_d \partial_y \phi_e\, dV\,, \tag{2.74 e}$$

$$[L_u]_d = \int\limits_V \phi_d f_x\, dV\,, \tag{2.74 f}$$

$$[L_v]_d = \int\limits_V \phi_d f_y\, dV\,. \tag{2.74 g}$$

All integrals are assembled in a loop over the elements and the sides of the mesh, using a fifth-order Gaussian quadrature rule. The fluidic system could likewise implement the stationary Navier–Stokes equations with a small Reynolds number. Here, we have chosen the Stokes equation for simplicity and for consistency with the variational derivation of Section 2.2.

In Section 2.1, it has already been announced that the perfect-slip boundary condition of equation (1.16) is not a "natural" boundary condition for the stationary Stokes equation. The slip boundary condition specifies the tangential component of the normal stress together with the kinematic condition. The naturally occurring boundary term (2.70), see also equation (2.43), however consists of the whole normal stress, containing tangential and normal components. The kinematic boundary condition is not included in the variational principles at all. Therefore, the slip boundary condition is not a natural boundary condition and has not been embedded into the linear system (2.73). Instead, we have to find a different method to enforce the slip boundary condition. One possibility is to employ a constraint technique: A DOF u_d, which resides on a boundary node and thus carries a boundary condition, is expressed by an inhomogeneity plus a weighted sum of other DOFs,

$$u_d = w_d + \sum_{e \neq d} w_{de}\, u_e \,. \tag{2.75}$$

The DOF u_d is then completely eliminated from the linear system (2.73). In this way, we implement the kinematic boundary condition (1.9) as

$$0 = \sum_d (u_d N_x + v_d N_y)\, \phi_d \,. \tag{2.76}$$

In the same manner, the tangential projection of the weak free-surface boundary condition (2.70) is written as

$$0 = \sum_e \begin{pmatrix} u_e \\ v_e \end{pmatrix} \cdot \begin{pmatrix} 2T_xN_x & T_xN_y + T_yN_x \\ T_xN_y + T_yN_x & 2T_yN_y \end{pmatrix} \int_A \phi_d \begin{pmatrix} \partial_x \phi_e \\ \partial_y \phi_e \end{pmatrix} dA \,. \tag{2.77}$$

The constraint equations (2.76) and (2.77) differ only with respect to the weights w_{de}. The inhomogeneity w_d is zero in all three equations. Non-zero inhomogeneities would result if also a surface-gradient term of the tension were taken into account in equation (2.77), or if the rigid walls performed a tangential movement.

In both constraint equations (2.76) and (2.77), a consistent definition of normal and tangential vectors is crucial. In Section 2.2, we found that for the tension-related aspect of the free-surface the definition of a normal vector at the nodes can be avoided. Here, we do not have a proper weak formulation which would allow to integrate by parts. As a starting point, we define the normal vector at a node as the arithmetic average of the normal vectors of the adjoining finite-element sides. Behr (2004) observed that an improper choice of the normal direction can cause spurious contributions in the velocity field, even if only conservative forces are applied. He recommends the use of a normal vector which is averaged with the stress on each adjoining side. Walkley et al. (2004) use arithmetic averages in three-dimensional calculations. In the presence of only conservative forces, we did not find spurious flows in our results.

The constraint equation (2.77) has the unwanted side-effect that each of the DOFs residing on a boundary node is defined in terms of all its neighbours on the boundary. Thus, all boundary DOFs are cross-linked. This leads to a nearly fully filled system-matrix which is prohibitory regarding memory capacity and computing time. We found that an iterative method can overcome this problem. Instead of defining a boundary DOF in terms of all its neighbours, we take previous values or extrapolated values for some of the neighbouring DOFs in the constraint equation (2.77). After some iterations, the full boundary condition (2.77) is established. This procedure makes it possible to enforce the perfect-slip boundary condition explicitly. A minor drawback of this scheme is that the constraint equations have to be reassembled after each solution step of the fluidic system. Since the assembly of the system does not take very long, compared to solving it, this does not matter very much. The details of the procedure, which DOFs are taken to constrain which of their neighbours, are provided in Appendix C.

The geometric system

The tangential components of the free-surface stress balance condition have already been used in the slip boundary condition (2.69) for the fluidic system. The remaining normal component, reading

$$\mathbf{N}\cdot\left.\frac{\delta P}{\delta\mathbf{v}}\right|_A = -\mathbf{N}\cdot\left.\frac{\delta F_{(\gamma)}}{\delta\mathbf{t}}\right|_A , \tag{2.78}$$

will be used as the update equation for the parametrisation variables r and s of the free surface. To reformulate (2.78) as an update equation, we introduce the residual vector of the variational formulation of the stress balance (2.44),

$$\mathbf{L} = \left.\frac{\delta F_{(\gamma)}}{\delta\mathbf{t}}\right|_A + \left.\frac{\delta P}{\delta\mathbf{v}}\right|_A , \tag{2.79}$$

which shifts the positions of the free surface. In a static system without flow, an update using the vector $-\mathbf{L}$ reduces to a steepest gradient descent on the functional $F_{(\gamma)}$. In a driven system, it takes the additional fluidic stress into account.

This is the very point in the algorithm where the reasoning of Section 2.2 about the different physical meanings of the forces in the free-surface boundary condition becomes relevant. If the calculation in Section 2.2.4 had provided a combined functional G, then we could have written $\mathbf{L}$ as $\delta G/\delta\mathbf{v}$. Since this is not the case, the normal component of the boundary condition (2.44) must be tested either with $\delta\mathbf{t}$ or with $\delta\mathbf{v}$. We will use $\delta\mathbf{t}$ because the most troublesome term in this calculation is the curvature κ, containing second derivatives. According to equations (2.30) and (2.26), the curvature can then be dissolved into two terms, each containing only a first derivative. The weak formulation of the force vector $\mathbf{L}$ in normal direction then reads

$$\begin{aligned}\int\limits_A L_i \delta t^i \, dA &= \int\limits_A \gamma \, t_i^\alpha \, \delta t^i_\alpha \, dA + \int\limits_A \sigma_{ij} \, N^j \delta t^i \, dA \\ &= -\delta F_{(\gamma)}[\delta \mathbf{t}] + \int\limits_A \sigma_{ij} \, N^j \delta t^i \, dA \, . \end{aligned} \tag{2.80}$$

Again, the replacement rule (2.6) can be applied to obtain the discretised version of the Cartesian components of the integral on the left-hand side,

$$[L_r]_d = \int\limits_A \gamma \, (\mathbf{e}_x \cdot \mathbf{T}) \, (\mathbf{T} \cdot \boldsymbol{\nabla} \chi_d) \, dA + \int\limits_A (\mathbf{e}_x \cdot \sigma \mathbf{N}) \, \chi_d \, dA \, , \tag{2.81 a}$$

$$[L_s]_d = \int\limits_A \gamma \, (\mathbf{e}_y \cdot \mathbf{T}) \, (\mathbf{T} \cdot \boldsymbol{\nabla} \chi_d) \, dA + \int\limits_A (\mathbf{e}_y \cdot \sigma \mathbf{N}) \, \chi_d \, dA \, . \tag{2.81 b}$$

If the ansatz functions ϕ_d and χ_d are chosen to be equal, then these equations become fully consistent with (2.79). The replacement rule here approximates each Cartesian component of the surface parametrisation with an ansatz function χ_d,

$$\mathbf{e}_x \cdot \delta \mathbf{t} \mapsto \chi_d \, , \qquad e_{(x)i} \, \delta t^i_{,\alpha} \mapsto (\chi_d)_{,\alpha} = t^i_\alpha \, (\chi_d)_{,i} \, , \tag{2.82 a,b}$$

$$\mathbf{e}_y \cdot \delta \mathbf{t} \mapsto \chi_d \, , \qquad e_{(y)i} \, \delta t^i_{,\alpha} \mapsto (\chi_d)_{,\alpha} = t^i_\alpha \, (\chi_d)_{,i} \, . \tag{2.82 c,d}$$

As the parametrisation variations δt^i are scalars with respect to the surface coordinates, their derivatives $\delta t^i_{,\alpha}$ have been be expressed by the tangential projection of the spatial gradient of χ_d in equations (2.82 b,d).

The residual vector $\mathbf{L}$ has the dimension of a force. In order to determine the displacement of the node positions caused by this force, we employ a Newton–Raphson method (Bronstein et al., 1995). The local displacement of the free surface is then determined from the force components $([L_r]_d, [L_s]_d)$ and their derivatives with respect to the parametrisation. Thus, in the geometric part of the algorithm we repeatedly solve the following linear system of equations,

$$\begin{pmatrix} \dfrac{\partial [L_r]_d}{\partial r_e} & \dfrac{\partial [L_r]_d}{\partial s_e} \\[2ex] \dfrac{\partial [L_s]_d}{\partial r_e} & \dfrac{\partial [L_s]_d}{\partial s_e} \end{pmatrix}^{\text{(old)}} \begin{pmatrix} \vec{r}_e^{\,\text{(new)}} - \vec{r}_e^{\,\text{(old)}} \\[2ex] \vec{s}_e^{\,\text{(new)}} - \vec{s}_e^{\,\text{(old)}} \end{pmatrix} = -\tau \begin{pmatrix} [L_r]_d \\[2ex] [L_s]_d \end{pmatrix}^{\text{(old)}} \, , \tag{2.83}$$

where $\tau \in [0, 1]$ denotes a step-size parameter. In all applications below, we use values of τ between 0.1 and 1.0. The entries of the matrix can either be calculated as the partial derivatives of the discretised vector $\mathbf{L}$ in (2.81), or equivalently as the discretised version of the continuous second variations of the surface free energy $F_{(\gamma)}$ and the power P, see equations (2.59) and (2.61). In the continuous formulation we have seen in equation (2.63) that the change of the pressure due to changes of the free surface must be taken into account. This term is necessary to yield a stable numerical algorithm and must likewise occur in the discrete formulation.

2.3.2. Similarity of free surfaces and rubber bands

The regularity of the computational mesh is an indispensable requirement for a stable numerical calculation. Very slim elements or drastic changes in the local density of elements can affect the properties of the linear systems of equations that are solved by the computer. In many cases, this results in errors that are amplified from iteration step to iteration step. In the case of minimising the free surface, the instability becomes manifest in the shrinking and growing of finite elements. This effect can be observed in the program *surface evolver*. The documentation (Brakke, 1992) therefore recommends to monitor the mesh quality and to re-mesh the surface whenever necessary. Similar effects were reported by Brinkmann (2005).

A look on equations (2.81) helps to explain the problems. In the numerical implementation, the integrals over the free surface in equation (2.81) are evaluated as separate integrals over the facets. At a node d, the resulting force $([L_r]_d, [L_s]_d)$ is the sum of the respective contributions from the adjacent sides m,

$$\left[L_r^{(m)}\right]_d = \int\limits_{A_{(m)}} \gamma\,(\mathbf{e}_x \cdot \mathbf{T}_{(m)})\,(\mathbf{T}_{(m)} \cdot \boldsymbol{\nabla}\chi_d)\,dA + \int\limits_{A_{(m)}} (\mathbf{e}_x \cdot \sigma\mathbf{N}_{(m)})\,\chi_d\,dA\,, \qquad (2.84\,\mathrm{a})$$

$$\left[L_s^{(m)}\right]_d = \int\limits_{A_{(m)}} \gamma\,(\mathbf{e}_y \cdot \mathbf{T}_{(m)})\,(\mathbf{T}_{(m)} \cdot \boldsymbol{\nabla}\chi_d)\,dA + \int\limits_{A_{(m)}} (\mathbf{e}_y \cdot \sigma\mathbf{N}_{(m)})\,\chi_d\,dA\,. \qquad (2.84\,\mathrm{b})$$

The gradient $\boldsymbol{\nabla}\chi_d$ in the first integrals of equations (2.84) is proportional to the inverse length of the one-dimensional surface facet m, because the ansatz function χ_d assumes values between zero and unity. Consequently, the forces caused by the surface tension do not scale with the facet size $A_{(m)}$, as is depicted in Figure 2.3. Neither do the changes of the nodal positions adapt themselves to the size of the participating facet. As long as the shifts occur only in normal direction, this does not matter. Tangential shifts, however, soon lead to shrinking and growing surface facets, resulting in an irregular boundary mesh and an unstable algorithm. The situation is slightly better for two-dimensional surfaces in three-dimensional space. The forces are then proportional to an effective diameter of a facet.

Our resolution of the problem is the following. We propose to scale the contributions from each free-surface facet with the length $A_{(m)}$ of the corresponding facet, divided by the average length $\langle A_{(m)} \rangle$ of all free-surface facets. The force then comprises not only a normal component, but also a tangential component, as can be seen from Figure 2.4 in comparison with Figure 2.3. In Section 2.3.1, we have assigned the boundary conditions to the two sub-problems in such a way that only the normal component of the stress balance becomes relevant for the movement of the free surface. We are therefore free to employ the occurring additional tangential forces for keeping the boundary mesh regular, as long as we do not modify the forces in normal direction.

For a constant surface tension, the change of the free energy of a single surface facet m reads $\delta F_{(m)} = \gamma \delta A_{(m)}$. Scaling the force on the facet with the proposed factors yields

$$\gamma \frac{A_{(m)}}{\langle A_{(m)} \rangle} \, \delta A_{(m)}[\delta \mathbf{t}] = \frac{\gamma}{2\langle A_{(m)} \rangle} \, \delta\big(A_{(m)}^2\big)[\delta \mathbf{t}] \, . \tag{2.85}$$

Here we find that the proposed scaling factors $A_{(m)}/\langle A_{(m)} \rangle$ modify the variational description such that a functional consisting of the *squares of the facet lengths* is minimised. This functional has some similarity with (and subtle differences from) the functional for a rubber band, as will be discussed now. A straight piece of rubber with spring constant $\gamma/\langle A_{(m)} \rangle$ exerts the force (2.85), when stretched by the length $A_{(m)}$. A rubber band has the decisive advantage, compared to a free surface, that it is able to compensate forces in arbitrary directions, not only in normal direction. The stabilised description (2.85) of the force of a free surface is therefore able to compensate small tangential components of the applied fluidic stress, which are due to numerical rounding errors. Additionally, the tangential components which occur in (2.85) tend to equalise the lengths of adjacent surface facets. Note, however, that a subtle distinction has to be made between a discretised rubber band and our stabilised free surface. In continuous notation, the energy functional of the rubber band is the integral over the square of the Jacobi determinant, which generally does not equal the square of the length,

$$\int_E a \, d\nu \neq \Big(\int_E \sqrt{a} \, d\nu \Big)^2 \, . \tag{2.86}$$

In case of a piecewise straight representation of the surface, both are equal. For a discretisation with curved element sides they are not. However, as long as we aim at a stable algorithm for the free surface and not for the rubber band, the precise interpretation of the tangential components of (2.85) is not important.

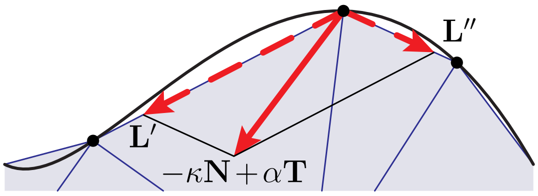

Figure 2.4. The same discrete approximation for a smooth curve as in Figure 2.3. Here, the pulling forces $\mathbf{L}'$ and $\mathbf{L}''$ are scaled to be proportional to the corresponding side length, according to the rubber-band formulation in equation (2.85). The resulting force contains a tangential component $\alpha\mathbf{T}$ which depends on the length difference of the participating element sides. Its precise magnitude is unspecified.

If all free-surface facets have equal lengths $A_{(m)} = \langle A_{(m)} \rangle$, then the scaling factors $A_{(m)} / \langle A_{(m)} \rangle$ in equation (2.85) have no effect and the behaviour of the free surface is re-established. This situation corresponds to a converged final state of the algorithm. This fact is due to the construction of the algorithm in Section 2.3.1, where the flow always has to satisfy the perfect-slip boundary condition (1.16 b), such that no tangential force components are applied by the flow. During the run of the algorithm, the deviations of the facet lengths from their average value provide a good measure for convergence: As long as the surface is not yet in its solution position, the normal components of the shifts dominate over the tangential components. When the surface is about to reach its final position, then the normal components decrease and give way to the tangential components to equilibrate the facet lengths. In the numerical examples below, it proved useful to monitor the statistical spread of the facet lengths as a measure of convergence.

For the Newton iteration we require the second variations of the surface free energy. We scale them with the same factors as the first variations in equation (2.85),

$$\gamma \frac{A_{(m)}}{\langle A_{(m)} \rangle} \delta^2 A_{(m)}[\delta \mathbf{t}, \delta \mathbf{t}] = \frac{\gamma}{2\langle A_{(m)} \rangle} \delta^2 \big(A_{(m)}^2\big)[\delta \mathbf{t}, \delta \mathbf{t}] - \gamma \frac{\big(\delta A_{(m)}[\delta \mathbf{t}]\big)^2}{\langle A_{(m)} \rangle} , \qquad (2.87)$$

finding that the second variations of the stabilised free surface and of the rubber-band analogue are not equal. This does not matter, as we are interested only in the description of a free surface.

We conclude that by scaling the force contributions of the individual facets with their corresponding lengths, we have arrived at a stabilised algorithm for the free surface. All facet lengths tend to the same average value, providing a perfectly regular boundary mesh. As soon as all facets arrive at the same length, the behaviour of the free surface is re-established. The discretised free surface thus adopts the advantageous property of a rubber band, that it can compensate forces also in tangential direction.

2.3.3. Summary of the algorithm

Here, we provide a short overview of the complete algorithm. The required steps are as follows:

1. Choose an initial mesh and initial ambient pressure p_0.
2. Until convergence repeat the following steps:
    - *a*) Smooth the inner mesh if it is too distorted.
    - *b*) Repeatedly solve the fluidic system for the pressure p and the velocity components u and v, until the slip boundary condition is established.
    - *c*) Subtract the average from p, thus yielding $\int_V p\, dV = 0$.

d) Solve the geometric system for the new boundary. At the same time, search for the value of p_0 that keeps the volume unchanged.

e) Set the mesh boundary nodes to the parametrisation values of the geometric system.

The fluidic system is assembled according to equations (2.73) and (2.74) with constraint equations (2.76) and (2.77) that incorporate the proper boundary conditions. Here, we summarise the terms of the geometric system. Its update equation (2.83) is written as

$$\begin{pmatrix} K_{rr} \, K_{rs} \\ K_{sr} \, K_{ss} \end{pmatrix}^{\text{(old)}} \begin{pmatrix} \vec{r} \\ \vec{s} \end{pmatrix}^{\text{(new)}} = -\tau \begin{pmatrix} L_r \\ L_s \end{pmatrix}^{\text{(old)}} + \begin{pmatrix} K_{rr} \, K_{rs} \\ K_{sr} \, K_{ss} \end{pmatrix}^{\text{(old)}} \begin{pmatrix} \vec{r} \\ \vec{s} \end{pmatrix}^{\text{(old)}} \tag{2.88}$$

with entries that are assembled per element m,

$$\begin{aligned} \left[K_{rr}^{(m)}\right]_{de} = &- \int\limits_{A_{(m)}} \chi_d \chi_e (\mathbf{e}_x \cdot \boldsymbol{\nabla} p)(\mathbf{e}_x \cdot \mathbf{N}) \, dA \\ &+ \int\limits_{A_{(m)}} \chi_d \, (\boldsymbol{\nabla} \chi_e \cdot \mathbf{T}) \Big\{ (\mathbf{e}_x \cdot \sigma \mathbf{N})(\mathbf{e}_x \cdot \mathbf{T}) - (\mathbf{e}_x \cdot \sigma \mathbf{T})(\mathbf{e}_x \cdot \mathbf{N}) \Big\} \, dA \\ &+ \frac{\gamma A_{(m)}}{\langle A_{(m)} \rangle} \int\limits_{A_{(m)}} (\boldsymbol{\nabla} \chi_d \cdot \mathbf{T})(\boldsymbol{\nabla} \chi_e \cdot \mathbf{T}) \, dA \, , \end{aligned} \tag{2.89}$$

$$\begin{aligned} \left[K_{rs}^{(m)}\right]_{de} = &- \int\limits_{A_{(m)}} \chi_d \chi_e (\mathbf{e}_x \cdot \boldsymbol{\nabla} p)(\mathbf{e}_y \cdot \mathbf{N}) \, dA \\ &+ \int\limits_{A_{(m)}} \chi_d \, (\boldsymbol{\nabla} \chi_e \cdot \mathbf{T}) \Big\{ (\mathbf{e}_x \cdot \sigma \mathbf{N})(\mathbf{e}_y \cdot \mathbf{T}) - (\mathbf{e}_x \cdot \sigma \mathbf{T})(\mathbf{e}_y \cdot \mathbf{N}) \Big\} \, dA \, , \end{aligned} \tag{2.90}$$

$$\left[L_r^{(m)}\right]_d = \int\limits_{A_{(m)}} \chi_d \, (\mathbf{e}_x \cdot \sigma \mathbf{N}) \, dA + \frac{\gamma A_{(m)}}{\langle A_{(m)} \rangle} \int\limits_{A_{(m)}} (\boldsymbol{\nabla} \chi_d \cdot \mathbf{T})(\mathbf{e}_x \cdot \mathbf{T}) \, dA \, . \tag{2.91}$$

The remaining entries can be obtained by permutations of x and y together with r and s. Again, constraints have been used to keep the contact lines pinned, using constraint equations for a Dirichlet-type boundary condition, comprising only a single DOF with an inhomogeneity. The first terms in (2.89) and (2.90) stem from the approximation (2.63), where the gradient of the pressure is taken into account. The next integrals in both equations stem from the second variation of the power P in (2.61). The last term in equation (2.89) is the stabilised term standing for the surface tension and the curvature. It originates from the second variation of the surface free energy $F_{(\gamma)}$ in (2.59), where we found it necessary to modify this term in the implementation. The second variation comprises a term $(N_i N_j a^{\alpha\beta} + t_i^\alpha t_j^\beta - t_i^\beta t_j^\alpha)$ that causes severe instabilities in the algorithm if implemented like this. Instead, we found $(g_{ij} a^{\alpha\beta})$ to serve well. This modification apparently has no influence on the accuracy of the free-surface algorithm, as will be shown in the next section. The terms in (2.91) have been implemented along the description of the previous sections, including the stabilisation technique.

For implementing these equations, we have used the open-source finite-element library *libmesh*[5] which allows to change the geometry of finite elements in a user's routine and provides a powerful constraint method.

2.3.4. Accuracy tests

The best way to prove the accuracy of a numerical algorithm is to compare the result with an analytical solution. Unfortunately, there are no known analytical solutions of the full nonlinear free-surface flow problem in a prescribed non-trivial domain. Already the linear Stokes equations are difficult to solve analytically, see Appendix A for an example. We thus have to test the parts of the algorithm individually. In the current section, the geometric sub-problem is tested. The surface shape in a static setting is calculated in two analytically solvable cases. The comparison confirms the accuracy of the geometric part of the problem, namely the curvature approximation. The setup is the following: A prescribed pressure field determines the free-surface shape. Under this assumption, the approximation in equation (2.63) becomes exact, so that all possible approximation errors must be due to the discretisation of the curvature.

Figure 2.5 depicts the simple situation with a homogeneous pressure field which deforms the boundary into a circular arc with radius $R = -1/\kappa = p_0/\gamma$. In dimensionless units, the surface tension is $\gamma = 1$, and the prescribed pressure $p_0 = 2$ produces a circle with radius $R = 1/2$ as the exact solution. In Figure 2.5, two different approximations are presented. The first contains only five second-order finite elements and yields a very accurate representation of the exact solution. Its relative error can be estimated from the topmost node which misses its target position by less than 0.4%. The relative error of the curvature is even smaller, namely less than 8×10^{-6}. The other approximations consists of 14 first-order elements. Although the number of elements is more than twice the number in the second-order approximation, the first look on Figure 2.5 reveals that the first-order approximation is less accurate than the second-order one. The relative error of the position of the topmost node is approximately 10%. Nevertheless, the first impression is misleading. The curvature of this approximation is still accurate with only 0.5% error.

In the next accuracy test, depicted in Figure 2.6, the pressure is still prescribed, but it varies in space. As before, we apply a pressure for which the resulting boundary shape

---

[5] available on-line from http://libmesh.sourceforge.net

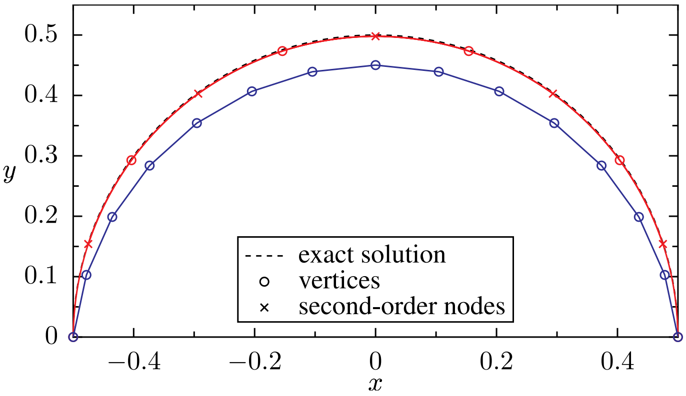

Figure 2.5. A prescribed homogeneous pressure $p_0 = 2$ bends the free surface into a half-circle with radius $1/2$. The surface tension is $\gamma = 1$. Two different approximations are presented, one with only five second-order finite elements (upper solid curve), the other with 14 first-order ones (lower solid curve). The boundary nodes are indicated either by circles, if they are vertices between two elements, or by crosses, if they are second-order nodes in the middle of a facet. The exact solution is indicated by the dashed half-circle. The initial geometry was the straight connection between the fixed endpoints. Good convergence was reached after 100 iterations with a step-size parameter $\tau = 1$. The topmost node of the second-order approximation misses its target position by a relative error of only $0.4\,\%$. The relative error of the overall curvature is even smaller, namely 8×10^{-6}. From the equally sized free-surface facets, which deviate from their average value only by a relative error of 1.2×10^{-6}, it can be seen that the stabilisation mechanism of Section 2.3.2 does not interfere. The relative error of the first-order approximation appears to be 10%. Its curvature approximation is still accurate with only 0.5% error.

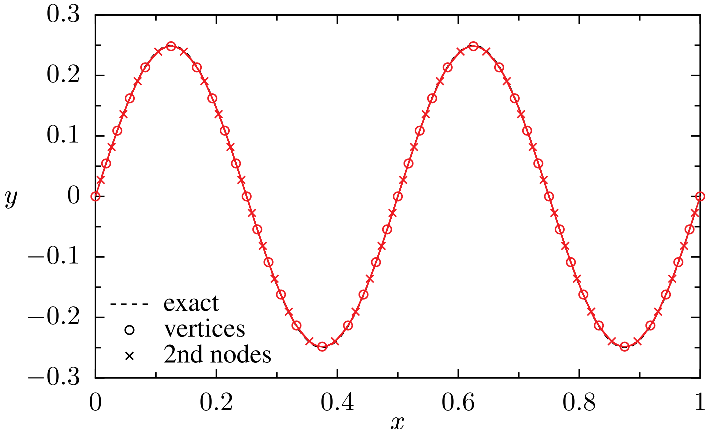

Figure 2.6. The exact sinusoidal boundary shape $y = h(x) = 0.25 \sin(4\pi x)$ with surface tension $\gamma = 1$ is well recovered by 40 second-order elements. The shape is generated by the prescribed pressure (2.92). As in Figure 2.5, the nodes at the boundary are indicated by circles and crosses. The exact solution is illustrated by the dashed curve. The initial geometry was the straight connection between the fixed endpoints of the sinus slope. Good convergence was reached after 60 iterations with a step-size parameter $\tau = 1$. The nodal positions at the maxima are off by a relative error of $0.6\,\%$. The lengths of the element sides vary only by $\pm 0.007\,\%$. This small deviation demonstrates that the mesh regularisation method does not influence the final behaviour of the free boundary.

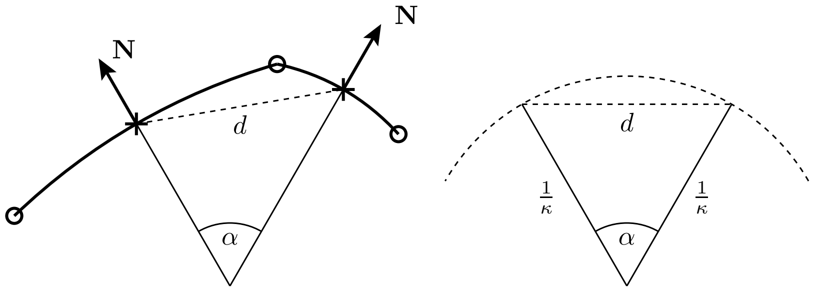

Figure 2.7. An illustration of the approximation technique for the curvature, which we refer to as *explicit reconstruction*. In the left panel, two sides of finite elements are drawn. The vertices are indicated by small circles, the second-order nodes by small crosses. The curvature of a smooth curve is defined as the change of the normal vector per arc-length of the curve. Here, the curvature at the middle node is approximated by the difference between the normal vectors at the two adjacent nodes, given in terms of the angle α. The arc-length between the two points where the normal vectors are taken is approximated by a piece of a circle with the chord length d equal to the distance of the points, see the right panel. The curvature is taken to be the inverse radius of this circle.

is known. Figure 2.6a illustrates the approximation of a sinusoidal boundary height function $y = h(x) = \alpha \sin(\beta x)$ that is caused by the pressure field

$$p(x,y) = -\gamma\kappa(x) = \gamma \frac{\alpha\beta^2 \sin(\beta x)}{[1+\alpha^2\beta^2\cos^2(\beta x)]^{3/2}} \,. \tag{2.92}$$

Again, the approximation (2.63) becomes exact, and we expect the same discretisation errors as in the previous example. The relative error of the curvature is slightly larger than in the previous example because the parts with the maximal curvature are discretised less densely. Nevertheless, the error is extremely small and can be calculated from the nodal position at a maximum, which is off by only 0.6%. The error decreases with the growing number of approximating elements.

Concerning the discretisation errors of the curvature, the accuracy test in Figure 2.6 covers already the general case. According to the construction of the algorithm, the flow exerts stress on the boundary only in normal direction. In the algorithm, it makes no difference whether this stress is of viscous nature or due to a pressure difference.

In more complicated applications of our free-surface algorithm, the solution will not be known in advance. In order to convince ourselves that the stress-balance boundary condition is indeed satisfied, we need an alternative method for calculating the approximation error of the curvature. The idea is to estimate the curvature from the discontinuous normal vectors of the element shapes. We will refer to this technique as the *explicit reconstruction* method. At each node, the normal vector of the element side is calculated. Due to the elements being second-order, this yields a valid normal vector for the nodes in the middle of the side. At vertices, where two elements meet and where the surface parametrisation is not smooth, the two normal vectors are averaged. Given these normal vectors, the curvature at a specific node is then estimated as the curvature of an appropriate circle. This circle is specified by the sector enclosed by the two normal vectors. The

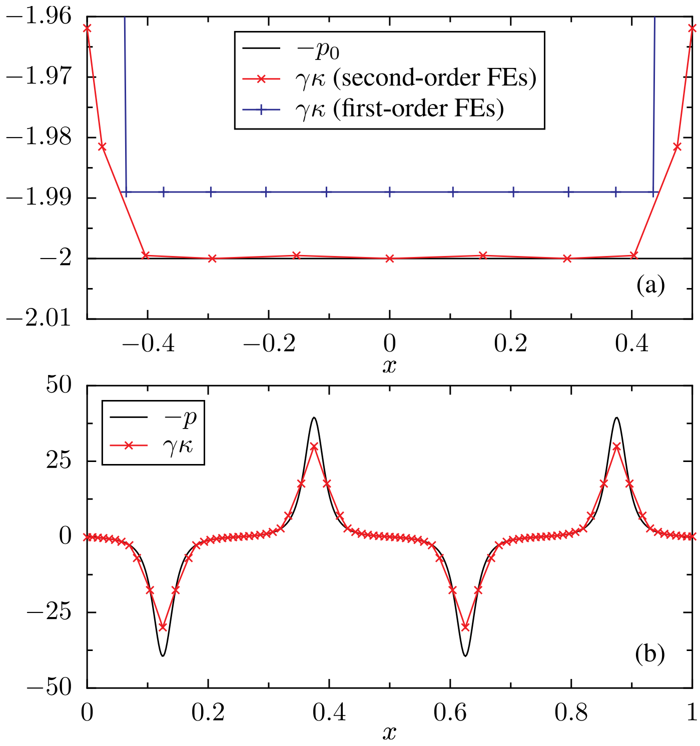

Figure 2.8. The curvature of the approximations in Figures 2.5 and 2.6, estimated from the change of the normal vectors of the finite-element sides. Panel (a) compares the estimate of the curvature for the circular approximations in Figure 2.5 with the analytical solution. The relative errors in the middle are comparable to the errors, as estimated from the global radius of the approximation. The outliers near the endpoints of the half circle are artefacts of the reconstruction method. Near the end points the normal vectors are not reliable. Panel (b) shows the same comparison for the sinusoidal slope from Figure 2.6. The large errors of approximately $25\,\%$ at the maxima and minima of the curvature clearly show the limitations of the reconstruction method. The approximation in Figure 2.6 does not indicate such a large error. Note that there are no outliers at the contact nodes of the sinus shape. Since the curvature there vanishes, the reconstructive estimate for the normal vectors becomes reliable.

angle of the sector is the angle between the normal vectors, and its chord length equals the distance between the neighbour nodes, as illustrated in Figure 2.7. This corresponds to the change of the normal vector per arc-length of the curve. By construction, the normal vector of the contact nodes at the ends of the free surface cannot be estimated correctly. The curvature estimate will therefore be less accurate for the contact nodes and their neighbour nodes.

In Figure 2.8, the curvature estimates from the explicit reconstruction technique are plotted for the shapes from Figures 2.5 and 2.6. We stress that in this figure two methods are tested simultaneously. First, the numerical solution of the problem, according to the algorithm in Section 2.3.3. Second, the explicit reconstruction mechanism which estimates the curvature. Both are subject to approximation errors. We must therefore conclude that Figure 2.8 shows an upper bound of the error. From panel 2.8a it can be seen that the second-order approximation of the constant curvature of a circle is extremely good. Apart from the outliers near the contact nodes, the curvature has a relative error less than 2.5×10^{-4}. This is not as good as the estimate obtained directly from Figure 2.5, indicating that the reconstruction technique adds a small error. The curvature errors of the sinus shape in panel 2.8b are also small; only at the maxima and minima of the curve they are large. As can be seen from the excellent approximation in Figure 2.6, the large errors in panel 2.8b are a result of the explicit reconstruction technique.

2.3.5. Stabilisation tests

In the previous section, we found the approximation in Figures 2.5 and 2.6 to consist of equally sized facets. By construction of the stabilisation mechanism, the surface then has the properties of a free surface, see Section 2.3.2. In the previous section, it has been demonstrated that the stabilised algorithm yields excellent results.

With the aid of another numerical example we will further explore the implications of the stabilising mechanism in the free-surface algorithm of Section 2.3.3. To this end, we let the algorithm solve a problem which is ill-posed for a free surface: Consider a one-dimensional surface in two spatial dimensions x and y, which is attached at its endpoints and which is subject to an externally applied stress. The stress is assumed to be such that the resulting force on the surface is a constant. The force does not depend on the position of the surface and points always in one direction, say the negative y-direction. This scenario is similar to the well-known setup of a flexible rope hanging in a homogeneous gravitational force field.

Under the specified conditions, a free surface does not possess a stationary shape. Due to its very nature, a free surface with constant surface tension can only compensate forces which are normal to the surface. The only curve which is always normal to the applied homogeneous force field, however, is a straight line. Even in the case that the straight surface is compatible with the boundary conditions, namely the position of the attachment points, it is not a solution of the problem. Because the force exerted by the surface is proportional to its curvature, it vanishes for a straight curve and cannot compensate the applied force.

Because the problem is ill-posed, we expect the free-surface algorithm without the stabilising technique to be unable of providing a meaningful result. Figure 2.9a indeed shows that this is the case. The boundary mesh, consisting of 50 first-order elements, becomes degenerate. All boundary nodes, with the exception of the two fixed attachment nodes, tend towards a single position. The movement of the nodes towards each other is due to the tangential component of the applied force. In the algorithm for the whole free-surface flow problem, such a tangential component cannot occur because of the perfect-slip boundary condition (1.16 b).

Since the stabilised free-surface algorithm in Section 2.3.3 contains some elements of the behaviour of a rubber band, it is able to compensate tangential forces. We therefore expect this algorithm to yield a stable shape for the boundary. The result can be seen in Figure 2.9b. The finite elements assume a curve which is hanging similar to a rope

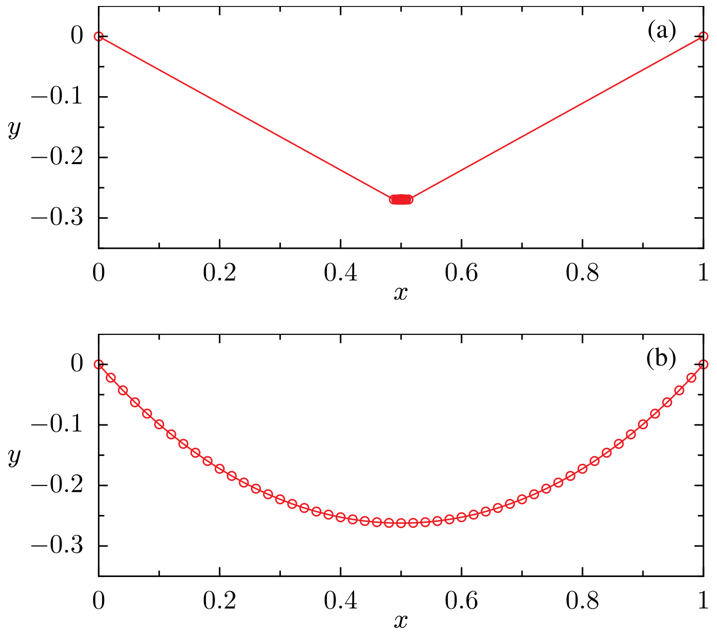

Figure 2.9. The reactions of two different free-surface algorithms on an invalid stress at the surface. Panel (a) shows the unstabilised result by the algorithm implementing the behaviour of a free surface directly. Since there is no solution to the problem due to the artificially applied stress being not the stress of a surrounding flow, this algorithm fails as expected. All mesh nodes meet in one point, except for the two fixed ones at the attachment points. Panel (b) depicts the final result by the stabilised free-surface algorithm. Its shape is an artefact due to the stabilisation, reacting on the artificial tangential force component. In both panels, the initial shape was the straight connection between the attachment points.

in a gravitational field. Note that the shape neither assumes the shape of a true rubber band, which would hang in the form of a parabola, nor is it comparable to a hanging rope, which yields a catenary curve. Instead, the shape in Figure 2.9b is caused by the artificially introduced tangential force components and has no physical meaning.

2.4. Pinned droplets in two dimensions

In this section, we compare experimental results, such as the droplet in Figure 1.2, with our numerical calculation. In the experiment, the flow inside the droplet is actuated by surface-acoustic waves due to the acoustic streaming effect. Unfortunately, the very details of the impact by the SAW on the fluid are not fully understood, as outlined in Section 1.2 of the Introduction. Therefore, we model the driving by the SAW with the aid of a body force, which is active in the fluid only. In Section 1.2 we have discussed the qualitative properties of such a body force, according to Figure 1.3. The force has been found to be active only in a long narrow region, starting at the entrance point of the SAW, and to carry the fluid along this channel. Figure 2.10 shows the force field which has been used in the numerical calculations to drive the flow. The form of the region where the force is considerably strong can be identified as a channel of approximately 70 μm to

Non-conservative force density: field lines and magnitude (in $\mathrm{N/m^3}$)

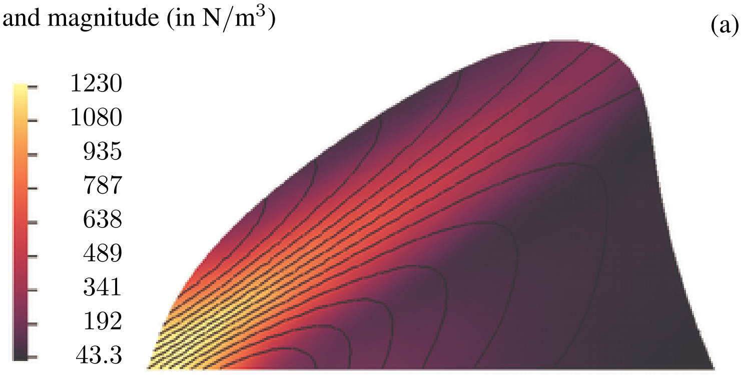

Conservative force potential (in $\mathrm{N/m^2}$)

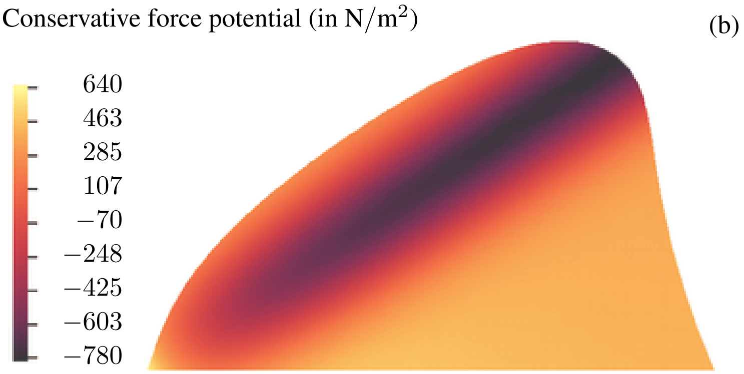

Figure 2.10. The body force that models the effect of the SAW in the droplet given in Figure 2.12. Panel (a) depicts the non-conservative part that causes the flow; (b) shows the potential of the conservative part that contributes only to the pressure. The same non-conservative force density has been used in Figure 2.13.

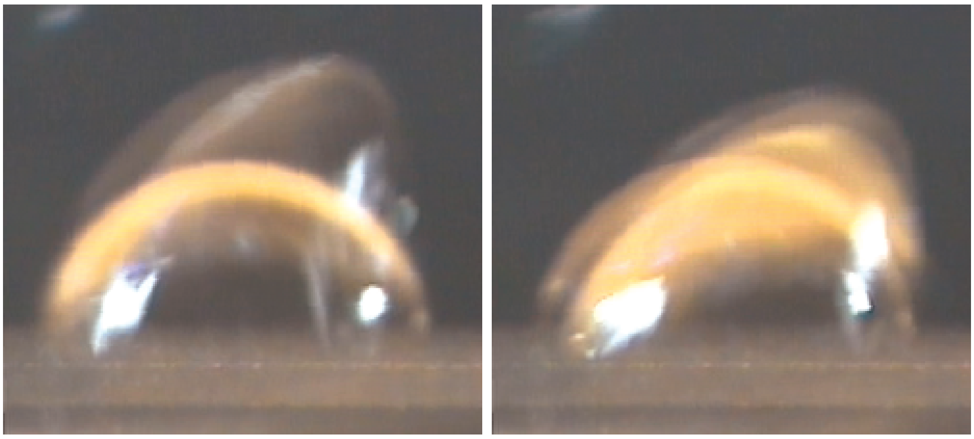

Figure 2.11. Panels (b) and (e) of Figure 1.2, depicted again for comparison with the droplet in Figure 2.12. The pictures are extracted from a film taken of the experiment. Hence, several overlapping snapshots are visible. The maximal elongation of the droplet gives an impression of the strongest deformation that occurs during the movement of this droplet. This shape of the droplet has been taken as the target shape for the droplet in Figure 2.12: In order to achieve qualitatively similar shapes, we adjusted the magnitudes of the forces in Figure 2.10 accordingly.

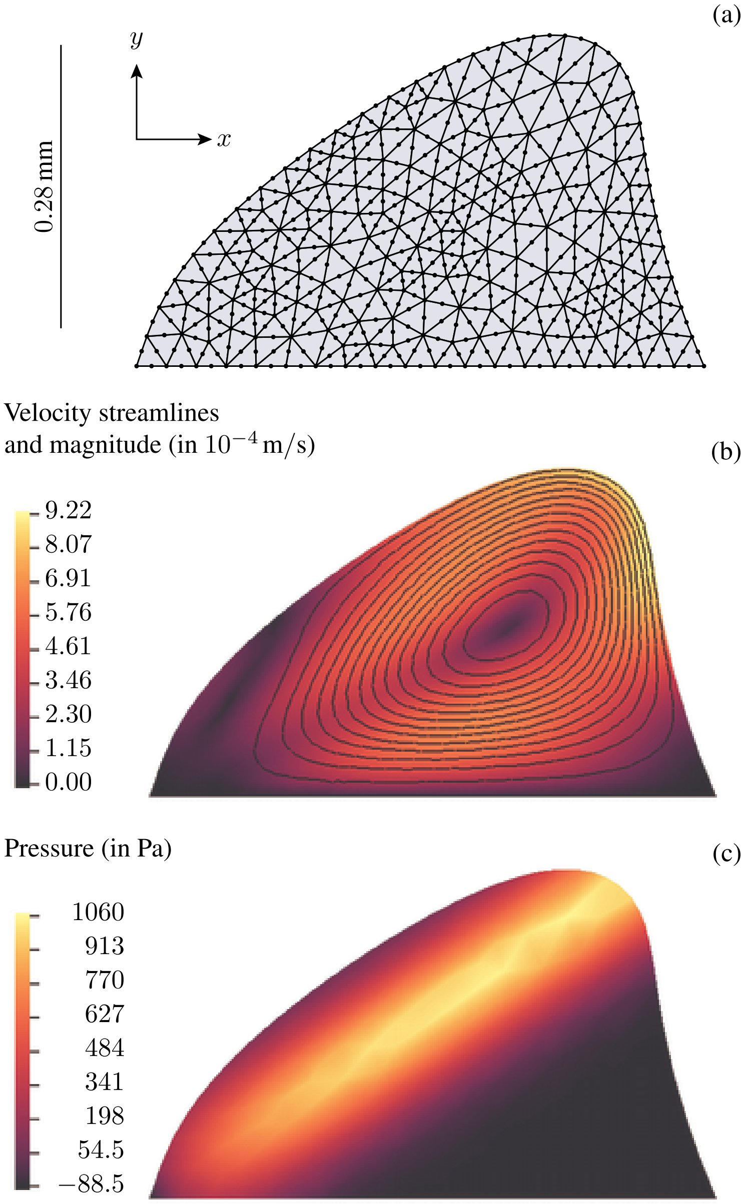

Figure 2.12. A deformed micro-droplet, sitting on a flat substrate with pinned contact-points. The deformation is due to an internal pressure and viscous flow, both caused by the body force illustrated in Figure 2.10. The material properties are those of water surrounded by air at room temperature. Its two-dimensional "volume" is that of the initial half-circle with radius 0.28 mm. Panel (a) illustrates the computational grid, consisting of second-order elements. The side-lengths of the free-surface facets differ only by $4.5 \times 10^{-5}\,\%$. Panels (b) and (c) depict the flow and the pressure, respectively. Note that the deformation is predominantly caused by the pressure which corresponds to the case that $Ca \ll Bo \approx 1$. Good convergence was reached after 7 iterations with a step-size parameter $\tau = 0.5$.

$100\,\mu$m width. Its length is larger than the system size.

The qualitative characterisation of the bulk force, providing the form of its active region, does not imply whether the force field is dominated by its conservative or by its non-conservative part. As detailed in Section 1.1.1, these two contributions have very different impacts on the resulting flow. Likewise, the deformation of the free surface can be due to either the conservative or the non-conservative part of the force. Their importance relative to the surface tension is expressed by the dimensionless numbers Ca and Bo, see Section 1.1.3. The two contributions of the bulk force can be adjusted independently in the numerical calculation, such that the resulting flow and the surface deformation obtain magnitudes which fit to the experiment in Figure 2.11. By this method, we are able to improve our understanding of the composition of the body force, and we can demonstrate that our stabilised algorithm can likewise calculate free-surface deformations which are mainly caused by a pressure ($Ca \ll Bo$), or by viscous forces ($Bo \ll Ca$).

We started the calculations with a half-circle of $0.28\,\mathrm{mm}$ radius. This corresponds to the size of the droplet that is depicted in Figures 1.2 and 2.11. The material properties are those of water and air at room temperature, i. e. $\eta = 10^{-3}\,\mathrm{kg/ms}$ and $\gamma = 72.8\times10^{-3}\,\mathrm{N/m}$. Figure 2.12 presents the surface shape as well as the flow, which are both caused by the force field in Figure 2.10. The deformed surface consists of two regions, one with negative curvature (as the initial half circle) and another one at the right flank of the droplet with positive curvature. A strongly curved region is found at the upper right part of the surface, where a large pressure is present. The computational mesh is depicted in Figure 2.12a, exhibiting that the boundary mesh is extremely regular. All facets have the same lengths, varying only by $1.5 \times 10^{-4}\,\%$. This guarantees that the behaviour of the boundary is indeed that of a free surface and is not modified by the automatic regularisation technique described in Section 2.3.2. The velocity field is depicted in Figure 2.12b, exhibiting a maximal velocity of approximately $1\,\mathrm{mm/s}$. The non-conservative part of the driving force has been tuned to yield this maximal velocity. The conservative part of the force, depicted in Figure 2.10b, gives rise to the pressure field in panel 2.12c. Its magnitude has been adjusted such that the deformation of the droplet in Figure 2.12 looks similar and is as strong as the deformation of the experimentally observed droplet in Figure 2.11.

Note that the deformation of the free surface in Figure 2.12 can only be caused by the pressure, and thus by the large conservative contribution of the driving force. The viscous forces for the observed velocities are far too weak to lead to a substantial deformation of the free surface. If the conservative part had been omitted, the resulting shape would be indistinguishable from the initial half circle. Expressed in dimensionless numbers, the parameters corresponding to the droplet in Figure 2.12 are a capillary number $Ca \approx 10^{-5}$ and a Bond number $Bo \approx 1$.

In order to prove that the presented algorithm can likewise produce stable results in the parameter regime $Bo \ll Ca$, we consider a droplet that is deformed only by viscous stress at the boundary. In Figure 2.13 we have used the same non-conservative force that is visualised in Figure 2.10, but without the conservative part. The pressure is therefore con-

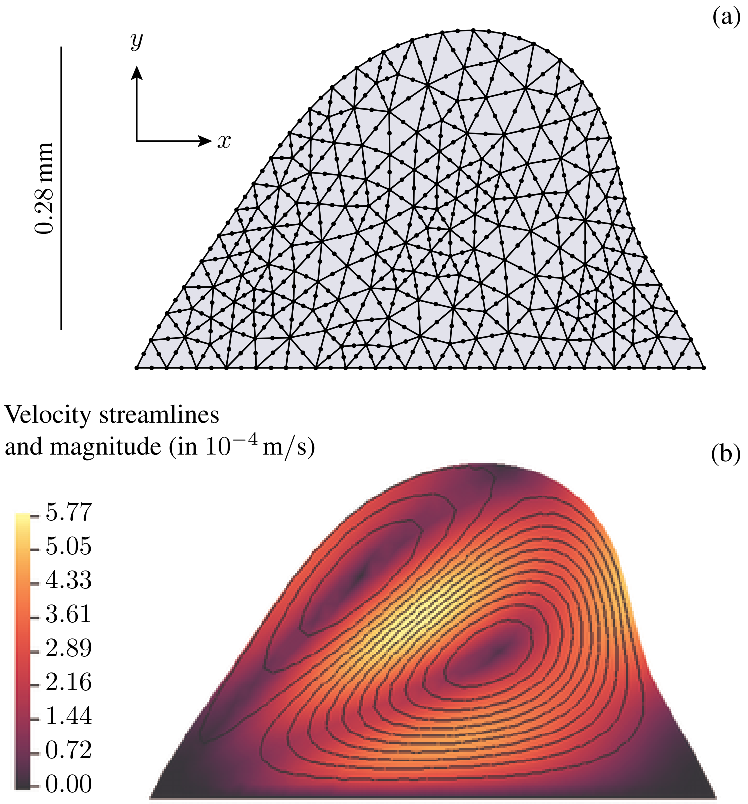

Figure 2.13. A similar micro-droplet as in Figure 2.12, deformed only by the viscous stress at the boundary. The flow is driven by the non-conservative force density depicted in Figure 2.10a. The conservative part of the force vanishes such that the pressure is constant inside the droplet. In order to obtain a comparable deformation, we have used a 10^5 times smaller surface tension than that of a water–air interface. This corresponds to the case $Bo \ll Ca \approx 1$. Good convergence was achieved after 30 iterations with $\tau = 0.1$.

stant, and $Bo = 0$. With the same water–air interface tension as in the previous example, the droplet would hardly be deformed. In order to obtain a comparable deformation as in the previous case together with $Ca \approx 1$, we have used an artificial surface tension that is 10^{-5} times smaller than the actual value for the water droplet. In this example, the mutual dependence of the interior flow and the surface deformation is much stronger than in the previous example. The velocity field generally depends stronger on the global shape of the domain than the pressure does. Therefore, the approximation (2.63) becomes questionable. It expresses the change of the stress due to changes of the surface, namely $\delta\sigma_{ij}[\delta\mathbf{t}]$ in terms of the pressure only. As a result, the numerical parameter τ had to be set to a smaller value than in the previous example, in order to reduce the step-size of the surface.

Unlike in the accuracy tests of Section 2.3.4, the form of the micro-droplets cannot be determined analytically. Nevertheless, with the aid of the explicit reconstruction technique we are able to obtain a reliable estimate for the curvature, see Figures 2.7 and 2.8. This makes it possible to prove that the free-surface boundary conditions are indeed

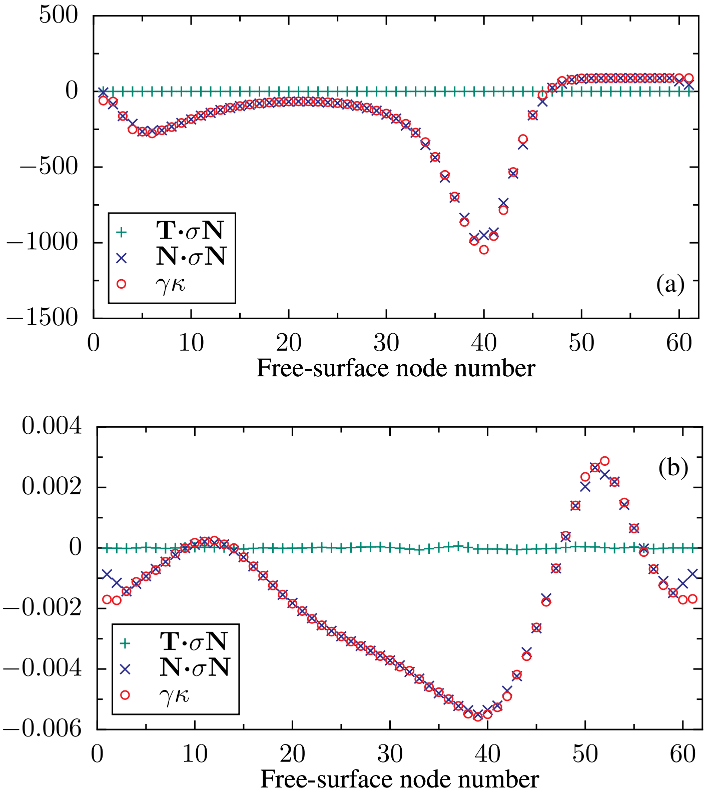

Figure 2.14. The stress balance at the free surface is found to be satisfied. Depicted are the tangential and the normal components of the forces at the surface, together with the reconstruction of the curvature for the droplets in Figure 2.12 (here, panel a) and Figure 2.13 (panel b). The tangential component of the normal stress is found to vanish, while its normal component equals the tension force. For the curvature, the reconstruction technique has been tested in Figure 2.8. The numbering of the free-surface nodes starts with the left contact point and ends with the right one. As in Figure 2.8, in the proximity of the contact nodes the reconstruction technique causes errors.

satisfied. Figure 2.14 shows all three terms in the stress balance and compares them.[6] For each node, we calculated the integrals of normal and tangential components of the normal stress, weighted by the corresponding ansatz function of the node. The tangential component vanishes, as expected. The normal component coincides well with the tension forces, where the curvature has been estimated with the explicit reconstruction technique.

Conclusions for the driving by the SAW

The two examples of this section allow an estimate of the capillary and Bond numbers of the flow in the SAW-driven water droplets. The driving mechanism with a SAW is not yet

---

[6] In the literature of free-surface numerics, one rarely finds explicit demonstrations that the stress balance is indeed satisfied at the free surface. We are convinced that readers urge to see figures like 2.14 in reviews of free-surface algorithms.

understood well enough to provide an estimate of the conservative and non-conservative parts of the resulting body force. However, Figures 2.12 and 2.13 allow the conclusion that the conservative part of the driving force must be several orders of magnitudes larger than its non-conservative part. The conservative forces for the droplet in Figure 2.12, derived from the potential of Figure 2.10b, are four to five orders of magnitudes larger than their non-conservative counterparts in Figure 2.10a. This is consistent with our finding that the surface tension in Figure 2.13 had to be reduced by five orders of magnitudes to achieve similar curvatures as in Figure 2.12.

The essence of this argument is not compromised by the fact that our numerical examples provide only two-dimensional stationary flows, while the flow in the experiment is both time-dependent and three-dimensional. The curvature in three dimensions usually differs from the two-dimensional one by a factor of two, due to the curvature radius in the second direction of the flow. Concerning the time-dependence, we stress that our argument is based on the stress-balance boundary condition, where no time derivatives enter. It must hold at any instant of time, for a time-dependent flow as well as for a stationary one.

One may be tempted to deduce the same result from the following dimensional analysis: The smallest curvature radius in photograph 1.2 of the experimentally observed droplet is 0.1mm. The flow velocity vanishes somewhere in the middle of the droplet and has a maximal value of approximately 1mm/s. A rough estimate of the viscous stress as the maximal velocity divided by the curvature radius leads to a capillary number of $Ca \approx 10^{-5}$. The Bond number must therefore be $Bo \approx 1$. This is the same order of magnitude as we have obtained from the arguments based on the two Figures 2.12 and 2.13. Of course, such a simple dimensional analysis cannot replace the detailed reasoning above. The fact that it yields the same order of magnitude, however, is another indication that our conclusion on the conservative and non-conservative parts of the body force by the SAW is correct.

2.5. Summary

In the present chapter, we have developed a combined differential geometric and variational description of the stationary flow around a free surface. The variational approach in Section 2.2 provides both the Stokes equations in the volume and the stress balance condition at the free surface from minimisations of two functionals. The respective variational formulations of the equations have been given in equations (2.41)–(2.44).

In Section 2.2.4, we found that a perfectly consistent variational description of the free-surface flow problem cannot be achieved in the given framework. This has important implications for the discretisation of the problem, namely that the discretisation order of the velocity variables and the parametrisation of the free surface should be the same. A further implication is that not all second variations of the functionals, which are necessary for the minimisations, cannot be given in explicit forms, and we have to introduce an approximation instead.

Based on the variational description of Section 2.2, in 2.3 we have provided a numerical algorithm that is capable of calculating the shape of a two-dimensional free surface deformed by a surrounding stationary viscous flow. This algorithm is designed for the tension-dominated parameter regime, where capillary and Bond numbers assume values up to unity, as described in Section 1.1.3 of the Introduction. The deformation of the free-surface shape thus can be significant, but it does not lead to a rupture of the surface. In this parameter regime, the property of the forces due to surface tension, being proportional to the curvature of the surface, is the most difficult part to treat numerically. We have overcome this problem by putting the minimisation aspects of the free energy of the surface into the focus of the algorithm.

A one-to-one discretisation of the continuous equations describing the behaviour of a free-surface emerged to be unstable. This problem was encountered also in previously existing algorithms, leading to shrinking and growing facets at the free-surface part of the computational mesh. Our solution to the problem is to allow a deviation from the behaviour of a discretised free surface towards the more stable behaviour of a discretised rubber band, see Section 2.3.2. The decisive advantage of this method is that this deviation comes into play only when the free surface has not yet assumed its final shape and as long as the facets on the boundary mesh do not have equal lengths. As the discretised surface relaxes to its target position, its behaviour also relaxes back to that of a free surface. In the numerical examples of Section 2.3.4, we show that our algorithm yields excellent approximations of free surfaces.

The parameter regime of the microfluidic flows in question is such that the behaviour of the free surface is dominated by the surface tension. This parameter regime implies that the flow inside the droplets is subject to a perfect-slip boundary condition. We propose to enforce this boundary condition in the algorithm with a constraint method.

As an application of the presented algorithm, we have calculated the deformation of pinned droplets. This deformation is caused by an internal flow, which is driven by a bulk force effectively describing the impact of an SAW. We explicitly show that the stress balance at the free surface does hold, thereby showing that our algorithm yields excellent results in the whole parameter range, $Bo \ll Ca \approx 1$ and $Ca \ll Bo \approx 1$. From the numerical solution of the flow inside the droplets and from the magnitudes of their deformation, a conclusion on the nature of the body force by the SAW can be drawn. This force must comprise a conservative part which is much stronger than the non-conservative one. Otherwise, no significant deformations would have been found. The conclusion stems from two independent observations concerning the two different droplets in Figures 2.12 and 2.13.

3. Particle accumulation

The transport of a particle in a viscous flow comprises a deterministic and a random aspect. Generally, the surrounding flow exerts stress on the particle via its boundary. If the particles are considerably small, additional fluctuations, which are inherent in the fluidic stress, lead to a noticeable Brownian motion. External forces may also be present. Generally speaking, in the theoretical description of small particles in a viscous flow, quite a number of different effects lead to small forces. Some of them annihilate each other, others sum up to noticeable effects. In the following, we will outline the main sources of particle transport.

Since we require only Cartesian coordinates in this chapter, we will simplify the notation and not differentiate between co- and contravariant tensors. Only lower indices will therefore be used. Still, indices occurring twice in a term are summed over, unless stated otherwise.

3.1. Transport of an extended particle in a flow

Point-like particles

Particles which are comparable in size and density to the fluid molecules can not be distinguished from the fluid itself. In the description of the Stokes equations, which describes the state of the flow by continuous fields, such particles can be considered as *point-particles*. They are transported with the very same velocity as the fluid. The surrounding pressure cannot affect them for the same reasons as it cannot affect the fluid elements. The pressure decouples from the velocity field, as shown in the formulation of the Stokes equations in (1.8).

Our aim in this chapter is to describe some mechanisms which allow an accumulation or a directed transport of particles in a flow. For point-like particles all accumulation effects must vanish. For small particles we expect the effects to be small as well. In the following, we will analyse several sources of such accumulation effects and try to compare them.

Extended particles

The motion of an extended particle is governed by the forces and torques that it experiences from the external body force and from the surrounding flow. When we parameterise the position of a particle P by a reference point $\mathbf{X}$, then its equations of motion read

$$m\dot{V}_i = F_i = \oint_{\partial P} \sigma_{ij} N_j \, dA + \int_P f_i \, dV \,, \tag{3.1}$$

$$\dot{L}_i = T_i = \oint_{\partial P} \varepsilon_{ijk}(x_j - X_j)\, \sigma_{kl} N_l \, dA(\mathbf{x}) + \int_P \varepsilon_{ijk}(x_j - X_j) f_k \, dV(\mathbf{x}) \,, \tag{3.2}$$

where m denotes the mass of the particle, $\mathbf{V} = \dot{\mathbf{X}}$ its velocity, and $\mathbf{L}$ its angular momentum with respect to the reference point. The force $\mathbf{F}$ and torque $\mathbf{T}$ comprise two contributions, one by the stress of the surrounding flow, which is exerted via the boundary of the particle, and a second contribution by the externally applied body force, acting on the particle volume.

Unfortunately, the stress $\sigma_{ij} N_j$ is not known if the particle motion is not known. At the same time that the particle experiences forces from the surrounding flow, it imposes time-dependent boundary conditions on this flow. These boundary conditions can be for example no-slip conditions if the particle surface is sticky. Thus the problem of the fluid flow and the particle motion cannot be split into independent parts, analogous to the free-surface problem in the previous chapter where fluid flow and shape of the free surface could not be treated independently. In order to obtain approximations of the combined flow and the particle motion, it is convenient to regard the unknown flow fields as a superposition of the *unperturbed flow* without the particle and a *correction flow* which guarantees the boundary conditions at the surface of the particle. We denote the unperturbed flow fields with the index (0) and the correction fields with (1),

$$\mathbf{u}(\mathbf{x}) = \mathbf{u}^{(0)}(\mathbf{x}) + \mathbf{u}^{(1)}(\mathbf{x}) \,, \tag{3.3}$$

$$p(\mathbf{x}) = p^{(0)}(\mathbf{x}) + p^{(1)}(\mathbf{x}) \,. \tag{3.4}$$

Of central interest is the influence of the particle size and shape on the correction flow $\mathbf{u}^{(1)}(\mathbf{x})$ and $p^{(1)}(\mathbf{x})$.

The forces on small particles in a fluid with considerable viscosity are found to be dominated by the fluidic stress. While the dependence of the total body force on the particle radius is cubic, we will find linear and quadratic dependencies for the viscous and pressure forces. In the limit of vanishing particle size, the body forces have no effect. Consequently, in the following we will omit the influence of the body force on the particle P completely. For the same reason, we will assume that the motion of the particle in the flow is overdamped (see also Purcell, 1977).

3.1.1. Zero-order forces

In contrast to a point-particle, an extended particle is able to sense pressure gradients in the surrounding flow. The pressure component of the resulting force is simply the integral of the pressure over the oriented surface. For a small sphere with radius R, we may expand the pressure into a Taylor series, leading to the force

$$\mathbf{F}^{(0)} = -\oint\limits_{S_R(\mathbf{X})} p^{(0)}\mathbf{N}\,dA = -\frac{4\pi}{3}R^3\,\boldsymbol{\nabla}p^{(0)}(\mathbf{X}) - \frac{4\pi}{30}R^5\,\boldsymbol{\nabla}\Delta p^{(0)}(\mathbf{X}) + \cdots\,, \tag{3.5}$$

where $S_R(\mathbf{X})$ is the spherical surface with radius R around the point $\mathbf{X}$ in three-dimensional space. The derivatives of $p^{(0)}$ are evaluated at the centre of the sphere. The sign in equation (3.5) has been chosen such that $\mathbf{F}^{(0)}$ denotes the force exerted by the pressure field on the particle. The normal vector points out of the sphere.

It is likewise possible to carry out the integral of the viscous stress by the zero-order velocity field over the surface of the particle. This quantity, however, is meaningless, because this velocity field does not obey the correct boundary conditions. Instead, the zero- and first-order contributions by the flow velocity have to be calculated together.

3.1.2. First-order forces

In the past, several different approaches have been used to calculate the viscous force on a small spherical particle. The first approach is due to Stokes, who considered a sphere moving through an unbounded viscous fluid which rests otherwise. The motion of the sphere is caused by a time-independent external force. It gives rise to an axisymmetric correction flow which Stokes calculated analytically with the aid of a special stream function (for the derivation see Happel and Brenner, 1991, Chapter 4). The linear relations between the force $\mathbf{F}$ on a particle and its velocity $\dot{\mathbf{X}}$, and between the torque $\mathbf{T}$ and its angular velocity $\dot{\boldsymbol{\varphi}}$ are the well-known *Stokes' laws of resistance* (Happel and Brenner, 1991),

$$\mathbf{F}^{(1)} = -6\pi\eta R\,\dot{\mathbf{X}}\,, \tag{3.6}$$

$$\mathbf{T}^{(1)} = -8\pi\eta R^3\dot{\boldsymbol{\varphi}}\,. \tag{3.7}$$

That the surrounding fluid must be at rest, apart from the moving sphere, is a drawback which has partially been overcome by the methods of Oseen (1913, 1927) and Faxén (1921). The resulting equations are known as *Faxén's theorems for translational and rotational motion*,

$$\dot{\mathbf{X}} = -\frac{1}{6\pi\eta R}\mathbf{F}^{(1)} + \mathbf{v}^{(0)}(\mathbf{X}) + \frac{1}{6}R^2\Delta\mathbf{v}^{(0)}(\mathbf{X})\,, \tag{3.8}$$

$$\dot{\boldsymbol{\varphi}} = -\frac{1}{8\pi\eta R^3}\mathbf{T}^{(1)} + \frac{1}{2}\boldsymbol{\nabla}\times\mathbf{v}^{(0)}(\mathbf{X})\,. \tag{3.9}$$

Faxén's theorems express the forces and torques on the particle, which are due to the correction field, in terms of the unperturbed flow. An overview of the derivation can be found in the books by Dhont (1996) and by Pozrikidis (1992). Equations (3.8) and (3.9) express the motion of the sphere in terms of the velocity field at its centre only. This is a decisive advantage, since the boundary conditions at the particle surface are already contained in the equations.

In the following, it will be of importance to know the precise meaning of the "unperturbed" velocity field $\mathbf{v}^{(0)}$ in Faxén's theorems. This becomes especially important in the presence of boundaries which confine the fluid and pose boundary conditions on the Stokes equations. In the following paragraphs, we will therefore derive equation (3.8) in a short and elegant way, finding that $\mathbf{v}^{(0)}$ is not completely unperturbed.

Faxén's theorem of translational motion

Two independent velocity fields $v_i(\mathbf{x})$ and $\bar{v}_i(\mathbf{x})$, each solutions of the homogeneous Stokes equations with arbitrary boundary conditions, satisfy the well-known *reciprocal identity* (Lamb, 1932),

$$0 = \left(\bar{v}_i \sigma_{ij} - v_i \bar{\sigma}_{ij}\right)_{,j} . \tag{3.10}$$

The velocity field $v_i(\mathbf{x})$ with the corresponding stress tensor $\sigma_{ij}(\mathbf{x})$ is the sought solution of the Stokes equation in the presence of an immersed spherical particle. The flow denoted with the bar is unspecified. As the boundary conditions in (3.10) are arbitrary, we may replace the latter by the fundamental solution of the Stokes equation,

$$0 = \frac{\partial}{\partial x_j}\left[\mathcal{K}_{ik}(\mathbf{x}-\mathbf{y})\sigma_{ij}(\mathbf{x}) - v_i(\mathbf{x})\mathcal{T}_{ijk}(\mathbf{x}-\mathbf{y})\right] , \tag{3.11}$$

as long as we do not touch the poles at $\mathbf{x} = \mathbf{y}$. The fundamental solutions for the velocity and the stress tensor depend only on the difference vector $\mathbf{r} = \mathbf{x} - \mathbf{y}$ and have the form (see Appendix D),

$$\mathcal{K}_{ik}(\mathbf{r}) = \frac{1}{8\pi\eta}\left(\frac{\delta_{ik}}{r} + \frac{r_i r_k}{r^3}\right) , \tag{3.12}$$

$$\mathcal{T}_{ijk}(\mathbf{r}) = -\frac{3}{4\pi}\frac{r_i r_j r_k}{r^5} . \tag{3.13}$$

Equation (3.11) is integrated over the fluid domain Ω, where no external forces are active. The divergence in equation (3.11) is then cast into an integral over the boundary of Ω. For this integration we have to distinguish between points $\mathbf{y}$ residing outside of Ω and not on its boundary $\partial\Omega$ (that is outside of the closure $\overline{\Omega}$), those points in the interior $\mathring{\Omega}$ and those points on the boundary $\partial\Omega$. For a point $\mathbf{y}$ not in $\overline{\Omega}$, the fundamental solutions are regular, leading to

$$0 = \oint_{\partial\Omega} dA(\mathbf{x}) N_j(\mathbf{x}) \left[\mathcal{K}_{ik}(\mathbf{x}-\mathbf{y})\,\sigma_{ij}(\mathbf{x}) - \mathcal{T}_{ijk}(\mathbf{x}-\mathbf{y})\,v_i(\mathbf{x})\right] . \tag{3.14}$$

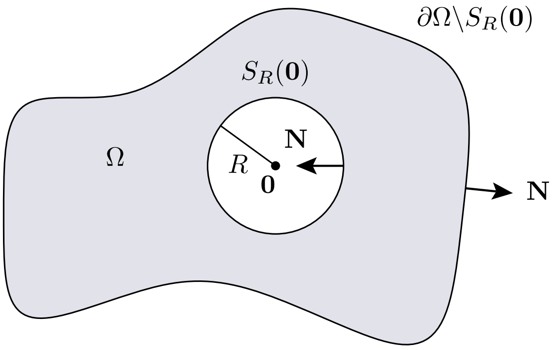

Figure 3.1. The fluid domain Ω and its boundaries, as used for the derivation of Faxén's theorem of translational motion in equations (3.14)–(3.29). The spherical hole in Ω is the rigid particle. The normal vectors are defined to point out of the fluid domain.

If the point $\mathbf{y}$ lies inside Ω, however, the integration over the pole of $\mathcal{T}_{ijk}$ results in the velocity at $\mathbf{y}$ (see Appendix D and Pozrikidis 1992),

$$v_k(\mathbf{y}) = \oint_{\partial\Omega} dA(\mathbf{x})\, N_j(\mathbf{x}) \big[\mathcal{K}_{ik}(\mathbf{x}-\mathbf{y})\, \sigma_{ij}(\mathbf{x}) - \mathcal{T}_{ijk}(\mathbf{x}-\mathbf{y})\, v_i(\mathbf{x})\big] \,. \tag{3.15}$$

The boundary $\partial\Omega$ is assumed to consist of two parts. One is the surface of a spherical particle of radius R, the other is the boundary of the fluid container, which is subject to externally prescribed boundary conditions. The fluid domain Ω and its boundary are illustrated in Figure 3.1 to make the orientation of the normal vectors clear. Without loss of generality, we choose the origin of the coordinate system to be at the centre of the sphere. By imposing no-slip boundary conditions at the surface of the particle, the fluid velocity there is given by a rigid motion of the particle,

$$v_i(\mathbf{x}) = V_i + \varepsilon_{ijk}\omega_j x_k \,. \tag{3.16}$$

The vector V_i is the velocity of the particle, and ω_i describes its rotation around the origin. In order to incorporate these boundary conditions, we integrate equation (3.14) over the particle surface $S_R(\mathbf{0})$ and obtain the lengthy equation

$$\begin{aligned} 0 = &\oint_{S_R(\mathbf{0})} dA(\mathbf{y}) \oint_{S_R(\mathbf{0})} dA(\mathbf{x})\, N_j(\mathbf{x}) \big[\mathcal{K}_{ik}(\mathbf{x}-\mathbf{y})\, \sigma_{ij}(\mathbf{x}) - \mathcal{T}_{ijk}(\mathbf{x}-\mathbf{y})\, v_i(\mathbf{x})\big] \\ &+ \oint_{S_R(\mathbf{0})} dA(\mathbf{y}) \oint_{\partial\Omega\backslash S_R(\mathbf{0})} dA(\mathbf{x})\, N_j(\mathbf{x}) \big[\mathcal{K}_{ik}(\mathbf{x}-\mathbf{y})\, \sigma_{ij}(\mathbf{x}) - \mathcal{T}_{ijk}(\mathbf{x}-\mathbf{y})\, v_i(\mathbf{x})\big] \,. \end{aligned} \tag{3.17}$$

Unfortunately, the integrands become singular where $\mathbf{x} = \mathbf{y}$, leading to improper integrals. We avoid this complication by performing the integral with respect to $dA(\mathbf{x})$ in (3.17), which corresponds to the integral in (3.14), not over the surface of the particle but over a slightly extended sphere $S_{R+\varepsilon}(\mathbf{0})$ and then take the limit $\varepsilon \to 0$ after both integrations have been performed. This is consistent with the requirement for (3.14) that the point $\mathbf{y}$ must be outside of $\overline{\Omega}$. The integrals over $\mathcal{K}_{ik}$ can be simplified with a result that can be found in the books by Dhont (1996, Appendix A of Chapter 5) and by Pozrikidis (1992, problem 2.3.9), see also equation (D.11) in Appendix D,

$$\oint\limits_{S_R(\mathbf{0})} \mathcal{K}_{ik}(\mathbf{x}-\mathbf{y})\,dA(\mathbf{y}) = \frac{2R}{3\eta}\delta_{ik}\,, \tag{3.18}$$

where $\mathbf{x}$ is a point on the sphere $S_R(\mathbf{0})$, and thus $x = y$. On the outer boundary of the fluid, $\partial\Omega\backslash S_R(\mathbf{0})$, we have $x > y$ and therefore use the more general result (cf. equation D.11 of Appendix D),

$$\oint\limits_{S_R(\mathbf{0})} \mathcal{K}_{ik}(\mathbf{x}-\mathbf{y})\,dA(\mathbf{y}) = \frac{R}{2\eta}\left[\delta_{ik}\Big(\frac{R}{x}+\frac{1}{3}\frac{R^3}{x^3}\Big)+\frac{x_i x_k}{x^2}\Big(\frac{R}{x}-\frac{R^3}{x^3}\Big)\right]. \tag{3.19}$$

This identity can be further simplified by noticing that the right-hand side is given by the fundamental solution for the velocity and its Laplacian, see equation (D.13) in Appendix D,

$$\oint\limits_{S_R(\mathbf{0})} \mathcal{K}_{ik}(\mathbf{x}-\mathbf{y})\,dA(\mathbf{y}) = 4\pi R^2\Big(\mathcal{K}_{ik}(\mathbf{x})+\frac{R^2}{6}\Delta\mathcal{K}_{ik}(\mathbf{x})\Big)\,. \tag{3.20}$$

A similar relation can be found for the integral of $\mathcal{T}_{ijk}$ if $x > y$, see equations (D.12) and (D.14) in Appendix D,

$$\begin{aligned}\oint\limits_{S_R(\mathbf{0})} &\mathcal{T}_{ijk}(\mathbf{x}-\mathbf{y})\,dA(\mathbf{y}) \\ &= -\frac{R^4}{x^4}\Big(\delta_{ij}\frac{x_k}{x}+\delta_{ik}\frac{x_j}{x}+\delta_{jk}\frac{x_i}{x}\Big)+\Big(5\frac{R^4}{x^4}-3\frac{R^2}{x^2}\Big)\frac{x_i x_j x_k}{x^3} && (3.21)\\ &= 4\pi R^2\Big(\mathcal{T}_{ijk}(\mathbf{x})+\frac{R^2}{6}\Delta\mathcal{T}_{ijk}(\mathbf{x})\Big)\,. && (3.22)\end{aligned}$$

The limiting value for $x \to y$ is given by

$$N_j(\mathbf{x})\oint\limits_{S_R(\mathbf{0})} \mathcal{T}_{ijk}(\mathbf{x}-\mathbf{y})\,dA(\mathbf{y}) = \delta_{ik}\,, \tag{3.23}$$

where we have already reduced the tensorial rank by multiplying with the normal vector $N_j(\mathbf{x})$ occurring in (3.17).

In order to simplify equation (3.17), we first carry out the integrations with respect to $dA(\mathbf{y})$, making use of the identities (3.18) and (3.23). Then, we perform the limit $\varepsilon \to 0$ which commutes with the other integration. At this point it is crucial to carry out the integrals over spheres with different radii. If we had taken the same radius for both spheres, we would have obtained $\delta_{ik}/2$ instead of the right-hand side of equation (3.23). The integral of $\mathcal{T}_{ijk}$ over the sphere for all three possibilities $x < R$, $x = R$, and $x > R$ is provided in equation (D.12) in Appendix D. Making use of the boundary condition (3.16), the first terms of equation (3.17) can be identified as the force and the velocity of the particle, respectively. They are given by

$$\lim_{\varepsilon\to 0} \oint\limits_{S_R(\mathbf{0})} dA(\mathbf{y}) \oint\limits_{S_{R+\varepsilon}(\mathbf{0})} dA(\mathbf{x}) \mathcal{K}_{ik}(\mathbf{x}-\mathbf{y})\,\sigma_{ij}(\mathbf{x})\,N_j(\mathbf{x}) \\ = \frac{2R}{3\eta} \oint\limits_{S_R(\mathbf{0})} dA(\mathbf{x}) \sigma_{kj}(\mathbf{x})\,N_j(\mathbf{x}) = -\frac{2R}{3\eta} F_k^{(1)} \,, \tag{3.24}$$

$$\lim_{\varepsilon\to 0} \oint\limits_{S_R(\mathbf{0})} dA(\mathbf{y}) \oint\limits_{S_{R+\varepsilon}(\mathbf{0})} dA(\mathbf{x}) \mathcal{T}_{ijk}(\mathbf{x}-\mathbf{y})\,v_i(\mathbf{x})\,N_j(\mathbf{x}) \\ = \oint\limits_{S_R(\mathbf{0})} dA(\mathbf{x}) v_k(\mathbf{x}) = 4\pi R^2 V_k \,. \tag{3.25}$$

Here, we have used

$$F_k^{(1)} = -\oint\limits_{S_R(\mathbf{0})} dA\,\sigma_{kj} N_j \,, \tag{3.26}$$

which is the total force exerted on the particle by the surrounding flow. Note that the normal vector points into the particle, as is visualised in Figure 3.1.

With the aid of the same helper identities (3.18) and (3.23), we may as well simplify the remaining two integrals of (3.17). Instead of (3.17), we obtain the more useful relation

$$0 = -\frac{2R}{3\eta} F_k^{(1)} - 4\pi R^2 V_k \\ + 4\pi R^2 \oint\limits_{\partial\Omega\setminus S_R(\mathbf{0})} dA(\mathbf{x})\,\sigma_{ij}(\mathbf{x})\,N_j(\mathbf{x}) \Big(\mathcal{K}_{ik} + \frac{R^2}{6}\Delta\mathcal{K}_{ik}\Big)(\mathbf{x}) \\ - 4\pi R^2 \oint\limits_{\partial\Omega\setminus S_R(\mathbf{0})} dA(\mathbf{x})\,v_i(\mathbf{x})\,N_j(\mathbf{x}) \Big(\mathcal{T}_{ijk} + \frac{R^2}{6}\Delta\mathcal{T}_{ijk}\Big)(\mathbf{x}) \,. \tag{3.27}$$

A look on the integral representation (3.15) of the velocity field helps to understand the remaining integrals in (3.27). In both integrals of (3.27) the integral kernels $\mathcal{K}_{ik}$ and $\mathcal{T}_{ijk}$ occur together with their Laplacian, scaled with $R^2/6$. Thus, if we define a velocity field $\mathbf{v}^{(0)}$ by a similar integral as in (3.15) but without the boundary of the particle,

$$v_k^{(0)}(\mathbf{y}) := \oint\limits_{\partial\Omega\setminus S_R(\mathbf{0})} dA(\mathbf{x})\,N_j(\mathbf{x}) \big[\mathcal{K}_{ik}(\mathbf{x}-\mathbf{y})\,\sigma_{ij}(\mathbf{x}) - \mathcal{T}_{ijk}(\mathbf{x}-\mathbf{y})\,v_i(\mathbf{x})\big] \,, \tag{3.28}$$

then the two remaining integrals in (3.27) yield the velocity $\mathbf{v}^{(0)}$ plus $R^2/6$ times its Laplacian, both evaluated at the centre of the sphere. Altogether, we obtain for (3.27)

$$0 = -\frac{2R}{3\eta} F_k^{(1)} - 4\pi R^2 V_k \; + \; 4\pi R^2 \Big(v_k^{(0)}(\mathbf{0}) + \frac{R^2}{6} \Delta v_k^{(0)}(\mathbf{0}) \Big) \,, \tag{3.29}$$

which is exactly Faxén's theorem of translational motion (3.8). This theorem generalises the result by Stokes, where the flow of the fluid is caused only by the motion of the sphere. Here, the fluid may perform a motion even in the absence of the particle. This flow is driven by boundary conditions at the outer boundary $\partial\Omega\backslash S_R(\mathbf{0})$. From the above derivation, we now have obtained a better understanding of the "unperturbed" velocity field $\mathbf{v}^{(0)}$ which enters Faxén's theorems. The definition (3.28) clearly indicates that for (3.29) to be valid, the "unperturbed" velocity field $\mathbf{v}^{(0)}$ must be defined in terms of the boundary values of the "true" velocity field $\mathbf{v}(\mathbf{x})$ and the corresponding stress. Therefore, $\mathbf{v}^{(0)}$ is not precisely the flow velocity which we would find in the complete absence of the particle. It is the flow without the particle, which produces the very same velocity and stress at the outer boundary as the flow with the particle does.

Note that the identities (3.20) and (3.22) are due to the spherical shape of the particle. For a differently shaped particle they do not hold. Faxén's theorem (3.29) has thus been found to be exact not only in the limit of vanishing radius but for spheres with arbitrary radii. Unfortunately, in order to obtain $\mathbf{v}^{(0)}$, the whole Stokes equation with proper boundary conditions also on the particle surface has to be solved. In Section 3.2 below, we will only need the property of $\mathbf{v}^{(0)}$ being a solenoidal vector field. If more details of the force on the particle are needed, then Faxén's theorem (3.29) can only serve as an approximation, with the truly unperturbed flow inserted as $\mathbf{v}^{(0)}$. If the particle is far away from the outer boundary, then the difference between the boundary values of a truly unperturbed flow and the boundary values of $\mathbf{v}^{(0)}$ can indeed be negligibly small. If the particle approaches the outer boundary, however, the flow near the boundary is too much influenced by the particle. The particle exerts additional stress on the boundary via the fluid in between. This *hydrodynamic interaction* between particle and boundary makes the description of particles near boundaries extremely difficult (Kim and Karilla, 1991; Pozrikidis, 1992).

Another requirement of (3.27) is that the flow must be stationary, or as an approximation, nearly stationary. A truly stationary flow is a very restrictive assumption concerning particle motion. The Stokes equations are then transformed into the co-moving reference frame of the particle centre, but in this time-dependent coordinate system the outer boundaries of the fluid may not change in time. The whole setup must therefore be invariant under the particle motion. This is the case for a particle moving along the axis of an infinitely long pipe or along the symmetry plane between two infinite parallel walls. These problems have been analysed analytically already in the original works by Faxén (1921, 1922, 1923, see also Oseen 1927). Numerical calculations of the motion performed by a sphere between parallel plane walls have been performed by Staben et al. (2003) even for small distances between sphere and wall. For very slow flows, however, the stationary Stokes equations may be satisfied well enough, such that Faxén's theorem (3.29) is a good approximation. Then, the whole motion of the particle is composed of a series of instantaneous snapshots, each satisfying the stationary equations.

A number of further extensions of Faxén's theorems have been published (Kim and Karilla, 1991). Pozrikidis (1989) describes particles and droplets in oscillating viscous flows, and Shu and Chwang (2001) consider particles which translate through rotating flows.

3.1.3. Higher-order forces

If several particles are immersed in a flow, they cause a common correction field which is generally not the superposition of separate correction fields. This poses the main difficulty of describing fluids that are heavily loaded with particles (see for example Dhont, 1996; Kim and Karilla, 1991; Doi and Edwards, 1986). This thesis, however, is concerned only with dilute particle dispersions, where the single-particle correction fields are already small, such that the hydrodynamic interaction between adjacent particles does not come into play.

3.1.4. Random forces

At room temperature, a fluid is always subject to thermal fluctuations (Landau and Lifschitz, 1966). The stress at the boundary of an immersed particle then comprises a deterministic and a fluctuating contribution. For small particles, these random forces can be of the order of the deterministic forces and lead to a Brownian motion of the particles. The description of the random motion of immersed particles in a fluid at thermal equilibrium has been ascribed to Einstein (1905). A little earlier, Sutherland (1905) published the same result (cf. also to Hänggi and Marchesoni 2005). Sutherland and Einstein argue that in a distribution of particles the osmotic pressure is compensated by the sum of the drag forces. If the result of Stokes (3.6) is used for the latter, this leads to the celebrated *Sutherland–Einstein relation* for the diffusion coefficient of the distribution of particles with radius R at temperature T,

$$D = \frac{k_{\mathrm{B}}T}{6\pi\eta R}\,. \tag{3.30}$$

The diffusion coefficient is used in the Fokker–Planck equation for the probability distribution $\rho(\mathbf{x})$ of the particle centre,

$$\partial_t \rho(\mathbf{X},t) = -\operatorname{div}\big(\mathbf{d}(\mathbf{X})\rho(\mathbf{x},t)\big) + D\Delta\rho(\mathbf{X},t)\,, \tag{3.31}$$

where the deterministic drift velocity of the particle is denoted by $\mathbf{d}(\mathbf{X})$. An equivalent dependence of the diffusion constant on R and T was derived by von Smoluchowski (1906) using microscopic considerations, different from Sutherland and Einstein. He arrived at a diffusion constant D which is $\sqrt{64/27}$ times larger than in equation (3.30).

The drift velocity depends on the forces which act on the particle. In order to find the dependence of $\mathbf{d}(\mathbf{X}(t))$ on the forces $\mathbf{F}(t)$ which have been analysed in the previous sections, we consider the Langevin equation for a particle of mass m,

$$m\ddot{\mathbf{X}}(t) = \mathbf{F}(t) + \sqrt{2d}\,\boldsymbol{\xi}(t)\,, \tag{3.32}$$

and search for the overdamped limit. The random force $\boldsymbol{\xi}(t)$ is assumed to be white noise, satisfying

$$\big\langle \xi_i(t) \big\rangle = 0\,, \tag{3.33}$$

$$\big\langle \xi_i(t)\xi_j(s) \big\rangle = \delta_{ij}\delta(t-s)\,. \tag{3.34}$$

The value of the noise strength d can be determined in several ways. One possible line of argumentation employs the Langevin equation (Kramers, 1940; Risken, 1984) together with the Sutherland–Einstein relation (3.30). The fluid is assumed to be in thermal equilibrium, that is without external driving and without any unperturbed flow. In this case, the force $\mathbf{F}$ in (3.32) reduces to the drag force given by the Stokes relation, yielding the Langevin equation

$$m\ddot{\mathbf{X}}(t) = -6\pi\eta R\dot{\mathbf{X}}(t) + \sqrt{2d}\,\boldsymbol{\xi}(t)\,, \tag{3.35}$$

with the long-time expectation values

$$\lim_{t\to\infty}\big\langle \dot{X}_i(t) \big\rangle = 0\,, \tag{3.36}$$

$$\lim_{t\to\infty}\big\langle \dot{X}_i(t)\dot{X}_j(s) \big\rangle = \delta_{ij}\,\delta(t-s)\,\frac{d}{6\pi\eta Rm}\,. \tag{3.37}$$

The same long-time limit is given at thermal equilibrium by the temperature,

$$\big\langle v_i v_j \big\rangle = \delta_{ij}\frac{k_\mathrm{B}T}{m}\,, \tag{3.38}$$

if the average flow vanishes (cf. Landau and Lifschitz, 1971, § 114). Equations (3.37) and (3.38) yield the result

$$d = 6\pi\eta R\,k_\mathrm{B}T\,. \tag{3.39}$$

This is the diffusion constant of the velocity at thermal equilibrium. We will use the very same diffusion constant also for the driven case, where the fluid performs a non-vanishing average flow. This approximation is expected to hold for sufficiently small velocity gradients (see Rubí and Bedeaux, 1988; Miyazaki and Bedeaux, 1995, and references therein). For small particles which are immersed in water the inertial term on the left-hand side of the Langevin equation (3.32) is negligible (Purcell, 1977). The particle thus performs an overdamped motion. In order to obtain the overdamped Langevin equation, we collect the zero- and first-order forces from equations (3.5) and (3.29) above and extract the particle velocity. We thus write the force on the particle as

$$\mathbf{F}(t) = 6\pi\eta R\left[-\dot{\mathbf{X}}(t) + \mathbf{d}(t)\right]\,, \quad \text{with} \tag{3.40}$$

$$\begin{aligned}\mathbf{d}(t) = {} & \mathbf{v}^{(0)}\big(\mathbf{X}(t)\big) + \frac{R^2}{6}\Delta\mathbf{v}^{(0)}\big(\mathbf{X}(t)\big) \\ & - \frac{2R^2}{9\eta}\boldsymbol{\nabla}p^{(0)}\big(\mathbf{X}(t)\big) - \frac{2R^4}{90\eta}\boldsymbol{\nabla}\Delta p^{(0)}\big(\mathbf{X}(t)\big) + \cdots\end{aligned} \tag{3.41}$$

The quantity $\mathbf{d}(t)$ is the *drift velocity* of the particle, which will play a central role in the following sections. The first line of equation (3.41) corresponds to the first-order forces by the flow $\mathbf{v}^{(0)}$, taken from Faxén's theorem of translational motion (3.29). The second line contains the zero-order forces from (3.5), which are caused by the externally induced pressure field $p^{(0)}$. After setting m to zero, the overdamped dynamics of the particle reads

$$\dot{\mathbf{X}}(t) = \mathbf{d}\big(\mathbf{X}(t)\big) + \sqrt{2D}\,\boldsymbol{\xi}(t)\,, \tag{3.42}$$

which is the Langevin equation equivalent to the Fokker–Planck equation (3.31). In the following, we will focus on the long-time limit of the particle distribution, which is governed by the stationary Fokker–Planck equation

$$0 = -\operatorname{div}\big(\mathbf{d}\,\rho\big) + D\Delta\rho\,. \tag{3.43}$$

3.2. Particle accumulation at boundaries

An inhomogeneous distribution of particles, exhibiting regions more densely filled with particles than other regions, is referred to as an *accumulation* of particles. The Fokker–Planck equation (3.43) with an arbitrary drift field $\mathbf{d}(\mathbf{X})$ may have such inhomogeneous solutions in two different cases. We will distinguish the two accumulation mechanisms by means of the boundaries being involved in the effect or not. The role of the boundaries is explained by the following observation: Consider the case of a solenoidal drift velocity field $\mathbf{d}(\mathbf{X})$. Then, the homogeneous particle distribution $\rho(\mathbf{X}) = \mathit{const}$ is the trivial solution of the stationary Fokker–Planck equation (3.43). Whether this solution is the physically realised particle distribution, depends only on the boundary conditions.

Volume effect

The first mechanism is a pure *volume effect*, occurring even if the fluid is not enclosed by boundaries at all. Since boundary conditions do not come into play, the volume effect depends only on the property of the drift velocity field $\mathbf{d}(\mathbf{X})$ being solenoidal or not. This attribute of the drift field, being solenoidal or not, depends on the shape of the particle. In the previous section we found that the special case of a spherical particle admits a solenoidal drift velocity. A particle of complicated shape, however, generally gives rise to a drift field with non-vanishing divergence. Examples can be found in the literature (Doi and Makino, 2005a,b; Kim and Karilla, 1991; Doi and Edwards, 1986). Especially chiral particles experience drift fields which are not solenoidal. As a minimal model for a chiral particle in two dimensions, a rigid combination of three small spherical particles of different radii has been used (Kostur, Schindler, Talkner & Hänggi, 2006). If all radii are different, then the particle is not invariant under reflection and does not coincide with its chiral partner. Such a chiral particle is extremely sensitive to the surrounding flow. When immersed in a fluid flowing in an array of small eddies, rotating clockwise and counter-clockwise, its motion exhibits complicated attractors, which depend on the sense of rotation of the specific eddy. In combination with thermal noise, these attractors lead to a relative accumulation of chiral particles in the eddies of fitting sense of rotation.

The influence of the shape of a particle on its motion decreases with its size. In the limit of vanishing size we may thus assume all particles to be spherical and make use of Faxén's theorems. The drift velocity $\mathbf{d}(\mathbf{X})$ is then given by equation (3.41). The leading-order term in (3.41) is the first one, the velocity field $\mathbf{v}^{(0)}(\mathbf{X})$. Since it is a solenoidal vector field, we cannot expect a volume effect.

One might object that there are forces on the particle due to the hydrodynamic interaction between particle and wall, which might eventually give rise to an non-trivial particle distribution. For slowly moving spherical particles, for which equation (3.41) is a good approximation of the drift velocity, hydrodynamic interactions do not help obtaining a volume effect. Although we cannot calculate the flow velocity $\mathbf{v}^{(0)}$ in equation (3.29) explicitly, we nevertheless know that it is solenoidal, which is the relevant information here. As in the previous section, there might be effects due to the hydrodynamic interaction of a particle with a curved wall or for a particle moving fast. In these cases, equation (3.29) does not apply.

The next-order terms contributing to $\mathbf{d}(\mathbf{X})$ in (3.41) are the ones proportional to R^2. The Laplacian of the velocity field is also solenoidal, not giving rise to any volume effect. Whether also the pressure terms in (3.41) have vanishing divergence or not, depends on the divergence of the body force $\mathbf{f}$ in the Stokes equation (1.6), giving rise to the pressure: In a flow driven by a homogeneous force, or in a pressure-driven flow in a long channel, this divergence is surely zero. In an SAW-driven droplet, however, it is not. The impact of the SAW on suspended spherical particles will be treated in Section 3.3. In this section, we focus on boundary effects.

Boundary effect

In case that the drift velocity $\mathbf{d}(\mathbf{X})$ is a solenoidal vector field, the trivial particle distribution $\rho(\mathbf{X}) = \mathit{const}$ is a solution of the stationary Fokker-Planck equation – if the boundary conditions indeed allow this solution. The boundary condition for the particle density in the fluid is the condition of vanishing normal particle flux,

$$0 = \mathbf{N} \cdot (\rho \mathbf{d} - D \boldsymbol{\nabla} \rho) \,, \tag{3.44}$$

which guarantees that the total particle density is conserved.

Additionally, the velocity field obeys the kinematic boundary condition, namely $0 = \mathbf{N} \cdot \mathbf{v}^{(0)}$. Taking for the drift velocity (3.41) the velocity field $\mathbf{v}^{(0)}$, which is the leading-order term, one always finds the trivial solution $\rho(\mathbf{X}) = \mathit{const}$ to obey the no-flux boundary condition (3.44). Therefore, we may expect neither a volume nor a boundary effect to leading order.

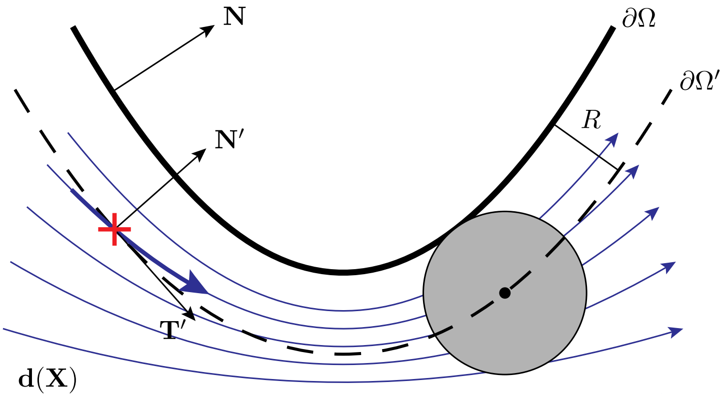

Figure 3.2. A spherical particle hits the boundary $\partial\Omega$ of the fluid domain, indicated by the thick solid curve. The region which is accessible for the particle centre is slightly smaller. Its boundary is marked by the dashed curve. The drift velocity field, which is indicated by the curved arrows, exhibits non-vanishing normal components at the boundary $\partial\Omega'$, for example at the point marked by a cross. This normal component leads to an accumulation or a depletion of particles near the boundary.

A close look on a spherical particle in the vicinity of a boundary reveals that the foregoing argumentation about the kinematic boundary condition is not fully applicable. Relevant in Faxén's theorem (3.29) is the velocity field at the centre of the particle. This centre, however, never touches the physical boundary but will always stay one radius apart from it. The no-flux boundary condition (3.44) must therefore be imposed on a slightly shifted boundary $\partial\Omega'$ rather than on the boundary $\partial\Omega$ of the fluid. Figure 3.2 sketches the situation. The effective boundary $\partial\Omega'$, depicted by the dashed curve, is defined to have always constant distance from the physical boundary $\partial\Omega$. The streamlines of the flow, and also the fieldlines of the particle drift velocity do not have a constant distance from the boundary. Thus, none of the fieldlines coincides with the effective boundary, and some of them must cross the boundary $\partial\Omega'$ of the region which is accessible to the particle centres. One of these crossing points is marked in Figure 3.2. The drift velocity there has a non-vanishing normal component, thus preventing the trivial particle density from satisfying the boundary condition (3.44). At the marked spot the normal component of $\mathbf{d}(\mathbf{X})$ is positive, which leads to a deposition of particles at the boundary. A negative normal component would describe a particle transport away from the boundary. Both signs will be found in the numerical simulations below. Since the boundaries have distance R, we expect the accumulation effect due to this *hard-sphere* collision with the boundary wall to scale linearly with the particle radius.

We cannot tell much about the normal projection of the next-order terms in (3.41). Generally, these terms may also give rise to a boundary effect. The magnitude of this effect, however, is small. It scales quadratically with the particle radius R and is therefore expected to be smaller than the hard-sphere boundary effect described above. Furthermore, for pressure-driven flows in long channels, a look on Figure 3.3d below reveals the pressure gradient at the boundary to be oriented in tangential rather than in normal direction.

3.2.1. Channels with no-slip boundaries

In the previous paragraphs, we found that in pressure-driven flows in long channels the volume effect of the particle accumulation cannot occur, if spherical particles are considered. We now analyse the boundary effects occurring in such systems. The discussion is restricted to the effect which we expect to be dominant for very small particles. This is the effect growing linearly with the particle radius, namely the collision effect depicted in Figure 3.2. For this effect it is sufficient to take the leading-order term in the drift velocity (3.41) and to use it in the stationary Fokker–Planck equation in the domain Ω' which is accessible to the particle centres,

$$0 = -\mathbf{v}^{(0)} \cdot \boldsymbol{\nabla}\rho + D\Delta\rho \,, \tag{3.45}$$

with the boundary condition on $\partial\Omega'$,

$$0 = \mathbf{N}' \cdot (\rho\, \mathbf{v}^{(0)} - D\boldsymbol{\nabla}\rho) \,. \tag{3.46}$$

The normal vector $\mathbf{N}'$ is the normal vector of the effective boundary $\partial\Omega'$.

Equations (3.45) and (3.46) are used to model the particle accumulation in the eight-shaped setup of Section 1.3.2, see Figure 1.5. The original setup comprises a three-dimensional water channel, bounded partly by a rigid flat substrate, partly by a curved free surface. We here employ a two-dimensional model flow, bounded by straight and curved no-slip and perfect-slip boundaries. The two-dimensional channel is periodically continued, thus modelling only the interesting middle part of the eight-shape, indicated by the circle in Figure 1.5.

The model flow is the solution of the stationary Stokes equations (1.4) and (1.6) together with the boundary conditions (1.9), (1.10), and (1.16). Since the SAWs that drive the flow are far away from the middle part of the eight-shape, the precise type of driving in the model flow does not matter. We employ a pressure gradient, which equivalently corresponds to a constant body force. Note that we do not solve the full free-surface problem here, and the surface geometry is not considered to be part of the problem. This allows to prescribe a curved slip-boundary, which makes the accumulation effects in the two-dimensional model flow more realistic. Since the channel is infinitely long and the flow is periodic, a truly free surface would equilibrate at a straight shape. As indicated in Section 1.3, we need some kind of asymmetry in the geometry of the channel in order to obtain a non-vanishing effect. This has been observed in the drift ratchet, and it can in our case be seen from Figure 3.2. The boundary accumulation effect in long channels takes place *only* if curved boundaries are involved.

Figure 3.3 shows the two-dimensional flows in differently shaped channels. Each channel is periodic in the direction of its axis. On one side it is bounded by a straight wall,

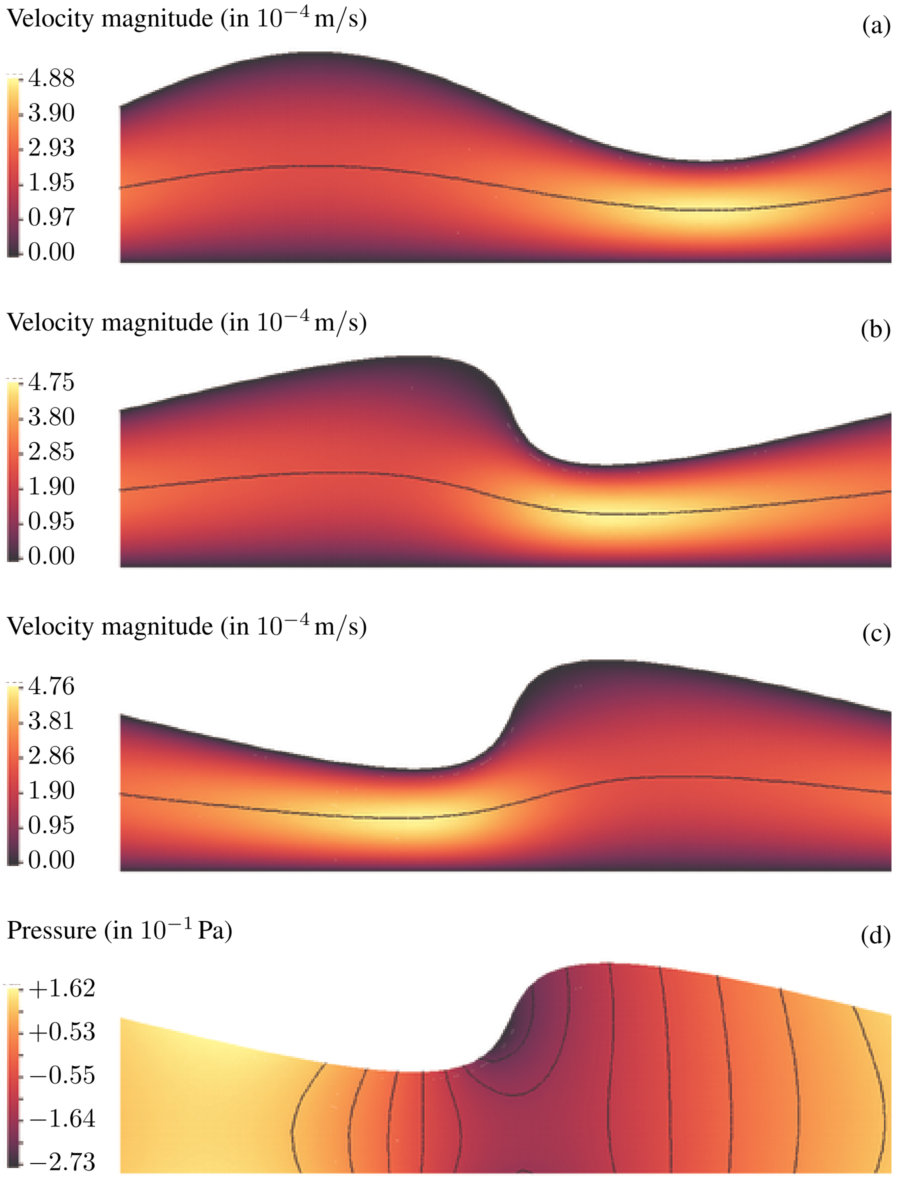

Figure 3.3. The flow in channels with no-slip boundary conditions. Each channel is periodically continued at its left and right boundaries, resulting in an infinitely long channel. Illustrated are three unit cells with different asymmetry parameters of the curved boundary. They are $a = 0$, 0.8, and -0.8 for (a), (b), and (c) in this order. The average flow direction is from left to right in all three panels. The flow is driven by a pressure difference of $\Delta p = 1\,\mathrm{Pa}$ along the length $L = 10^{-4}\,\mathrm{m}$ of a unit cell. The black lines in (a)–(c) indicate the streamlines which separate the two flow chambers of the microfluidic device of Figure 1.5. Here, they have been chosen in the middle of the flow, where the water throughputs above and below the separating streamline are equal. Panel (d) shows the pressure field, without the applied linear pressure gradient driving the flow. The black lines in (d) are level lines of the pressure. At the boundary, they tend to end in normal direction rather than in tangential direction.

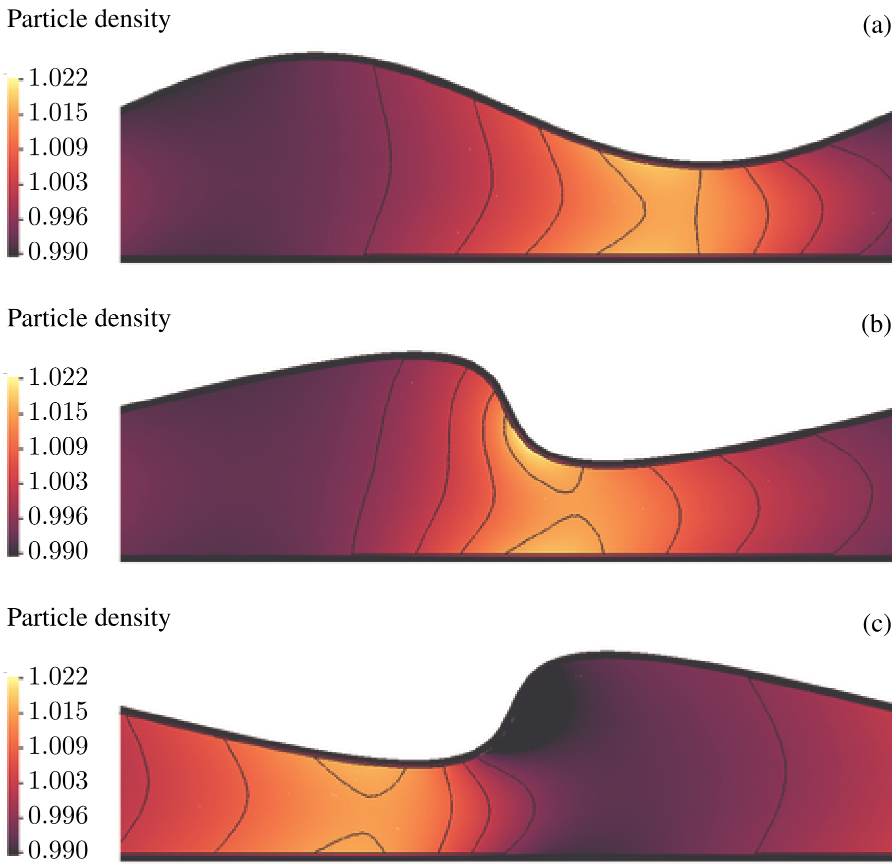

Figure 3.4. Typical densities of particle centres in the flows depicted in Figure 3.3. At the wall, the thin black zone with zero density indicates the area which the particle centres cannot enter. It is one particle radius wide, which here has been set to $R = 10^{-2}\,L$. The thin black lines are level lines of the particle density, which has been normalised to an average value of unity. For the considered average flow direction from left to right, we find that the region in front of the bottleneck is populated by more particles than the region behind. The densities have been calculated using a ratio of pressure difference and temperature $\Delta p/T = 3.3 \times 10^{-6}\,\mathrm{Pa/K}$ which corresponds to a Péclet number of $Pe \approx 16$.

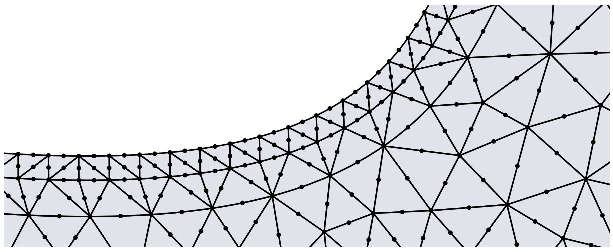

Figure 3.5. A detail of the computational mesh at the boundary. The outermost layer of finite elements represents the forbidden zone for the particle centres. The element sides of this layer constitute the two boundaries $\partial\Omega$ and $\partial\Omega'$, see also Figure 3.2.

while the other wall is curved. The flows have been calculated as the numerical solution of the Stokes equations with periodic boundary conditions relating the in- and outflow at the left and at the right sides of a unit cell. The Stokes equations and the boundary conditions have been implemented according to the algorithm in Chapter 2 and Appendix C. The curved upper boundaries of the channels are given by the function g, which is defined by the relation

$$g(z) = \sin\bigl(2\pi z - a\, g(z)\bigr)\ . \tag{3.47}$$

The parameter a causes the asymmetry of the shape. A value $a = 0$ corresponds to the symmetric sinusoidal shape in Figure 3.3a, while shapes with $a > 0$ close steeper than they broaden, when seen from left to right, compare Figure 3.3b. The function g can be evaluated iteratively, starting with $\sin(2\pi z)$. We found the iteration to converge for asymmetry parameters $a \in [-1, 1]$.

As mentioned above in Section 1.3, see Figure 1.4, the difference of the current setup to the drift ratchet is that here the flow is unidirectional. The asymmetry of the channel, having one straight and one curved boundary, may cause a particle accumulation *perpendicular* to the main flow direction. An individual trajectory of a particle essentially follows a streamline of the velocity $\mathbf{v}^{(0)}(\mathbf{X})$. Small deviations from the streamlines are caused by the random contributions. The particle *accumulation* that we refer to is a highly dynamic process. The conventional understanding of an accumulation is rather such that particles move towards a certain region and stay there. In contrast, in the current accumulation mechanism, different streamlines of the flow are populated differently by the particles, which remain in permanent motion. Only if the flow is stopped at some time, which can happen in such small systems almost without inertial relaxation, then the resulting particle distribution is similar to the usual understanding of an accumulation.

Figure 3.4 presents the numerically obtained solutions of the stationary Fokker–Planck equation (3.45) with boundary condition (3.46) for the flows in Figure 3.3 with no-slip boundaries. The global forms of the stationary distributions in Figure 3.4 are quite intuitive. Left of the bottleneck in the channel, we find an accumulation zone of the particles. Since the main flow direction is from left to right, the flow velocity concentrates particles just in front of the bottleneck. This result can be understood with a look on Figure 3.2. At the bottleneck, the density of streamlines is higher than in the wide part of the channel. Their form is governed by the Stokes equation, while the form of the effective boundary $\partial\Omega'$ is governed only by the geometry of the physical boundary. Thus, left and right of the bottleneck we find regions where many streamlines cross the effective boundary. There, the drift contains a non-vanishing component in normal direction, $\mathbf{N}'\cdot\mathbf{v}^{(0)} \neq 0$. A particle at such a point is transported only by the tangential component of $\mathbf{v}^{(0)}$, and is thus slowed down. The normal component is compensated by the wall. This normal component results in the dynamic accumulation that we see in Figure 3.4. Correspondingly, a depletion zone occurs behind the bottleneck.

The accumulation effect is caused by the fact that the particle centres cannot enter the region near the boundary of the fluid, as explained above and illustrated in Figure 3.2. We use particle radii which are at least two orders of magnitude smaller than the system size.

The computational mesh has to provide both boundaries, $\partial\Omega$ and $\partial\Omega'$. Figure 3.5 shows a detail of the mesh near a boundary, where the zone of thickness R, which the particle centres cannot enter, is given by one layer of finite elements. The boundary condition for the Stokes equation must be satisfied at the outer boundary, while the no-flux boundary condition (3.44) holds at the effective boundary consisting of finite-element boundaries of the second layer. The resulting forbidden zone for the particle centres can be identified in Figure 3.4 as the zone near the boundary, where the particle density is zero.

The parameter regime of equation (3.45) is characterised by the dimensionless *Péclet number*, which expresses the ratio of advective to diffusive transport. Since the flow in the channels is pressure-driven, the typical velocity scale is proportional to the applied pressure difference. We set the scale of the velocity to the maximal velocity in a Poiseuille flow in a straight channel of length L and width W,

$$\bar{v} = \frac{W^2\,\Delta p}{4\eta L}\,, \tag{3.48}$$

which reproduces the correct order of magnitude when the narrowest channel width $W \approx L/8$ is used, see Figure 3.3. The Péclet number then reads

$$\mathit{Pe} = \frac{\bar{x}\bar{v}}{D} = \frac{3\pi L^2}{128\,k_\mathrm{B}}\,R\,\frac{\Delta p}{T}\,. \tag{3.49}$$

For the stationary particle distribution, there is no difference between a weakly driven system and one at a high temperature, as long as the ratio $\Delta p/T$ is the same. In the numerical calculations for several different temperatures, we therefore used the same numerically obtained velocity field, driven by a unit pressure difference $\Delta p = 1\,\mathrm{Pa}$ along the channel length $L = 10^{-4}\,\mathrm{m}$. The Péclet number used in Figure 3.4 is $\mathit{Pe} \approx 16$. This corresponds to a slightly advection-dominated transport of particles. For smaller Péclet numbers, the diffusion becomes dominant, resulting in a smoother particle distribution than in Figure 3.4. For larger Péclet numbers, the maxima of the distribution near the boundaries become more pronounced.

The temperature values used in the following numerical calculations (from $10^5\,\mathrm{K}$ to $3\times10^8\,\mathrm{K}$ at the pressure difference $\Delta p = 1\,\mathrm{Pa}$) correspond to pressure differences between $10^{-6}\,\mathrm{Pa}$ and $3\times10^{-3}\,\mathrm{Pa}$ at room temperature. Together with the particle radius R ranging from $10^{-3}L$ to $10^{-2}L$, we obtain Péclet numbers in the range

$$\mathit{Pe} \in (10^{-1}, 10^2)\,. \tag{3.50}$$

Hence, the parameter regime covers all parameters from diffusion-dominated to advection-dominated flows.

The behaviour of the stationary particle distributions in the direction perpendicular to the main flow direction is not obvious and cannot be guessed from a glance at Figure 3.4. In the figure, we find accumulation and depletion regions on both sides of the separating streamline. We would like to know in which basin of the eight-shaped flow chamber

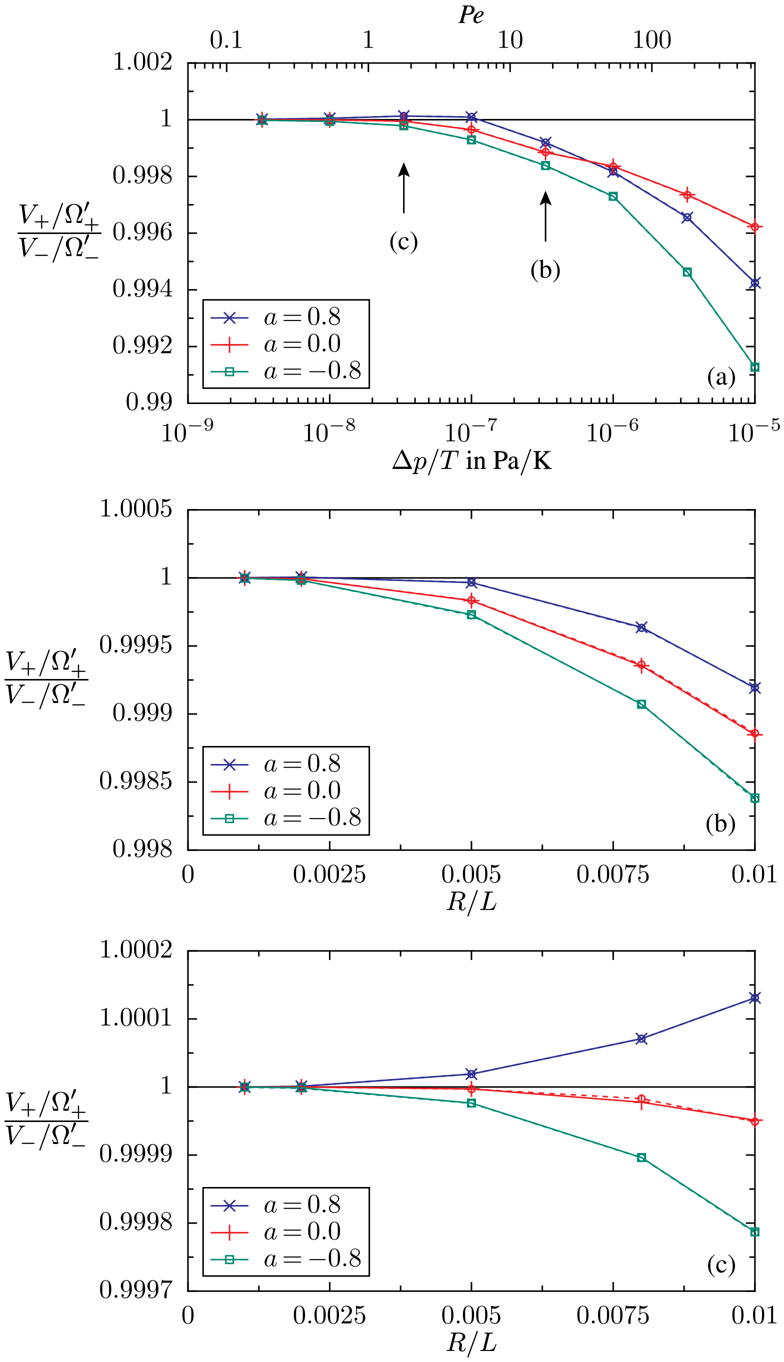

Figure 3.6. The relative accumulation effect for the flows in Figure 3.3 with no-slip boundary conditions. Values smaller than unity correspond to the situation where more particles are in the basin below the separating streamline, near the straight boundary. Panel (a) exhibits that this occurs for most flow parameters. Only the boundary shape in Figure 3.3b with asymmetry parameter $a = 0.8$ allows an accumulation at the curved boundary as well as at the straight one. In panel (a) the temperature is varied for a fixed particle radius of $R = 10^{-2}L$. In panels (b) and (c) the particle radius is varied for two selected temperatures $\Delta p/T = 3.3 \times 10^{-7}$ and 3.3×10^{-8}. The interesting behaviour of the curve for $a = 0.8$ in panel (a), yielding values larger than unity, persists also for all radii in panel (c). In all three panels, the numerical results have been calculated also for the inverted flow with inverted pressure differences. The resulting values are found to be identical to the original values. They are depicted by small circles, connected by dashed lines.

of Figure 1.5 there are more particles of a specified radius. To find an answer to this question, we integrate the particle density in the two regions Ω'_+ and Ω'_-, representing the accessible regions above and below the separating streamline. The two probabilities

$$V_+ = \int\limits_{\Omega'_+} \rho \, dV \quad \text{and} \quad V_- = \int\limits_{\Omega'_-} \rho \, dV \qquad (3.51\,\text{a,b})$$

of finding a particle above $(+)$ or below $(-)$ the separating streamline can be used to provide a measure for the relative accumulation of particles in one of the basins. Of course, the position of the separating streamline has to be taken into account as well. We use the quantity

$$\frac{V_+}{\Omega'_+} \Big/ \frac{V_-}{\Omega'_-} \qquad (3.52)$$

as a measure for the relative accumulation in the upper basin, which is the one with the curved boundary. The denominators Ω'_+ and Ω'_- stand for the volumes of the regions above and below the separating streamline.

Figure 3.6 displays the resulting relative accumulation for the flows in Figure 3.3 with two no-slip boundaries. The upper panel gives the ratio (3.52) as a function of the inverse temperature. The first observation is that the effect vanishes for vanishing driving – or equivalently, for infinite temperature. For most parameters, the result is smaller than unity. This corresponds to an *accumulation of particles on the side of the straight wall*. This appears as a general tendency, which was found also for different shapes and different boundary conditions, see the results below in Section 3.2.2. The relative accumulation effect is small, up to maximally one percent for the smallest temperature we have used in the calculation. As expected, it vanishes for very small values of $\Delta p/T$. In order to convince ourselves that this small effect is not an artefact of the numerical calculation, also the flows in the inverted channels with inverted pressure differences have been used. The results are also depicted in Figure 3.6. The differences are found to be smaller than the linewidth.

For two temperature values, also the particle radius has been varied. Panels (b) and (c) of Figure 3.6 depict the ratio (3.52) as a function of the radius. Again, the effect vanishes with vanishing radius. This is the expected behaviour, because a point-particle can come arbitrarily close to the physical boundary.

An interesting aspect of the accumulation results in Figure 3.6 is the fact that the two doubly asymmetric channels (with $a = 0.8$ and $a = -0.8$) behave differently. It seems to be the general tendency that the channel which suddenly widens and slowly narrows ($a = -0.8$) yields better accumulations than the suddenly narrowing one. The channel with the sinusoidal shape ($a = 0$) yields accumulation results somewhere in between.

A remarkable property of the accumulation mechanism can be observed at the flow in the shape with asymmetry parameter $a = 0.8$, where the flow from left to right experiences a slowly opening channel which suddenly narrows. Here, we find values of the ratio (3.52)

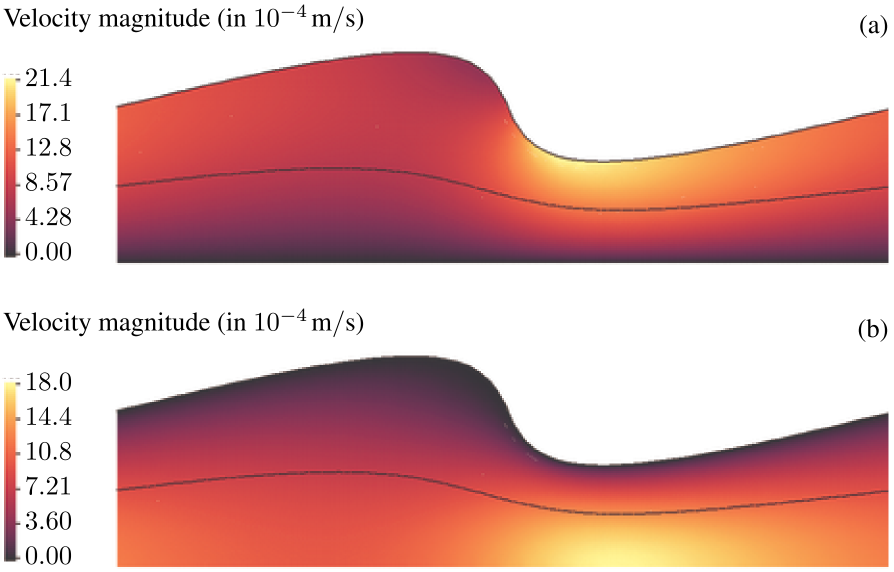

Figure 3.7. The flow in partially open channels. In (a) we have used the perfect-slip boundary condition at the curved boundary together with a no-slip condition at the straight one. In (b) the boundary conditions are interchanged. The velocity magnitude is maximal at the slip boundary, as expected for free-surface flows.

not only smaller than unity, but also larger than unity. Particles in this parameter regime are transported rather towards the curved boundary than towards the straight one. The occurrence of both values corresponds to an inversion of the transport direction. Panel (c) confirms that the values larger than unity, which we found in panel (a), persist also for several smaller radii. Note that for each radius, a different numerical mesh had to be used, displaying the correct boundary $\partial\Omega'$. An *inversion* of the accumulation direction is exactly what is needed for sorting particles, similar to the current inversion in the drift ratchet (Kettner et al., 2000). However, the inversion found here is not readily usable for sorting particles, because the inversion takes place only while varying the parameter $\Delta p/T$ and not the radius R. Moreover, the effect is far too small to be of experimental relevance. Still, the occurrence of accumulation inversion is an interesting effect.

3.2.2. Comparison of slip and no-slip boundaries

In the previous section, we found that the eight-shaped microfluidic device in Figure 1.5 indeed accumulates particles in one of its loops. The calculations have been performed for a model flow with no-slip boundary conditions. We now consider free-surface flows as well. In the above paragraphs, we found that the accumulation effect strongly depends on the shapes of the boundaries. By construction of the boundary effect, it is also clear that the accumulation must vanish if two parallel straight boundaries are used.

Curved boundaries in the tree-dimensional flows within the eight-shaped geometry of Figure 1.5 can be enforced by prescribing suitable wetting patterns on the underlying sub-

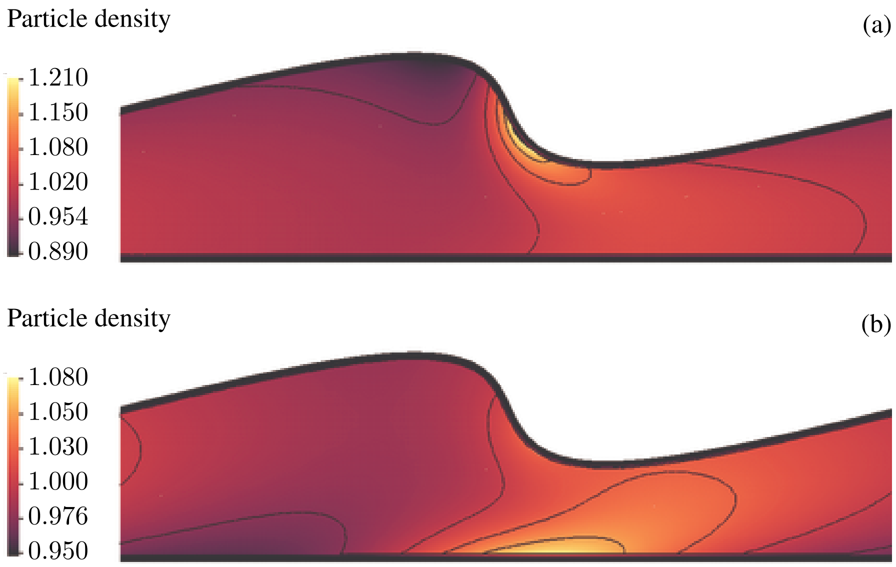

Figure 3.8. Particle distributions in the flows of Figure 3.7. The particle radius and the temperature are the same as in Figure 3.4. The maximum and minimum of the distribution are more pronounced than in Figure 3.4. This is an immediate result of the perfect-slip boundary conditions, used here instead of the no-slip boundary conditions as used in Figure 3.4. The large velocities at the boundary also contain larger normal components, which cause more pronounced maxima and minima of the particle distribution. The curved slip-boundary in panel (a) is even more effective in causing an inhomogeneous distribution than the straight one in panel (b). This can be understood in terms of Figure 3.2: The whole accumulation effect is caused by the streamlines crossing the boundary $\partial\Omega'$. At curved surface, there seem to be more such crossings.

strate. Curved boundaries of the wetting patterns generally give rise to likewise curved free boundaries. We would like to model such a flow with our two-dimensional setup and therefore maintain a prescribed curved boundary also for the model of the free surface. As mentioned in the previous section, a truly free surface would be straight due to our special situation of a periodically continued channel.

The flows resulting from the same pressure difference and for the same boundary shape as in Figure 3.3 but with different boundary conditions are depicted in Figure 3.7. The flow in panel (a) is subject to a no-slip boundary condition at the straight wall and to a perfect-slip condition at the curved boundary. These boundary conditions are interchanged in panel (b). As in the flows with truly free surfaces in Chapter 2, Figures 2.12 and 2.13, the maximal velocity is found at the surface.

The use of free surfaces instead of closed geometries with rigid walls gives rise to larger accumulation effects: Since the velocities at the boundaries are generally much higher at free surfaces than at no-slip walls, and since the accumulation in this section is due to a boundary effect, also the normal components of the velocity that enter the boundary condition (3.46) cause larger effects. In this sense, the accumulation at a free surface can make use of the maximal velocity that is obtainable in the system. How much larger the effects are, can be revealed from Figure 3.8. Compare the maximum values of the

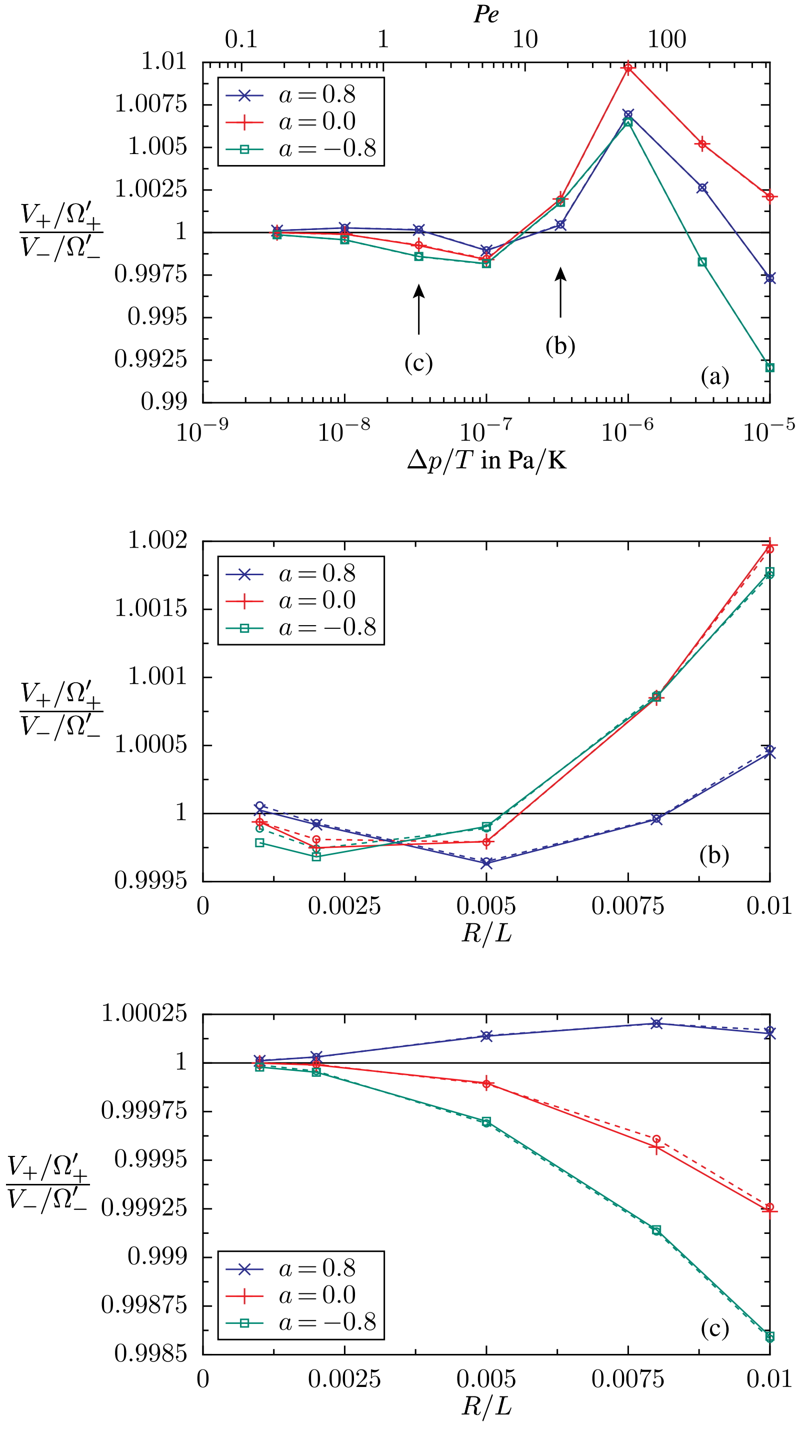

Figure 3.9. The relative accumulation effect for flows with a curved no-slip boundary and a straight slip boundary, see Figures 3.7b and 3.8b. The magnitude of the accumulation effect is similar as in Figure 3.6. The accumulation direction, however, exhibits drastic changes. In panel (a) the particle radius is fixed to the value $R = 10^{-2}\,L$ and only the temperature is varied. Panels (b) and (c) show the particle accumulation as a function of the radius of the particles, for two fixed ratios of pressure difference and temperature $\Delta p/T = 3.3 \times 10^{-7}$ and 3.3×10^{-8}, respectively. The sign of the accumulation direction changes not only as a function of the driving in panel (a), but also as a function of the radius in panel (b).

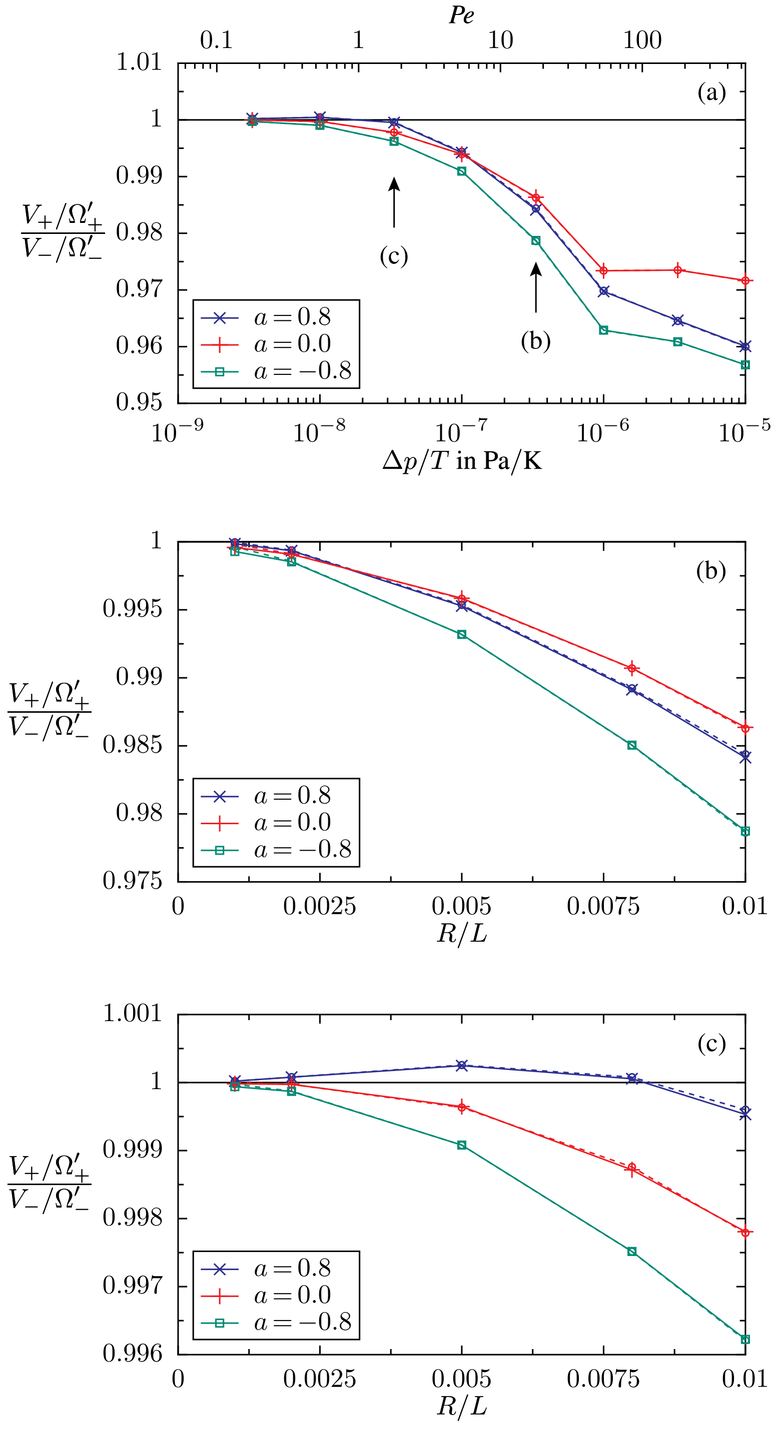

Figure 3.10. The relative accumulation effect flows where the curved boundary carries a perfect-slip boundary condition, while the straight one is sticky, see Figures 3.7a and 3.8a. The magnitude of the accumulation effect is larger than in Figures 3.6 and 3.9. Again, the particle radius is $R = 10^{-2} L$, with variable temperature in panel (a). In panels (b) and (c) the pressure difference and temperature are $\Delta p/T = 3.3 \times 10^{-7}$ and 3.3×10^{-8}, respectively, and the radius is varied.

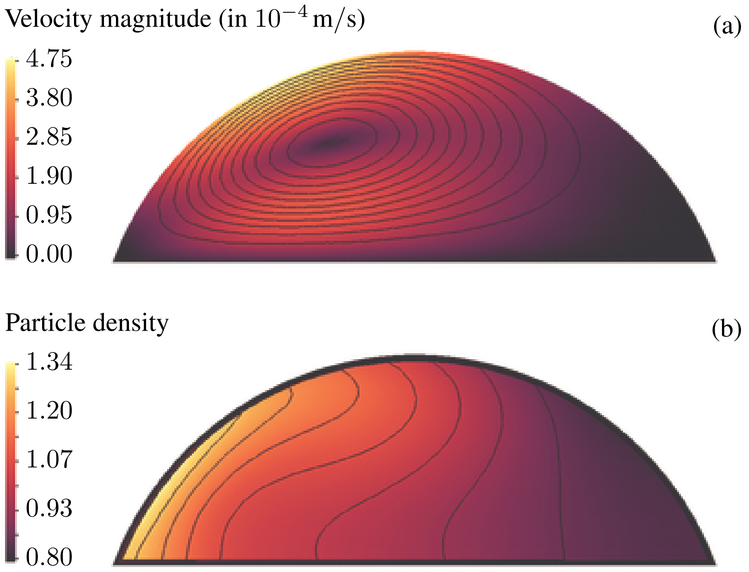

Figure 3.11. The accumulation in a droplet. The boundary comprises a no-slip condition at the flat substrate and a perfect-slip boundary condition at the curved free surface. The typical velocity scale and the temperature are the same as in the channels of Figure 3.4. The two contact-points on the horizontal axis are 10^{-4} m apart. Hence, the Péclet number is $Pe \approx 16$, the same value as for the channels in Figure 3.4.

particle densities with that of Figure 3.4b. The maxima and minima here are five to ten times more pronounced.

Larger accumulation effects than in their no-slip equivalent can also be seen in Figures 3.9 and 3.10. In these two figures, the accumulation of particles below the separating streamline, relative to the particles above the separating streamline, is shown for the same parameters as in Figure 3.6. Again, the accumulation depends on the asymmetry parameter a. In contrast to Figure 3.6, where the sinusoidal shape with $a = 0$ mostly yields values between the other two shapes, we here find a more complicated dependence on a. In panel 3.9a, the line with $a = 0$ lies above the other two for larger values of $\Delta p/T$ and between them for smaller values. In panel 3.9b there seems to be no difference between the shapes with $a = 0$ and $a = -0.8$. This complicated dependence of the accumulation on the shape parameter a makes a simple explanation of the effect impossible. As in Figure 3.6, the numerical findings have been checked by inverting both the channel geometry and the flow direction, proving that the numerical error is negligible compared to the accumulation effect.

Figures 3.9a and 3.10a exhibit a similar accumulation inversion as has been found in Figure 3.6a, where only no-slip boundaries were used. There, we did not find an inversion while varying the radius of the particle. Here, in Figures 3.9b and 3.10c, and probably also in 3.9c, an accumulation inversion takes place also when the radius is varied. This is an immediate result of the employment of slip boundaries instead of no-slip ones.

The fact that the accumulation is much larger at a free surface than at no-slip walls can be understood more readily for a confined geometry than for the infinitely long channels. Consider a droplet, driven by similar forces as the droplets in Figures 2.12 and 2.13 in Chapter 2. Here, we are only interested in the flow and thus solve the Stokes equations in a given circular shape, as depicted in Figure 3.11. Note that the streamlines in panel 3.11a behave differently at the curved free surface and at the wall. The distance between adjacent streamlines is larger in the vicinity of the rigid substrate than far from it. Near the free surface, this distance remains the same. That the distances between adjacent streamlines behave differently in the two cases is a geometric way of saying that the boundary conditions are different. As a result, the centre of rotation resides nearer to the free surface than to the substrate, with the implication that the streamlines are more dense at the free surface. Consequently, at this surface, there are more streamlines crossing the effective boundary $\partial\Omega'$ at a higher velocity, compared to the no-slip substrate. This geometric picture explains the accumulation pattern in panel 3.11b, which exhibits an accumulation predominantly at the free surface and not at the substrate. The region where the free surface can accumulate particles is in the upper left part of the boundary. The region of a possible accumulation by the substrate is at its lower right part.

Note that for Figure 3.11 the argumentation with a forbidden zone of width R has been equally used for the rigid wall and for the free surface. Strictly speaking, the free surface could behave differently in this respect, allowing an effective width smaller than R, if the particles were allowed to leave the fluid partly, or to deform the surface locally. The currently used width R can be assumed for particles that try not to leave the fluid, namely strongly wetting particles.

3.3. Particle accumulation in SAW-driven eddies

After having analysed the boundary accumulation effects in the previous section, we now turn to a volume accumulation in the eight-shaped channel geometry. A volume effect can occur only in the vicinity of the point where the SAW enters the fluid, because this is the only region where sensible body forces are found. We thus focus on the two corners of the eight-shape of Figure 1.5, where the SAWs are located. In each of these corners, the main flow along the channel is generated. Additionally, as the body force is quite strong there, the flow exhibits two eddies (Frommelt and Wixforth, 2006). Rotating in such an eddy appears to be preferable to the fluid compared to the long route around a loop. The flow pattern in such a corner is visualised in Figures 3.12 and 3.13.

The main conclusion of Chapter 2 concerning particle transport is that there must be a dominant pressure field active in the region where the SAW enters the fluid. For the observed velocities, we found that only a strong pressure contribution is able to deform the free surface substantially. The gradient of this pressure acts as a force on a particle, according to equation (3.5). We remind that this is a zero-order force, thus independent of the correction flows caused by the particle itself. The magnitude of the pressure force depends on the properties of the fluid, on the driving by the SAW, and on the particle radius. In Chapter 2, we found the pressure forces to be much larger than the viscous forces at the free surface. The body force caused by the SAW must be dominated by the conservative contribution. This has some consequences for the terms adding up to the drift velocity $\mathbf{d}(\mathbf{X})$ in equation (3.41). When comparing the two terms proportional to R^2, the Laplacian of the velocity is found to be negligible, only the pressure gradient remains. Furthermore, the terms proportional to R^4 and higher-order terms vanish since the particle is smaller than the typical length on which the pressure changes. As a result, only the first term in equation (3.41), namely the velocity of the unperturbed flow, and the third one, the unperturbed pressure gradient remain as relevant in the drift velocity of the particle.

As we found in Chapter 2 that the pressure gradients can be quite large in SAW-driven systems, we put forward the hypothesis that the pressure field plays an important role in the accumulation process of particles. For estimating the relative importance of the two remaining forces on the particle, we take the pressure inside of the droplet of Figure 2.12. The bar-like form of the region where the pressure is large, can be seen directly in Figure 2.12b. It acts as a barrier for particles trying to follow the streamlines of the flow. We therefore consider a particle trajectory at the highest available velocity, which tries to cross this barrier in perpendicular direction and which is stopped by the pressure forces at some point. The condition for the viscous drag forces and the pressure gradient to compensate each other at this point is

$$6\pi\eta R\mathbf{v}^{(0)}(\mathbf{X}) = \frac{4\pi}{3}R^3\boldsymbol{\nabla}p^{(0)}(\mathbf{X})\,. \tag{3.53}$$

When the magnitudes of velocity and pressure are taken from Figure 2.12, then a critical radius is obtained as

$$R_{\text{crit}} = \sqrt{\frac{9\eta\,\|\mathbf{v}^{(0)}\|}{2\,\|\boldsymbol{\nabla}p^{(0)}\|}} \approx 0.5\,\mu\text{m}\,. \tag{3.54}$$

Particles with a smaller radius than R_{crit} have a better chance to pass the barrier together with the fluid, while larger particles are exposed to a larger pressure difference and are kept back. We emphasise that the pressure does not influence the carrier flow at all. The ratio of the viscous drag and the pressure force depends quadratically on the radius of the particle. For a sphere with $5\,\mu$m radius, this ratio is already 10^{-2}. The viscous drag on such a particle may thus be neglected in the vicinity of the pressure barrier.

The effect by the pressure fields from the SAW might be an explanation for an interesting phenomenon in the experiment (Frommelt and Wixforth, 2006). When particles are immersed in the water of the eight-shaped channel, then, under certain circumstances, they are found to be collected in one of the flow eddies after some time. Figure 3.12 depicts such an accumulation of micro-beads of 4.6μm radius, which were well distributed before the flow has set in. While the particles perform their motion according to the viscous drag and to the pressure forces, they are found to be absorbed into one of these eddies, leaving the remaining fluid empty. The experimental photographs in Figure 3.12 illustrate this process. It is the upstream eddy, sitting in front of the pressure barrier, which collects the vast majority of particles. This leads to the proposed hypothesis that

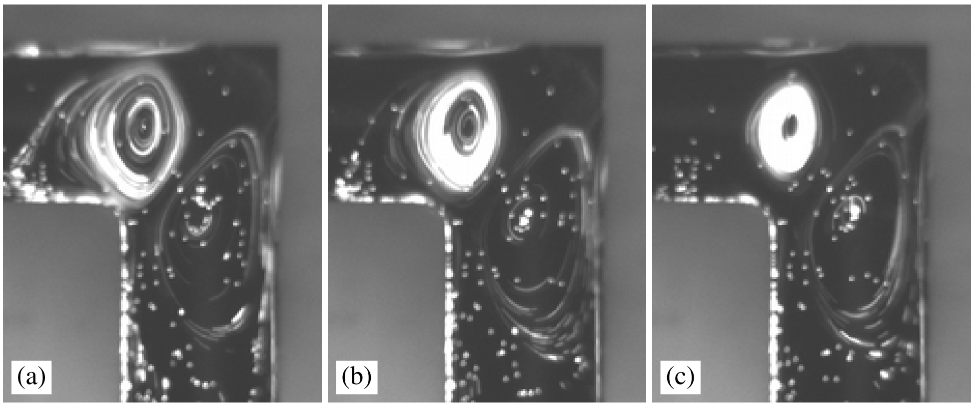

Figure 3.12. The particle collection mechanism in two eddies generated by a SAW: The photographs show one of the bended corners of the eight-shaped water channel of Figure 1.5. The main water flow is from the left to the bottom side of the photographs. The SAW runs into the bend from the top. The SAW causes not only the main flow but also the two eddies, a round one in front of the bend and a lengthy one behind. Immersed in the flow are beads of $4.6\,\mu$m radius. Initially, the particles are well distributed in the fluid. Soon, they are dragged into the round eddy in front of the bend. In photograph (a) the two eddies can be recognised in an intermediate state, when the particles are still distributed a bit. Photograph (b) shows a later state, where nearly all particles are collected in the eddy, and (c) shows the final state. (Pictures from T. Frommelt)

the SAW acts as a pressure cap for the upstream eddy. When a particle is about to leave this eddy in order to follow the main flow along the loop of the eight-shape, then it must pass the region with high pressure. That the pressure barrier is located exactly where the particles try to leave the eddy is an presumption on the form of the driving force caused by the SAW. It appears plausible since both the non-conservative part, which generates the flow, and the conservative part, which is responsible for the pressure cap, have the same origin. For a validation of this assumption, however, both the details of the acoustic streaming mechanism and of the resulting three-dimensional flow would be required, which are inaccessible at the moment.

The fact that still some of the particles can be found in the downstream eddy indicates that not only the pressure-driven accumulation process is active here. The flow eddies themselves are somehow able to collect particles in their centre. This appears to be a much smaller effect than the pressure barrier by the SAW, it nevertheless helps the latter to collect the particles which cannot pass the barrier into the centre of the upstream eddy.

Figure 3.13 shows the same flow pattern for much smaller particles. Micro-beads of $0.36\,\mu$m radius have been used here, which is comparable to the critical radius R_{crit}. The viscous drag and the pressure forces are of the same order of magnitude, and the pressure field can only act as a very weak barrier. This is corroborated by the experiment. Generally, it appears to be much more difficult to obtain an accumulation of these smaller particles, requiring much stronger driving. Additionally, the accumulation is not reliable any more, depending not only on the existence of the eddy but on details of its shape and the precise position of the boundaries and the SAW. Figure 3.13 shows two situations

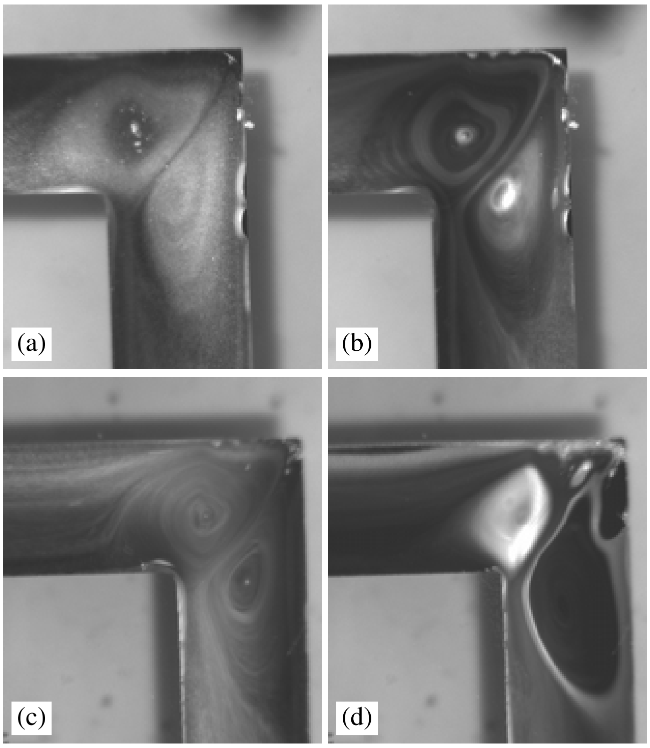

Figure 3.13. The particle collection mechanism, similar to Figure 3.12. The beads have a radius of $0.36\,\mu$m, which is comparable to the critical radius from equation (3.54). These smaller particles cannot be accumulated into one eddy as easily as the larger ones in Figure 3.12. In panel (b), which has been started with the situation in (a), no clear accumulation takes place. The flow of panel (c), however, leads to the accumulation in (d). Both situations required a much stronger driving than for the large particles and took more time. The driving had to be so strong that the water channel became unstable. (Pictures from T. Frommelt)

with very similar flow patterns, one of which does not cause an accumulation (panels a and b), while the other one does (c and d). Experiments with particles much smaller than the critical radius have not yet been done.

A numerical corroboration of our hypothesis that the pressure field by the SAW acts as a cap on the upstream eddy cannot be performed at the moment. The analysis of the droplet deformations in Figures 2.12 and 2.13 was sufficient to provide the correct order of magnitude for the drag and for the pressure forces on the particles. For the eddies in Figures 3.12 and 3.13, however, the topology of the flow pattern plays a key role. The nature of the driving by an SAW is not yet understood well enough to predict the precise shape of the conservative part of the body force which causes the pressure barrier. The three-dimensional flow pattern around this barrier is driven by the non-conservative counterpart, as detailed in Section 1.1.1. Thus, the relative position of the two force components and their relative orientation together determine the particle accumulation qualities of the SAW.

3.4. Summary

We have considered the transport of small particles in different types of flows. Two different kinds of boundaries are taken into account, namely sticky immobile walls, imposing no-slip boundary conditions on the flow, and free surfaces, which are modelled by perfectly slippery curved boundaries. Two different types of driving have been used, namely simple pressure-driven flows in long channels, and SAW-driven flows in droplets and water channels bounded by free surfaces.

A small particle, when immersed in a flowing fluid, is subject to quite a number of different forces, which all are weak. The detailed analysis of the different forces, as provided in Section 3.1, makes clear that an accumulation of particles in a flow may be caused either by a boundary effect or a volume effect. This accumulation of particles, which is a highly dynamical effect by populating different streamlines in a flow differently, can be described by the stationary Fokker–Planck equation (3.45) with the drift velocity (3.41). Depending on the shape and the size of the particle, different terms in the equation for the drift velocity are dominant.

We found that in the situation of a pressure-driven flow in a long channel, the drift velocity of a particle is essentially given by the velocity of the fluid. In this case, the flow in the channel cannot give rise to any accumulation effect. All effects must come from the channel boundaries. The further investigation of the boundary effect in Section 3.2 revealed that the boundary condition of the flow at the channel wall has a great influence on the accumulation pattern. We used channels which are curved at one side and straight at the other. As a general tendency, we found an accumulation of particles near the straight boundary than near the curved one, independent of the flow direction and the particle size. Only for specially shaped curved boundaries we found an accumulation inversion, leading to a higher concentration of particles near the curved boundary. When utilising free surfaces instead of no-slip walls, we found the accumulation effects to be larger, which is a direct consequence of the higher velocities at free surfaces, compared to walls. Also the accumulation inversion occurred for various shapes and for different particle radii. This result shows that an effect similar to the particle separation in the drift ratchet, which has been introduced in Section 1.3.1, is in principle possible also in systems with free surfaces, such as the one in Figure 1.5. As we assumed the flow to be stationary, not oscillating like in the drift ratchet, we found a particle transport in perpendicular direction of the main flow direction.

In SAW-driven flows, a volume accumulation effects can be found in the vicinity of the SAW. According to the formula for the drift velocity (3.41), the particles are transported by means of viscous drag and by means of the pressure gradients. Estimating the magnitude of these respective forces is possible with the aid of the pressure and flow fields we have obtained from the droplets in Chapter 2. As a result, there must be a critical radius of particles, where both forces are balanced. Larger particles get accumulated in a flow eddy in front of the SAW, while smaller particles tend to remain distributed.

4. Summary and outlook

The present thesis deals with microfluidic flows, where we usually have in mind small droplets or water channels, bounded partly by free surfaces, partly by a flat substrate. The fluid in these geometries is water, actuated by surface-acoustic waves (SAWs) by means of the acoustic streaming effect. We provide a stable and accurate numerical algorithm for the calculation of the resulting stationary flows with deformed free surfaces in the parameter regime of microfluidics, that is here characterised by a small Reynolds number together with Bond and capillary numbers up to unity. The consistent derivation of this algorithm with the aid of the calculus of variations is provided in Chapter 2: We propose to split the combined problem of finding the correct shape of the fluid domain, especially the free surface, and of finding the flow inside this domain, into two separate steps. The steps are processed successively, until the free surface has reached its target position.

Concerning the variational derivation of the Stokes equations together with the stress balance at the free surface in Section 2.2, we found that this variational description cannot be given in a fully consistent way. Despite the fact that the Stokes equations, describing a slow stationary viscous flow, can be obtained from a minimisation of a functional, and despite that also the behaviour of the free surface in a static setting can be obtained from a minimisation of a free energy, both approaches cannot be combined to yield a single functional for the full free-surface problem. This astonishing result is due to the different origins of the contributing forces. The tension forces are of thermodynamic (or rather thermo-"static") nature, while the viscous stress stems from dynamic considerations.

So far, the presented algorithm is restricted to two-dimensional free-surface flows with pinned contact-lines. Extensions to free surfaces with contact lines that are not pinned, that move, or that even lead to a breakup of the surface, appear to be possible. Still, there are some hurdles to be overcome, some of which can already be identified here. The presented covariant derivation of the forces at the free surface allows to clearly identify the occurring complications. One of them concerns the above mentioned different origins of the contributing forces, being of static or dynamic origin. The same problem arises when non-pinned contact lines are considered, which adjust their position according to thermodynamic and dynamic principles. Beside other complications, also the description of moving contact lines (see Thiele, 2003; Huh and Scriven, 1971; de Gennes, 1985; Dimitrakopoulos and Hidgon, 1999; Solonnikov, 1995; Leger and Joanny, 1992) as well as the treatment of pinch-off and breakup phenomena of free surfaces (Eggers, 1997; Notz et al., 2001; Cohen et al., 1999; Brenner and Gueyffier, 1999) encounters this fundamental problem. In our derivation, the different origins of the forces at the free surface became manifest in the principally unknown mutual dependence of the stress tensor and the surface parametrisation, when we had to introduce the approximation (2.63). Another indication on fundamental problems of the continuous variational description of free surfaces is our numerical observation of instabilities caused by the last integral in the second variation of the surface's free energy, see the comments on equation (2.89).

The presented covariant formulation of the forces at the free surface further opens the possibility to utilise the powerful differential geometric description of free surfaces in finite-element implementations of the Stokes equations. It thus provides a natural approach to treat surfaces and interfaces with a richer behaviour such as lipid vesicles containing bending stiffness, area constraints, and much more. Many potential applications can be found in the literature on lipid vesicle geometry, where more complicated expressions for the surface free energy contribution are in use (Guven, 2004; Capovilla et al., 2003; Seifert, 1997).

The free-surface flows in this thesis were driven by a bulk force that effectively modelled the influence of a SAW. The acoustic streaming effect, which takes place on two different time scales, still contains several aspects that are to be investigated further. To be mentioned is the large Reynolds number of the flow in the vicinity of the surface of the substrate, which causes problems in the theoretical description, see Section 1.2.

The second focus of the present thesis resides on particle transport in free-surface flows. The setup considered here is similar to the drift ratchet, which employs a driving periodic in time, see Section 1.3. We found that also in a stationary flow a particle transport can be achieved which is based on the finite extension of the immersed particles, on thermal fluctuations, and on the asymmetric shape of the boundaries of the flow. This effect can be considered a boundary effect, since it is caused by the boundary condition of the stationary Fokker–Planck equation which describes the long-time behaviour of the particle distribution. The boundary effect is based on the fact that the centre of a particle cannot come arbitrarily close to the boundary of the flow. In this situation, a small contribution of the force on the particle normal to the boundary either keeps the particle near the boundary, or pulls it away.

Concerning the boundary accumulation effect of the flows, we employed a description that modelled the interaction of a particle and a boundary as the collision of a hard sphere with a wall. A more detailed investigation would require also the influence of the particle shape on the drag forces. Taking the complete hydrodynamic interaction with other particles and with different types of boundaries into account would then be a next step. In our model, we found a strong dependence of the accumulation effect on the type of boundary, whether it imposes no-slip or perfect-slip boundary conditions on the flow. Also the hydrodynamic interactions between a boundary and a particle surely depends on the type of boundary condition. A comparison of the results from our model with those of a more detailed description, would provide insight into the influence of the boundary conditions. Another possible extension of our model concerns flexible particles.

A second accumulation effect has been observed in the volume close to the point where the SAW enters the fluid. Here, several interesting phenomena take place. One of them is that the fluid and the immersed particles are transported differently by the body force caused by the SAW. This body force is the stationary impact of the SAW on the fluid. Whether there are more direct forces by the SAW on an immersed particle, such as by the generated sound wave, or whether there is an influence of a suspension of particles on the acoustic streaming effect, are open problems. The calculations of chapter 2 allow the conclusion that the body force that is caused by the SAW must comprise a strong conservative contribution. This part of the force gives rise to a pressure field, which then imposes a force on extended particles, but does not act on the fluid. As a result, particles and fluid experience different forces, leading to an accumulation of particles in an eddy on the upstream side of the SAW. How efficient this accumulation is, depends on the size of the particles. Large particles are densely concentrated, while small particles remain distributed.

This last calculation nicely combines the results of both aspects in the SAW-driven microflows, which have considered in the present thesis. The geometry of deformed microdroplets in Chapter 2 helped to understand the role of the conservative and the nonconservative parts in the driving force, which proved useful for the accumulation effects in Chapter 3.

Appendix A.

Free-surface flow in a half cylinder: an analytical solution

In order to show how intricate the calculation of free-surface flows can become, we present a simple example. A water strand in the form of an infinitely long half cylinder is driven by a homogeneous body force parallel to the cylinder axis $\mathbf{e}_z$. Figure A.1 illustrates the situation. The contact surface with the substrate poses a no-slip boundary condition for the flow. The cylinder barrel is a fluid–air interface in the limit of infinite surface tension, thus presenting a perfect-slip boundary condition (1.16) for the flow. Due to the symmetry of the setup, we assume that the velocity is stationary and contains a non-vanishing component v_z only in z-direction. The incompressibility condition then requires that v_z does not depend on z. A transformation to polar cylindrical coordinates

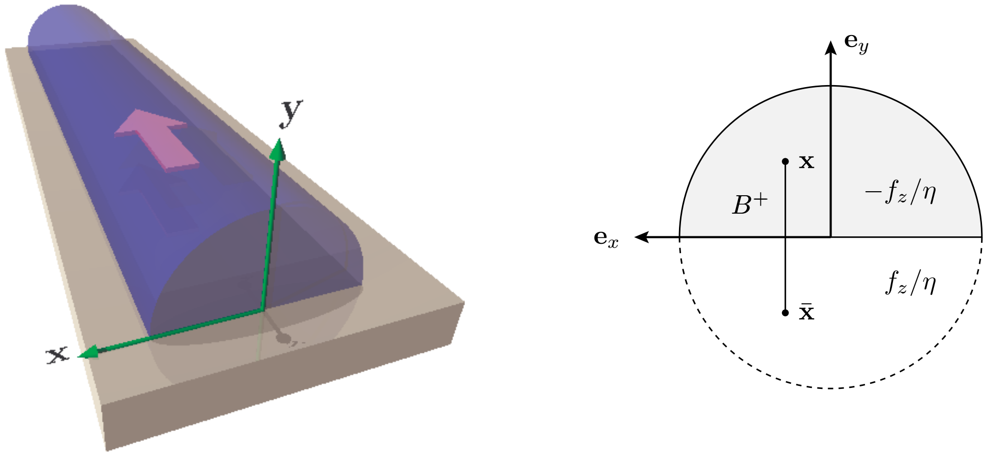

Figure A.1. Left panel: The geometry of a half-cylinder flow. The velocity at the substrate is zero, while the curved boundary is a free surface. The channel is assumed to have the same radius everywhere and to be infinitely long. Right panel: The grey shaded area indicates a cut through the fluid domain. Its completion to the full circle indicates the area where the Green function for the Poisson equation with Neumann boundary conditions is defined. The driving in the grey-shaded area is $-f_z/\eta$, while it has opposite sign in the white half circle. Thus, the velocity at $y = 0$ vanishes.

(r, φ, z) yields the stationary Navier–Stokes equation as

$$0 = -\partial_r p(r, \varphi, z) \,, \tag{A.1}$$

$$0 = -\frac{1}{r}\,\partial_\varphi p(r, \varphi, z) \,, \tag{A.2}$$

$$0 = -\partial_z p(r, \varphi, z) + \eta\Big(\frac{1}{r}\partial_r r \partial_r + \frac{1}{r^2}\partial_\varphi^2\Big) v_z(r, \varphi) + f_z \,. \tag{A.3}$$

The nonlinear terms vanish identically. With the stress tensor in cylindrical coordinates (see e.g. Aris, 1989, p. 181) and with the normal vector $\mathbf{e}_r$, namely the basis vector in radial direction, we obtain the coordinates for the normal stress,

$$\begin{pmatrix} [\sigma\mathbf{N}]_r \\ [\sigma\mathbf{N}]_\varphi \\ [\sigma\mathbf{N}]_z \end{pmatrix} = \begin{pmatrix} -p & 0 & \eta\partial_r v_z \\ 0 & -p & \eta\partial_\varphi v_z/r \\ \eta\partial_r v_z & \eta\partial_\varphi v_z/r & -p \end{pmatrix} \begin{pmatrix} 1 \\ 0 \\ 0 \end{pmatrix} = \begin{pmatrix} -p \\ 0 \\ \eta\partial_r v_z \end{pmatrix} . \tag{A.4}$$

These lead to the following boundary conditions at the free surface,

$$-\,p(R, \varphi, z) = \gamma\kappa \,, \tag{A.5}$$

$$\eta\partial_r v_z(R, \varphi) = 0 \,. \tag{A.6}$$

Equation (A.5) is the normal projection of the stress balance, which we have found already in Section 1.1.4 as the Laplace–Young condition (1.15). Equation (A.6) is the perfect-slip condition (1.16 b). Equations (A.1) and (A.2) together with the boundary condition (A.5) determine the pressure to be constant

$$p(r, \varphi, z) = -\gamma\kappa = \frac{\gamma}{R} \,, \tag{A.7}$$

which causes also the term $\partial_z p$ in (A.3) to vanish because the radius of the cylinder does not depend on z. Therefore, already by construction, the flow cannot be driven by a pressure gradient, and only a body force f_z is able to generate a flow.

The symmetries of the three-dimensional problem have been chosen such that it reduces to a two-dimensional Poisson equation with mixed Neumann and Dirichlet boundary conditions

$$\Delta v_z(r, \varphi) = -f_z/\eta \quad \text{in the half circle} \,, \tag{A.8}$$

$$\partial_r v_z(R, \varphi) = 0 \quad \text{at the free surface} \,, \tag{A.9}$$

$$v_z(r, \varphi) = 0 \quad \text{at the substrate} \,, \tag{A.10}$$

where Δ denotes the Laplace-operator in two dimensions. By employing an image technique, the mixed boundary condition can be simplified to a pure Neumann boundary condition. We add a driving with opposite sign at the opposite half of the circle, as indicated in the right panel of Figure A.1. The solution is then given by the proper Green function together with the driving force,

$$v_z(\mathbf{x}) = -\frac{1}{2\pi}\int\limits_{B^+} \frac{f_z}{\eta} G(\mathbf{x}, \mathbf{x}')\, d\mathbf{x}' + \frac{1}{2\pi}\int\limits_{B^+} \frac{f_z}{\eta} G(\bar{\mathbf{x}}, \mathbf{x}')\, d\mathbf{x}' \,, \tag{A.11}$$

where the integration is performed only over the upper half of the circle. The point $\bar{\mathbf{x}}$ is given by reflection of the point $\mathbf{x}$ at the x-axis, see Figure A.1. The Green function consists of the usual logarithmic part for the free-space problem, and a term accounting for the boundary condition,

$$G(\mathbf{x},\mathbf{x}') = \ln(|\mathbf{x}-\mathbf{x}'|) + F(\mathbf{x},\mathbf{x}')\,. \tag{A.12}$$

The function F is determined by the Laplace equation

$$\Big(\frac{1}{r}\partial_r r \partial_r + \frac{1}{r^2}\partial_\varphi^2\Big) F(r,\varphi,r',\varphi') = 0\,, \tag{A.13}$$

with the boundary condition at $r = R$

$$\partial_r F(R,\varphi,r',\varphi') = \frac{1}{R} - \partial_r \ln(|\mathbf{x}-\mathbf{x}'|)\,. \tag{A.14}$$

The solution can be found with the aid of a Fourier series for the angular arguments of $\ln(|\mathbf{x}-\mathbf{x}'|)$ and by using an expansion of the Laplace equation (A.13) in Bessel functions.

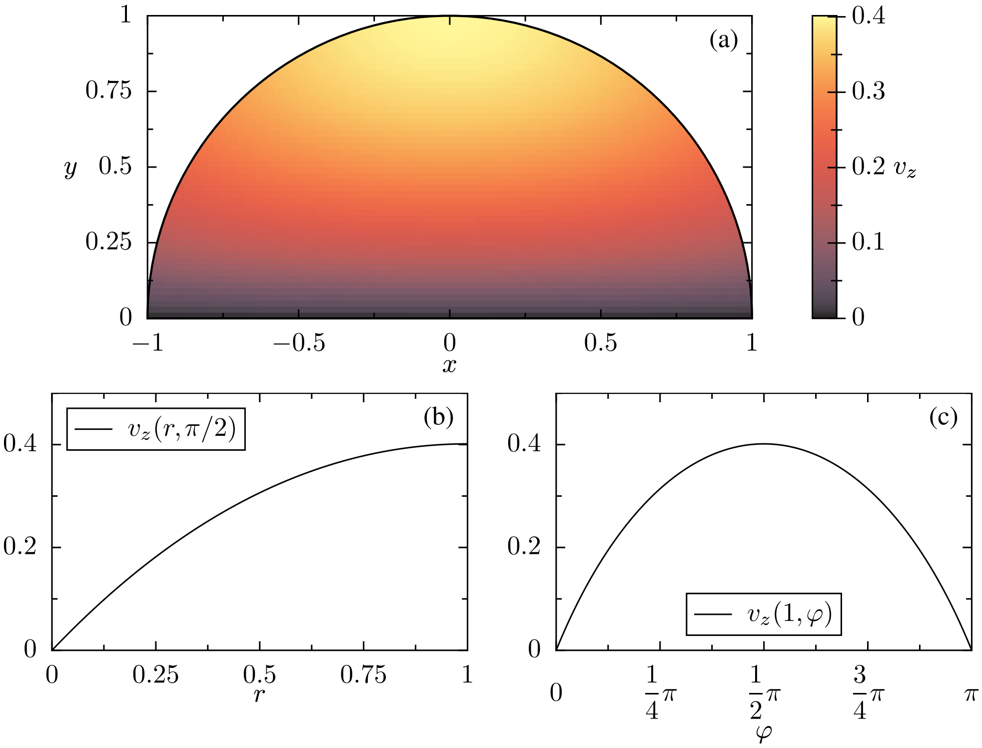

Figure A.2. The velocity profile in the half-cylinder geometry for $R = 1$ and $f_z/\eta = 1$. In panel (a) the function v_z is given in the x,y-plane. Panels (b) and (c) depict the velocity $v_z(r,\varphi)$ for selected values of φ and r. The free-surface boundary condition leads to the vanishing slope of the curve in (b) at $r = 1$.

We find for this part of the Green function,

$$\begin{aligned} F(r,\varphi,r',\varphi') &= -\sum_{n=1}^{\infty} \frac{1}{n}\Big(\frac{rr'}{R^2}\Big)^n \cos\big[n(\varphi-\varphi')\big] && \text{(A.15)} \\ &= \frac{1}{2}\ln\Big(1+\frac{r^2r'^2}{R^4}-2\frac{rr'}{R^2}\cos(\varphi-\varphi')\Big)\,. && \text{(A.16)} \end{aligned}$$

The integral in (A.11) then equates to the solution of the problem, namely

$$v_z(r,\varphi) = \frac{4f_z}{\pi\eta}r^2 \sum_{\substack{m=1 \\ m\ \text{odd}}}^{\infty} \frac{\sin(m\varphi)}{m(m^2-4)} - \frac{8f_z}{\pi\eta}R^2 \sum_{\substack{m=1 \\ m\ \text{odd}}}^{\infty} \Big(\frac{r}{R}\Big)^m \frac{\sin(m\varphi)}{m^2(m^2-4)}\,, \tag{A.17}$$

which is depicted in Figure A.2.

Appendix B.

Calculus of variations for the differential geometry of a surface

In order to prove equation (2.26), we express the change of the surface free-energy functional (2.21) by the change of the Jacobi determinant $\sqrt{a}$ of the surface parametrisation. With the infinitesimal surface area $dA = \sqrt{a}\, d\boldsymbol{\nu}$ the variation of the surface free-energy is given in terms of the variation of its parametrisation $\mathbf{t}$,

$$\delta F_{(\gamma)}[\delta \mathbf{t}] = \delta\Big(\int\limits_{A} \gamma \, dA \Big)[\delta \mathbf{t}] \tag{B.1}$$

$$= \int\limits_{E} \gamma \, \delta\big(\sqrt{a}\big)[\delta \mathbf{t}] \, d\boldsymbol{\nu} = \int\limits_{E} \gamma \, \frac{\partial \sqrt{a}}{\partial t^i_\alpha} \, \delta t^i_\alpha \, d\boldsymbol{\nu} \, . \tag{B.2}$$

This is a higher-dimensional variation problem. We vary the D functions t^i, which depend on $(D-1)$ independent variables. Our use of the covariant formulation appears to be the natural choice for the calculus of variations, see also the excellent survey by Lovelock and Rund (1975). The dependence of $\sqrt{a}$ on the tangential vectors follows from its definition as the determinant of the covariant entries of the surface metric tensor. For a two-dimensional surface, this reads

$$a = \begin{vmatrix} a_{11} & a_{12} \\ a_{21} & a_{22} \end{vmatrix} = \frac{1}{2} \epsilon^{\alpha\gamma} \epsilon^{\beta\delta} \, a_{\alpha\beta} \, a_{\gamma\delta} = \frac{1}{2} \epsilon^{\alpha\gamma} \epsilon^{\beta\delta} \, g_{ij} \, g_{kl} \, t^i_\alpha \, t^j_\beta \, t^k_\gamma \, t^l_\delta \, , \tag{B.3}$$

where $\epsilon^{\alpha\beta}$ is the permutation symbol in two dimensions,

$$\epsilon^{\alpha\beta} = \begin{cases} 0 & \alpha = \beta, \\ +1 & \alpha = 1 \text{ and } \beta = 2, \\ -1 & \alpha = 2 \text{ and } \beta = 1, \end{cases} \tag{B.4}$$

which is a relative surface tensor with weight $+1$. The absolute tensor results as

$$\varepsilon^{\alpha\beta} = \frac{\epsilon^{\alpha\beta}}{\sqrt{a}} \, . \tag{B.5}$$

This is analogous to the completely antisymmetric tensor in three dimensions, described in detail by Aris (1989). With the antisymmetric tensor we obtain the inverse of the surface metric tensor as

$$a^{\alpha\beta} = \varepsilon^{\alpha\gamma}\varepsilon^{\beta\delta}a_{\gamma\delta} \,. \tag{B.6}$$

A formal differentiation of (B.3) with respect to the surface parametrisation yields

$$\frac{\partial a}{\partial t^i_\alpha} = 2g_{ij}t^j_\beta\varepsilon^{\alpha\gamma}\varepsilon^{\beta\delta}a_{\gamma\delta} = 2a\, g_{ij}a^{\alpha\beta}t^j_\beta = 2a\, t^\alpha_i \quad \text{and} \tag{B.7}$$

$$\frac{\partial\sqrt{a}}{\partial t^i_\alpha} = \frac{1}{2\sqrt{a}}\frac{\partial a}{\partial t^i_\alpha} = \sqrt{a}\; g_{ij}a^{\alpha\beta}t^j_\beta = \sqrt{a}\; t^\alpha_i \,, \tag{B.8}$$

which can be inserted into (B.1) to give the desired result (2.26).

For a one-dimensional curve in two-dimensional space, the same formula (2.26) can be derived, but the notation may be somewhat confusing. Summation over the single surface index makes no sense. Nevertheless, we still have to distinguish between co- and contravariant relative tensors, i. e.,

$$a = a_{11} = g_{ij}t^i_1t^j_1 \,, \tag{B.9}$$

$$a^{11} = 1/a_{11} \quad \text{because} \quad a^{11}a_{11} = a^{\alpha\beta}a_{\alpha\beta} = 1 \,. \tag{B.10}$$

The formal derivative then becomes

$$\frac{\partial\sqrt{a}}{\partial t^i_1} = \frac{1}{2\sqrt{a}}2g_{ij}t^j_1 = \sqrt{a}\; g_{ij}t^j_1\frac{1}{a_{11}} = \sqrt{a}\; g_{ij}t^j_1a^{11} \,, \tag{B.11}$$

which completes the proof of (2.26) also for a one-dimensional surface.

It is important to note that in (B.2) we have differentiated only with respect to the covariant surface-vector t^i_α and not with respect to any other covariant surface-tensors of higher order. The first covariant surface-derivative is equivalent to a partial derivative, because the spatial components t^i of the parametrisation are scalars with respect to the surface coordinates, see (2.14). In case that a functional contains higher-order surface tensors, one has to pay attention to the difference between covariant derivatives and partial derivatives of t^i. Especially for the integration by parts over the surface, which leads from equation (2.26) to (2.30), this is of concern. For the integration by parts to be carried out, we need that the variation and the surface-derivative commute,

$$\delta(t^i_\alpha) = \delta(t^i_{,\alpha}) = (\delta t^i)_{,\alpha} \,. \tag{B.12}$$

For higher-order surface tensors, the variation and the surface-derivative do not commute. This can be seen from the definition of the covariant surface-derivative of a hybrid surface and space tensor, which *per se* contains the tangential vectors already in its derivative,

$$A^i_{\alpha,\beta} = \frac{\partial A^i_\alpha}{\nu^\beta} - \left\{ {\gamma \atop \alpha\,\beta} \right\} A^i_\gamma + \left\{ {i \atop j\,k} \right\} A^j_\alpha\, t^k_\beta \,. \tag{B.13}$$

The Christoffel symbols $\{\cdot\!\cdot\}$ are those of the surface and the embedding space, respectively. Thus, the variation does not commute with, for example, the second derivative of the surface parametrisation,

$$\delta(t^i_{,\alpha\beta}) = N^i N_j (\delta t^j)_{,\alpha\beta} - b_{\alpha\beta} t^i_\delta a^{\delta\gamma} \delta t^j_\gamma N_j \, . \tag{B.14}$$

For the first variations (2.27), (2.28), (2.56), and (2.58), as well as for the second variations (2.59) and (2.61) we need the variations of the inverse metric tensor of the surface, of the normal vector, and of a few other terms. They can all be calculated like the variation of the Jacobi determinant in (B.8). Here, we summarise the results,

$$\begin{aligned}
\delta a_{\alpha\beta} &= g_{ij}(\delta t^i_\alpha t^j_\beta + t^i_\alpha \delta t^j_\beta) \, , && \text{(B.15)}\\
\delta a &= 2a \delta t^i_\alpha t^\alpha_i \, , && \text{(B.16)}\\
\delta\sqrt{a} &= \sqrt{a}\, \delta t^i_\alpha t^\alpha_i \, , && \text{(B.17)}\\
\delta N_i &= -\delta t^j_\alpha t^\alpha_i N_j \, , && \text{(B.18)}\\
\delta(\sqrt{a}\, N_i) &= \sqrt{a} \left[N_i(\delta t^j_\alpha t^\alpha_j) - t^\alpha_i (\delta t^j_\alpha N_j) \right] , && \text{(B.19)}\\
\delta a^{\alpha\beta} &= \begin{cases} -2a^{\alpha\beta}\, \delta t^i_\delta\, t^\delta_i & \text{in 2D} \\ -2a^{\alpha\beta}\, \delta t^i_\delta\, t^\delta_i + \delta t^i_\gamma\, g_{ij}\, t^j_\delta (\varepsilon^{\alpha\gamma}\varepsilon^{\beta\delta} + \varepsilon^{\alpha\delta}\varepsilon^{\beta\gamma}) & \text{in 3D,} \end{cases} && \text{(B.20)}\\
&= -\delta t^i_\gamma (a^{\alpha\gamma} t^\beta_i + a^{\beta\gamma} t^\alpha_i) \, . && \text{(B.21)}
\end{aligned}$$

In the last identity, the fourth-order isotropic tensor $\varepsilon^{\alpha\gamma}\varepsilon^{\beta\delta}$ is expressed as a superposition of the only three possible isotropic tensors of fourth order,

$$\varepsilon^{\alpha\gamma}\varepsilon^{\beta\delta} = \lambda a^{\alpha\gamma} a^{\beta\delta} + \mu(a^{\alpha\beta} a^{\gamma\delta} + a^{\alpha\delta} a^{\beta\gamma}) + \nu(a^{\alpha\beta} a^{\gamma\delta} - a^{\alpha\delta} a^{\beta\gamma}) \, . \tag{B.22}$$

(Anti-)symmetry properties then determine the coefficients as $\lambda = \mu = 0$ and $\nu = 1$.

From equation (B.18) it follows that the normal projection $N_i \delta t^i_\alpha$ of the varied tangential vector does not vanish. If it did, the change of the normal vector due to changes of the tangential vectors would also vanish, which is impossible.

The following terms are needed for the second variation of $\sqrt{a}\, t^\alpha_i$,

$$\begin{aligned}
\delta(t^\alpha_i) &= \delta t^j_\beta (g_{ij} a^{\alpha\beta} - t^\beta_i t^\alpha_j - t^\gamma_i t_{j\gamma} a^{\alpha\beta}) \, , && \text{(B.23)}\\
\delta(\sqrt{a}\, t^\alpha_i) &= \sqrt{a}\, \delta t^j_\beta (N_i N_j a^{\alpha\beta} + t^\alpha_i t^\beta_j - t^\beta_i t^\alpha_j) \, . && \text{(B.24)}
\end{aligned}$$

Appendix C.

An implementation of the perfect-slip boundary conditions: a constraint method

The tangential components of the free-surface stress balance (1.11) correspond to the perfect-slip boundary condition (1.16 b). When this condition is expressed as a set of constraints for the DOFs, we obtain one equation like (2.77) for each DOF at the free surface. Because the derivatives of the second-order ansatz functions ϕ_d generally do not vanish at proximate nodes, the constraint equations contain non-vanishing weights for all DOFs that are located on the same element. As a result, the constraints for DOFs that are connected to two adjacent elements create dependencies of DOFs also on other elements. This is illustrated in Fig. C.1a. Consequently, all DOFs on the free surface depend on each other.

In order to avoid this full mutual dependence, we replace the constraint equation of the type (2.75) by the equation

$$u_d = w_d + \sum_{e \in \Lambda_d} w_{de} u_e + \sum_{e \in \overline{\Lambda}_d} w_{de} u_e^{(\mathrm{old})} \,, \tag{C.1}$$

where the sums run over two complementary sets Λ_d and $\overline{\Lambda}_d$. The DOFs in Λ_d contribute to the constraint for u_d in the usual way, while those in $\overline{\Lambda}_d$ have been substituted by their old values $u_e^{(\mathrm{old})}$ and thus contribute to the inhomogeneity. There is some freedom in the choice which of the participating DOFs in one element belong to Λ_d and which ones are taken into $\overline{\Lambda}_d$. We found that the combination illustrated in Figure C.1b works well: For the DOFs located at element vertices we take those DOFs which belong to adjacent nodes on the free surface as inhomogeneities; all other constraining DOFs are located at inner nodes and are not constrained. The DOFs located at second-order nodes on the free surface acquire their full constraints. When all constrained DOFs are expressed by non-constrained DOFs, then the resulting constraint equations will only contain DOFs that are located at inner nodes of three adjacent elements. This presents a sufficient decoupling of the constraint equations to yield an efficient algorithm.

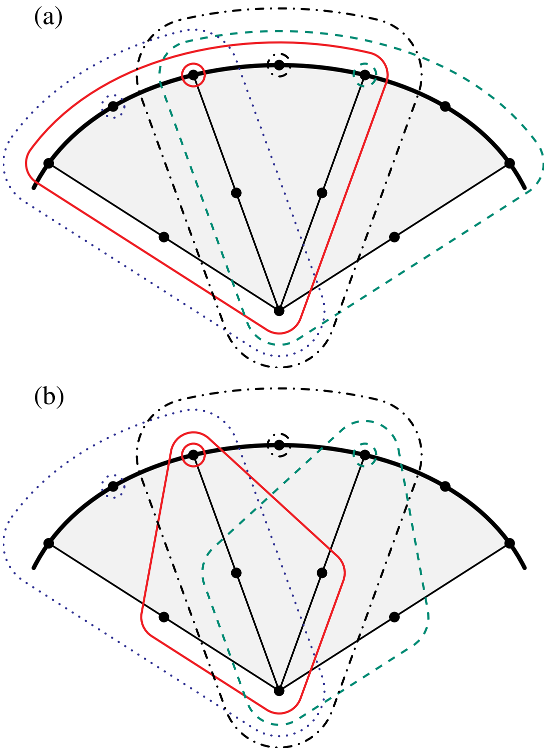

Figure C.1. A sketch of the dependencies among the DOFs located on three elements. The free surface is indicated by the thick curve. Constrained DOFs are surrounded by small circles. The nodes carrying the corresponding constraining DOFs are surrounded by curves drawn in the same style (solid and dashed for vertices; dotted and dash-dotted for second-order nodes). Panel (a) depicts the full mutual dependencies, while in (b) the DOFs located at vertices depend only on DOFs located at inner nodes. By taking in (b) the values of the missing adjacent DOFs located on the free surface as inhomogeneities rather than as constraints, the DOFs of adjacent elements become decoupled. The correct constraint equations are then established after some iteration steps.

Although the boundary condition given by equation (C.1) is not the correct one when the true velocity field has not yet been determined, it still improves as the velocity field approaches the solution. Thus, there is hope that the correct boundary condition is established by successive application of equation (C.1) using increasingly better values for the $u_e^{(\mathrm{old})}$. In numerical experiments, the scheme for splitting the cross-dependencies as illustrated in Figure C.1b turned out to be the only one that works. In the examples of Figures 2.12 and 2.13, it took about 20 iteration steps to establish the correct boundary condition from scratch, and 5 iteration steps to re-establish it after a change of the mesh. This could be readily observed, because after the first iteration step the velocity field exhibited oscillations at the boundary nodes that ceased during iteration.

In the channels of Figure 3.7, we employed a modification of the above described procedure. It turned out that the use of the old values $u_e^{(\mathrm{old})}$ took very long to converge, or did not converge to the correct result. A better choice was to take instead the velocity values of the constrained node itself. This velocity was transformed in order to utilise the same normal and the tangential components at both boundary nodes, thus accounting for the change of the surface shape between the adjacent node and the constrained one.

Appendix D.

Green functions for stationary Stokes flow

As in Chapter 3, the following equations are written in Cartesian coordinates with metric tensor δ_{ij}. We will write all indices in lower position and assume indices which occur twice in a term to be summed over.

D.1. Green functions for the inhomogeneous Stokes equations

The Green functions for the Stokes equations (1.4) and (1.6) are defined to express the pressure, velocity and stress as linear functionals of the externally applied body force field,

$$p(\mathbf{x}) = \int\limits_{\Omega} P_k(\mathbf{x},\mathbf{y}) f_k(\mathbf{y})\, dV(\mathbf{y})\,, \tag{D.1}$$

$$v_i(\mathbf{x}) = \int\limits_{\Omega} K_{ik}(\mathbf{x},\mathbf{y}) f_k(\mathbf{y})\, dV(\mathbf{y})\,, \tag{D.2}$$

$$\sigma_{ij}(\mathbf{x}) = \int\limits_{\Omega} T_{ijk}(\mathbf{x},\mathbf{y}) f_k(\mathbf{y})\, dV(\mathbf{y})\,. \tag{D.3}$$

If the fluid domain is unbounded ($\Omega = \mathbb{R}^3$) and if the flow vanishes at infinity, then the Green functions for the pressure and the velocity equal the fundamental solutions of the Stokes equations (Dhont, 1996),

$$\mathcal{P}_k(\mathbf{r}) = -\frac{1}{4\pi}\left(\frac{1}{r}\right)_{,k} = \frac{1}{4\pi}\frac{r_k}{r^3} \quad \text{and} \tag{D.4}$$

$$\mathcal{K}_{ik}(\mathbf{r}) = \frac{1}{8\pi\eta}\left(\frac{\delta_{ik}}{r} + \frac{r_i r_k}{r^3}\right), \tag{D.5}$$

which depend only on the difference vector $\mathbf{r}=\mathbf{x}-\mathbf{y}$. The absolute value of the vector $\mathbf{r}$ is denoted by r. From equations (D.4) and (D.5) we find the fundamental solution also for the stress tensor,

$$\mathcal{T}_{ijk}(\mathbf{r}) = -\frac{3}{4\pi}\frac{r_i r_j r_k}{r^5}\,. \tag{D.6}$$

The fundamental solutions satisfy the Stokes equations with a point-force located at the point $\mathbf{y}$,

$$\mathcal{K}_{ik,i} = 0\,, \tag{D.7}$$

$$\mathcal{P}_{k,i}(\mathbf{r}) - \eta\Delta\mathcal{K}_{ik}(\mathbf{r}) = \delta_{ik}\delta(\mathbf{r})\,. \tag{D.8}$$

One third of the delta function in equation (D.8) is contributed by the Green function of the pressure, while the other two thirds stem from the velocity. Integration over a small ball $B_\varepsilon(\mathbf{0})$ around the origin yields

$$\lim_{\varepsilon\to 0}\int\limits_{B_\varepsilon(\mathbf{0})} \mathcal{P}_{k,i}\,dV = \frac{1}{3}\delta_{ik}\,, \tag{D.9}$$

$$-\eta\lim_{\varepsilon\to 0}\int\limits_{B_\varepsilon(\mathbf{0})} \Delta\mathcal{K}_{ik}\,dV = \frac{2}{3}\delta_{ik}\,. \tag{D.10}$$

D.2. Green functions for the homogeneous Stokes equations

The *boundary integral method* expresses the homogeneous solution of the Stokes equations in terms of integrals over the domain boundary. It is based on the reciprocal identity (3.11) of the fundamental solutions, namely

$$0 = \frac{\partial}{\partial x_j}\left[\mathcal{K}_{ik}(\mathbf{x}-\mathbf{y})\sigma_{ij}(\mathbf{x}) - v_i(\mathbf{x})\mathcal{T}_{ijk}(\mathbf{x}-\mathbf{y})\right]\,.$$

This identity holds for points $\mathbf{x}\neq\mathbf{y}$.

For the analysis in equations (3.18)–(3.22), we require the integrals of the fundamental solutions for the velocity field and the stress over a spherical surface $S_R(\mathbf{0})$. The sphere is embedded in three dimensions and centred at the origin. Carrying out the integral of the fundamental solution $\mathcal{K}_{ik}$, we obtain different values, depending on the relation between y and R,

$$\begin{aligned}\oint\limits_{S_R(\mathbf{0})} \mathcal{K}_{ik}(\mathbf{x}-\mathbf{y})\,dA(\mathbf{x}) &= \frac{1}{8\pi\eta}\oint\limits_{S_R(\mathbf{0})}\Big(\frac{\delta_{ik}}{\|\mathbf{x}-\mathbf{y}\|} + \frac{(x_i-y_i)(x_k-y_k)}{\|\mathbf{x}-\mathbf{y}\|^3}\Big)\,dA(\mathbf{x}) \\ &= \frac{1}{8\pi\eta}\left[\delta_{ik}\left\{\begin{array}{c} 16\pi R/3 \\ 4\pi\frac{R^2}{y}\Big(1+\frac{1}{3}\frac{R^2}{y^2}\Big)\end{array}\right\} + \frac{y_i y_k}{y^2}\left\{\begin{array}{c} 0 \\ 4\pi\frac{R^2}{y}\Big(1-\frac{R^2}{y^2}\Big)\end{array}\right\}\right]\,.\end{aligned} \tag{D.11}$$

The upper values in the braces are valid for $y \leq R$ and the lower ones for $y > R$. This integral can be carried out in an appropriately rotated coordinate system, where one axis is aligned towards the point $\mathbf{y}$. The general case (D.11) then follows from the rotation back into the original coordinate system. The integral of the fundamental solution $\mathcal{T}_{ijk}$ over the same sphere reads

$$\oint\limits_{S_R(\mathbf{0})} \mathcal{T}_{ijk}(\mathbf{x}-\mathbf{y})\, dA(\mathbf{x}) = -\frac{3}{4\pi} \oint\limits_{S_R(\mathbf{0})} \frac{(x_i-y_i)(x_j-y_j)(x_k-y_k)}{\|\mathbf{x}-\mathbf{y}\|^5}\, dA(\mathbf{x})$$
$$= \Big(\delta_{ij}\frac{y_k}{y} + \delta_{ik}\frac{y_j}{y} + \delta_{jk}\frac{y_i}{y}\Big) \left\{ \begin{matrix} 0 \\ 1/2 \\ R^4/y^4 \end{matrix} \right\} - \frac{y_i y_j y_k}{y^3} \left\{ \begin{matrix} 0 \\ 1 \\ 5R^4/y^4 - 3R^2/y^2 \end{matrix} \right\} . \tag{D.12}$$

The values in the braces correspond to $y < R$, $y = R$, and $y > R$ from top to bottom.

For equations (3.20) and (3.22) we further need the Laplacians of the fundamental solutions $\mathcal{K}_{ik}$ and $\mathcal{T}_{ijk}$. For arguments $\mathbf{r} \neq \mathbf{0}$, they can be obtained directly by differentiation. The results are

$$\Delta\mathcal{K}_{ik}(\mathbf{r}) = \Delta\Big(\frac{r_i r_k}{r^3}\Big) = \frac{2}{r^3}\Big(\delta_{ik} - 3\frac{r_i r_k}{r^2}\Big)\,, \tag{D.13}$$
$$\Delta\mathcal{T}_{ijk}(\mathbf{r}) = -\frac{3}{4\pi}\Delta\Big(\frac{r_i r_j r_k}{r^5}\Big) = 2\Big(\frac{\delta_{ij} r_k}{r^5} + \frac{\delta_{ik} r_j}{r^5} + \frac{\delta_{jk} r_i}{r^5} - 5\frac{r_i r_j r_k}{r^7}\Big)\,. \tag{D.14}$$

For the special case that $\mathbf{y} = \mathbf{0}$, the following integrals can be carried out,

$$\oint\limits_{S_R(\mathbf{0})} \mathcal{K}_{ik}(\mathbf{x})\, N_j(\mathbf{x})\, dA(\mathbf{x}) = \frac{1}{8\pi\eta} \oint\limits_{S_R(\mathbf{0})} \Big(\frac{\delta_{ik} x_j}{R^2} + \frac{x_i x_j x_k}{R^4}\Big)\, dA(\mathbf{x}) = 0\,, \tag{D.15}$$
$$\oint\limits_{S_R(\mathbf{0})} \mathcal{T}_{ijk}(\mathbf{x})\, N_j(\mathbf{x})\, dA(\mathbf{x}) = -\frac{3}{4\pi} \oint\limits_{S_R(\mathbf{0})} \frac{x_i x_k}{R^4}\, dA(\mathbf{x}) = -\delta_{ik}\,, \tag{D.16}$$

where we have assumed the normal vector $\mathbf{N}$ to point out of the sphere $S_R(\mathbf{0})$.

We now carry out the integral of the right-hand side of equation (3.11) over a bounded domain Ω. In case that the closure $\overline{\Omega}$ does not contain the point $\mathbf{y}$, this integral can be cast into an integral over the boundary $\partial\Omega$, as has been done in Section 3.1.2 for equation (3.14).

In order to prove identity (3.15), which expresses the velocity inside Ω by the integral over the boundary $\partial\Omega$, we now consider a domain Ω, that does contain the point $\mathbf{y}$ in its interior $\overset{\circ}{\Omega}$. As the integrand possesses a singularity at this point, we must exclude a small ball around $\mathbf{y}$ from the integration. By transforming the integral over the volume into an integral over the whole boundary $\partial\Omega \cup S_\varepsilon(\mathbf{y})$, a contribution over a sphere with radius ε

is obtained,

$$0 = \oint_{\partial\Omega} \left[\mathcal{K}_{ik}(\mathbf{x}-\mathbf{y})\sigma_{ij}(\mathbf{x}) - v_i(\mathbf{x})\mathcal{T}_{ijk}(\mathbf{x}-\mathbf{y})\right] N_j(\mathbf{x})\, dA(\mathbf{x}) + \oint_{S_\varepsilon(\mathbf{y})} \left[\mathcal{K}_{ik}(\mathbf{x}-\mathbf{y})\sigma_{ij}(\mathbf{x}) - v_i(\mathbf{x})\mathcal{T}_{ijk}(\mathbf{x}-\mathbf{y})\right] N_j(\mathbf{x})\, dA(\mathbf{x})\,. \quad \text{(D.17)}$$

Note that here the normal vector $\mathbf{N}$ points into the sphere $S_\varepsilon(\mathbf{y})$. The last integral can be carried out using relations (D.15) and (D.16), thereby assuming that the velocity and the stress are analytic at the point $\mathbf{y}$. In the limit $\varepsilon \to 0$ the linear and the higher-order terms of the Taylor series

$$v_i(\mathbf{x}) = v_i(\mathbf{y}) + v_{i,l}(\mathbf{y})[x_l - y_l] + \frac{1}{2} v_{i,lm}(\mathbf{y})[x_l - y_l][x_m - y_m] + \cdots \quad \text{(D.18)}$$

$$\sigma_{ij}(\mathbf{x}) = \sigma_{ij}(\mathbf{y}) + \sigma_{ij,l}(\mathbf{y})[x_l - y_l] + \frac{1}{2} \sigma_{ij,lm}(\mathbf{y})[x_l - y_l][x_m - y_m] + \cdots \quad \text{(D.19)}$$

all vanish. Their integrals are of the type

$$\oint_{S_\varepsilon(\mathbf{0})} \mathcal{K}_{ik}(\mathbf{x})\, N_j(\mathbf{x}) \left[x_l x_m \cdots x_r\right] dA(\mathbf{x})\,, \quad \text{(D.20 a)}$$

$$\oint_{S_\varepsilon(\mathbf{0})} \mathcal{T}_{ijk}(\mathbf{x})\, N_j(\mathbf{x}) \left[x_l x_m \cdots x_r\right] dA(\mathbf{x})\,, \quad \text{(D.20 b)}$$

which result at least in a linear dependence on ε, when carried out. The limit $\varepsilon \to 0$ makes them vanish. Only the leading terms of the Taylor series remain. Then, the last integral of (D.17) consists of the terms

$$\lim_{\varepsilon\to 0} \oint_{S_\varepsilon(\mathbf{y})} \mathcal{K}_{ik}(\mathbf{x}-\mathbf{y})\sigma_{ij}(\mathbf{x})\, N_j(\mathbf{x})\, dA(\mathbf{x}) = \sigma_{ij}(\mathbf{y}) \lim_{\varepsilon\to 0} \oint_{S_\varepsilon(\mathbf{y})} \mathcal{K}_{ik}(\mathbf{x}-\mathbf{y})\, N_j(\mathbf{x})\, dA(\mathbf{x}) = 0\,, \quad \text{(D.21)}$$

$$\lim_{\varepsilon\to 0} \oint_{S_\varepsilon(\mathbf{y})} v_i(\mathbf{x})\mathcal{T}_{ijk}(\mathbf{x}-\mathbf{y})\, N_j(\mathbf{x})\, dA(\mathbf{x}) = v_i(\mathbf{y}) \lim_{\varepsilon\to 0} \oint_{S_\varepsilon(\mathbf{y})} \mathcal{T}_{ijk}(\mathbf{x}-\mathbf{y})\, N_j(\mathbf{x})\, dA(\mathbf{x}) = v_k(\mathbf{y})\,, \quad \text{(D.22)}$$

which have been evaluated with the use of equations (D.15) and (D.16). Inserting (D.21) and (D.22) into (D.17) concludes the proof of equation (3.15).

Bibliography

ABRAHAM, R., MARSDEN, J. E., AND RATIU, T. (1988). *Manifolds, Tensor Analysis, and Applications*. New York: Springer-Verlag.

AJDARI, A. (2000). Pumping liquids using asymmetric electrode arrays. *Phys. Rev. E* **61**, R45.

ARIS, R. (1989). *Vectors, Tensors, and the Basic Equations of Fluid Mechanics*. New York: Dover Publications.

ASTUMIAN, R. D. AND HÄNGGI, P. (2002). Brownian motors. *Physics Today 55*(11), 33–39.

BÄNSCH, E. (1998). *Numerical methods for the instationary Navier–Stokes equations with a free capillary surface*. Habilitation thesis, Albert-Ludwigs-Universität Freiburg, Freiburg.

BEHR, M. (2004). On the application of slip boundary condition on curved boundaries. *Int. J. Numer. Meth. Fluids* **45**, 43.

BENDER, C. M. AND ORSZAG, S. A. (1978). *Advanced Mathematical Methods for Scientists and Engineers*. New York: McGraw-Hill Publishing Company.

BRACKBILL, J. U., KOTHE, D. B., AND ZEMACH, C. (1992). A Continuum Method for Modeling Surface Tension. *J. Comput. Physics* **100**, 335.

BRAKKE, K. A. (1992). The Surface Evolver. *Experimental Mathematics* **1**, 141–165.

BRENNER, M. P. AND GUEYFFIER, D. (1999). On the bursting of viscous films. *Phys. Fluids* **11**, 737–739.

BRINKMANN, M. (2002). *Benetzung lateral strukturierter Oberflächen*. Ph.D. thesis, Universität Potsdam, Potsdam.

BRINKMANN, M. (2005). private communication.

BRONSTEIN, I. N., SEMENDJAJEW, K. A., MUSIOL, G., AND MÜHLIG, H. (1995). *Taschenbuch der Mathematik*. Thun, Frankfurt a. M.: Harri Deutsch.

BUSH, J. W. M. AND HU, D. L. (2006). Walking on water: Biolocomotion at the interface. *Ann. Rev. Fluid Mech.* **28**, 339–369.

CAPOVILLA, R., GUVEN, J., AND SANTIAGO, J. A. (2003). Deformations of the geometry of lipid vesicles. *J. Phys. A: Math. Gen.* **36**, 6281.

CAREY, G. F. AND ODEN, J. T. (1986). *Finite Elements: Fluid Mechanics*, Volume VI: Fluid Mechanics. Englewood Cliffs: Prentice Hall.

COHEN, I., BRENNER, M. P., EGGERS, J., AND NAGEL, S. R. (1999). Two fluid drop snap-off problem: Experiments and theory. *Phys. Rev. Lett.* **83**, 1147–1150.

CRANK, J. (1984). *Free and moving boundary problems*. Oxford: Clarendon Press.

CUVELIER, C. AND SCHULKES, R. M. S. (1990). Some numerical methods for the computation of capillary free boundaries governed by the Navier–Stokes equations. *SIAM Review* **32**, 355.

CUVELIER, C., SEGAL, A., AND VAN STEENHOVEN, A. A. (1986). *Finite Element Methods and Navier–Stokes Equations*. Dordrecht: D. Reidel.

DANIEL, S., CHAUDHURY, M. K., AND DE GENNES, P. G. (2005). Vibration-Actuated Drop Motion on Surfaces for Batch Microfluidic Processes. *Langmuir* **21**, 4240–4248.

DEVILLE, M. O., FISCHER, P. F., AND MUND, E. H. (2002). *High-Order Methods for Imcompressible Fluid Flow*. Cambridge: Cambridge University Press.

DHONT, J. K. G. (1996). *An Introduction to Dynamics of Colloids*. Amsterdam: Elsevier.

DIMITRAKOPOULOS, P. AND HIDGON, J. J. L. (1999). On the graviational displacement of three-dimensional fluid droplets from inclined solid surfaces. *J. Fluid Mech.* **395**, 181–209.

DOI, M. AND EDWARDS, S. F. (1986). *The Theory of Polymer Dynamics*. Oxford: Oxford University Press.

DOI, M. AND MAKINO, M. (2005a). Migration of twisted ribbon-like particles in simple shear flow. *Phys. Fluids* **17**, 103605.

DOI, M. AND MAKINO, M. (2005b). Sedimentation of particles of general shape. *Phys. Fluids* **17**, 043601.

DZIUK, G. (1991). An algorithm for evolutionary surfaces. *Numer. Math.* **58**, 603.

ECKART, C. (1948). Vortices and Streams Caused by Sound Waves. *Phys. Rev.* **73**, 68.

EGGERS, J. (1997). Nonlinear dynamics and breakup of free-surface flows. *Rev. Mod. Phys.* **69**, 865–929.

EICHHORN, R., REIMANN, P., AND HÄNGGI, P. (2002). Brownian Motion Exhibiting Absolute Negative Mobility. *Phys. Rev. Lett.* **88**, 190601.

EIJKEL, J. C. T. AND VAN DEN BERG, A. (2006). The promise of nanotechnology for separation devices – from a top-down approach to nature-inspired separation devices. *Electrophoresis* **27**, 677–685.

EINSTEIN, A. (1905). Über die von der molekularkinetischen Theorie der Wärme geforderte Bewegung von in ruhenden Flüssigkeiten suspendierten Teilchen. *Annalen der Physik* **17**, 549. Reprinted in Einstein and von Smoluchowki (2001).

EINSTEIN, A. AND VON SMOLUCHOWSKI, M. (2001). *Untersuchungen über die Theorie der Brownschen Bewegung. Abhandlung über die Brownsche Bewegung und verwandte Erscheinungen*. Number 199, 207 in Ostwalds Klassiker der exakten Wissenschaften (Reprint). Thun: Harri Deutsch.

FAXÉN, H. (1921). *Einwirkung der Gefässwände auf den Widerstand gegen die Bewegung einer kleinen Kugel in einer zähen Flüssigkeit*. Ph.D. thesis, Philosophische Fakultät in Uppsala, Uppsala.

FAXÉN, H. (1922). Der Widerstand gegen die Bewegung einer starren Kugel in einer zähen Flüssigkeit, die zwischen zwei parallelen ebenen Wänden eingeschlossen ist. *Annalen der Physik, Folge IV* **68**, 89–119.

FAXÉN, H. (1923). Die Bewegung einer starren Kugel längs der Achse eines mit zäher Flüssigkeit gefüllten Rohres. *Arkiv för matematik, astronomi o. fysik 17*(27), 1–28.

FINLAYSON, B. A. (1972). *The Method of Weighted Residuals and Variational Principles*. Number 87 in Mathematics in Science and Engineering. New York: Academic Press.

FRIEDMAN, A. (1982). *Variational principles and free-boundary problems*. New York: Wiley.

FROMMELT, T. AND WIXFORTH, A. (2006). *(in preparation)*.

GAMMAITONI, L., HÄNGGI, P., JUNG, P., AND MARCHESONI, F. (1998). Stochastic resonance. *Rev. Mod. Phys.* **70**, 223–287.

GANTNER, A., HOPPE, R. H. W., KÖSTER, D., SIEBERT, K. G., AND WIXFORTH, A. (2006). Numerical simulation of piezoelectrically agitated Surface Acoustic Waves on microfluidic biochips. *Computing and Visualization in Science* **(in press)**.

DE GENNES, P. G. (1985). Wetting: Statics and Dynamics. *Rev. Mod. Phys. 57*(3), 827–863.

DE GENNES, P. G. (1999). Mechanical selection of chiral crystals. *Europhys. Lett.* **46**, 827–831.

GORRE-TALINI, L., JEANJEAN, S., AND SILBERZAN, P. (1997). Sorting of Brownian particles by the pulsed application of an asymmetric potential. *Phys. Rev. E* **56**, 2025–2034.

GUTTENBERG, Z., MÜLLER, H., HABERMÜLLER, H., GEISBAUER, A., PIPPER, J., FELBEL, J., KIELPINSKI, M., SCRIBA, J., AND WIXFORTH, A. (2005). Planar chip device for PCR and hybridization with surface acoustic wave pump. *Lab on a Chip* **5**, 208.

GUTTENBERG, Z., RATHGEBER, A., KELLER, S., RÄDLER, J. O., WIXFORTH, A., KOSTUR, M., SCHINDLER, M., AND TALKNER, P. (2004). Flow profiling of a surface-acoustic-wave nanopump. *Phys. Rev. E* **70**, 056311.

GUVEN, J. (2004). Membrane geometry with auxiliary variables and quadratic constraints. *J. Phys. A: Math. Gen.* **37**, L313.

HADJICONSTANTINOU, N. G. AND PATERA, A. T. (2000). A variationally consistent finite element approach to the two-fluid internal contact-line problem. *Int. J. Numer. Meth. Fluids* **34**, 711–727.

HÄNGGI, P. AND MARCHESONI, F. (2005). 100 years of Brownian motion. *Chaos* **15**, 026101.

HÄNGGI, P., TALKNER, P., AND BORKOVEC, M. (1990). Reaction-rate theory: fifty years after Kramers. *Rev. Mod. Phys.* **62**, 251–341.

HAPPEL, J. AND BRENNER, H. (1991). *Low Reynolds Number Hydrodynamics*. Dordrecht: Kluwer Academic Publishers. 5. printing of second edition 1973.

VON HELMHOLTZ, H. (1869). Zur Theorie der stationären Ströme in reibenden Flüssigkeiten. *Verhandlungen des naturhistorisch-medicinischen Vereins zu Heidelberg* **V**, 1–7. reprinted in von Helmholtz (1882), p. 223–230.

VON HELMHOLTZ, H. (1882). *Wissenschaftliche Abhandlungen*, Volume 1. Leipzig: Barth.

HO, L. W. AND PATERA, A. T. (1991). Variational formulation of three-dimensional viscous free-surface flows: natural imposition of surface tension boundary conditions. *Int. J. Numer. Meth. Fluids* **13**, 691–698.

HU, D. L., CHAN, B., AND BUSH, J. W. M. (2003). The hydrodynamics of water strider locomotion. *Nature* **424**, 663–666.

HUANG, L. R., COX, E. C., AUSTIN, R. H., AND STURM, J. C. (2004). Continuous Particle Separation Through Deterministic Lateral Displacement. *Science* **304**, 987–990.

HUGHES, T. J. R., LIU, W. K., AND ZIMMERMANN, T. K. (1981). Lagrangian–Eulerian finite element formulation for incompressible viscous flows. *Comput. Meth. Appl. Mech. Engrg.* **29**, 329–349.

HUH, C. AND SCRIVEN, L. E. (1971). Hydrodynamic Model of Steady Movement of a Solid/Liquid/Fluid Contact Line. *J. Colloid Interf. Sci.* **35**, 85–101.

JOHN, K., BÄR, M., AND THIELE, U. (2005). Self-propelled running droplets on solid substrates driven by chemical reactions. *Eur. Phys. J. E* **18**, 183–199.

JÜLICHER, F., AJDARI, A., AND PROST, J. (1997). Modeling molecular motors. *Rev. Mod. Phys.* **69**, 1269.

KETTNER, C., REIMANN, P., HÄNGGI, P., AND MÜLLER, F. (2000). Drift ratchet. *Phys. Rev. E* **61**, 312–323.

KIM, S. AND KARILLA, S. J. (1991). *Microhydrodynamics: Principles and Selected Applications*. Boston: Butterworth–Heinemann.

KISTLER, S. F. AND SCRIVEN, L. E. (1983). Coating Flows. In J. R. A. Pearson (Ed.), *Computational analysis of polymer processing*, Chapter 8, pp. 243–299. Barking, Essex: Applied Science Publishers.

KOSTUR, M., SCHINDLER, M., TALKNER, P., AND HÄNGGI, P. (2006). Chiral separation in microflows. *Phys. Rev. Lett.* **96**, 014502.

KRAMERS, H. A. (1940). Brownian motion in a field of force and the diffusion model of chemical reactions. *Physica* **7**, 284.

LAFAURIE, B., NARDONE, C., SCARDOVELLI, R., ZALESKI, S., AND ZANETTI, G. (1994). Modelling merging and fragmentation in multiphase flows with SURFER. *J. Comput. Phys.* **113**, 134.

LAMB, H. (1932). *Hydrodynamics*. New York: Dover Publications.

LANDAU, L. D. AND LIFSCHITZ, E. M. (1966). *Hydrodynamik*. Berlin: Akademie Verlag.

LANDAU, L. D. AND LIFSCHITZ, E. M. (1971). *Lehrbuch der theoretischen Physik V: Statistische Physik*. Berlin: Akademie-Verlag.

LEGER, L. AND JOANNY, J. F. (1992). Liquid spreading. *Rep. Prog. Phys.* **55**, 431–486.

LOVELOCK, D. AND RUND, H. (1975). *Tensors, Differential Forms, and Variational Principles*. New York: Dover Publications.

MARQUET, C., BUGUIN, A., TALINI, L., AND SILBERZAN, P. (2002). Rectified Motion of Colloids in Asymmetrically Structured Channels. *Phys. Rev. Lett.* **88**, 168301.

MATTHIAS, S. (2002). Experimenteller Nachweis einer Drift-Ratsche. Diplomarbeit, Mathematisch-Naturwissenschaftlich-Technische Fakultät der Martin-Luther-Universität Halle, Halle.

MATTHIAS, S. AND MÜLLER, F. (2003). Asymmetric pores in a silicon membrane acting as massively parallel Brownian ratchets. *Nature* **424**, 53–57.

MEISTER, A. (1999). *Numerik linearer Gleichungssysteme*. Braunschweig: Vieweg.

MIYAZAKI, K. AND BEDEAUX, D. (1995). Brownian motion in a fluid in simple shear flow. *Physica A* **217**, 53.

MYSHKIS, A. D., BABSKII, V. G., KOPACHEVSKII, N. D., SLOBOZHANIN, L. A., AND TYUPTSOV, A. D. (1987). *Low-Gravity Fluid Mechanics*. Berlin: Springer-Verlag.

NOTZ, P. K., CHEN, A. U., AND BASARAN, O. A. (2001). Satellite drops: Unexpected dynamics and change of scaling during pinch-off. *Phys. Fluids* **13**, 549–552.

NYBORG, W. L. (1965). Acoustic Streaming. In W. P. Mason (Ed.), *Physical Acoustics, 2B: Properties of polymers and nonlinear acoustics*, pp. 265–331. New York: Academic Press.

OMURTAG, A. C., DUTTA, P., AND CHEVRAY, R. (1996). Attractors of finite-sized particles: An application to enhanced separation. *Phys. Fluids* **8**, 3212–3214.

OSEEN, C. W. (1913). Über den Gültigkeitsbereich der Stokesschen Widerstandsformel. *Arkiv f. mat., astr. o. fys. 9*(16), 1–15.

OSEEN, C. W. (1927). *Hydrodynamik*. Leipzig: Akademische Verlagsgesellschaft.

POPINET, S. AND ZALESKI, S. (1999). A front-tracking algorithm for accurate representation of surface tension. *Int. J. Numer. Meth. Fluids* **30**, 775.

POZRIKIDIS, C. (1989). A singularity method for unsteady linearized flow. *Phys. Fluids A* **1**, 1508.

POZRIKIDIS, C. (1992). *Boundary Integral and Singularity Methods for Linearized Viscous Flow*. Cambridge: Cambridge University Press.

PURCELL, E. M. (1977). Life at Low Reynolds Number. *Am. J. Phys. 45*(1), 3–11.

PURCELL, E. M. (1997). The Efficiency of Propulsion by a Rotating Flagellum. *P. Natl. Acad. Sci. USA* **94**, 11307–11311.

RATHGEBER, A., WASSERMEIER, M., AND WIXFORTH, A. (2005). Acoustic 'distributed source' mixing of smallest fluid volumes. *J. ASTM Int.* **2**, 6.

REIMANN, P. (2002). Brownian motors: noisy transport far from equilibrium. *Phys. Rep.* **361**, 57–265.

REIMANN, P. AND HÄNGGI, P. (2002). Introduction to the physics of Brownian motors. *Appl. Phys. A* **75**, 169–178.

RENARDY, Y. AND RENARDY, M. (2002). PROST: A parabolic reconstruction of surface tension for the volume-of-fluid method. *J. Comput. Phys.* **183**, 400.

RISKEN, H. (1984). *The Fokker–Planck equation*. Berlin: Springer-Verlag.

RUBÍ, J. M. AND BEDEAUX, D. (1988). Brownian Motion in a Fluid in Elongational Flow. *J. Stat. Phys.* **53**, 125.

SACKMANN, E. (2004). Mikromechanik der Zelle. *Physik Journal* **3**, 35–42.

SAITO, H. AND SCRIVEN, L. E. (1981). Study of Coating Flow by the Finite Element Method. *J. Comput. Phys.* **42**, 53.

SCHLAGBERGER, X. AND NETZ, R. R. (2005). Orientation of Elastic Rods in Homogeneous Stokes Flow. *Europhys. Lett.* **70**, 129.

SCHWARZ, H. R. (1986). *Numerische Mathematik*. Stuttgart: Teubner.

SCHWARZ, H. R. (1991). *Methode der finiten Elemente* (3. ed.). Stuttgart: Teubner.

SCRIVEN, L. E. (1960). Dynamics of a fluid interface. Equation of motion for Newtonian surface fluids. *Chem. Eng. Sci.* **12**, 98–108.

SEIFERT, U. (1997). Configurations of fluid membranes and vesicles. *Adv. Phys.* **46**, 13.

SHU, J.-J. AND CHWANG, A. T. (2001). Generalized fundamental solutions for unsteady viscous flow. *Phys. Rev. E* **63**, 051201.

SKALAK, R. (1970). Extensions of extremum principles for slow viscous flows. *J. Fluid Mech.* **42**, 527–548.

SMOLIANSKI, A. (2005). Finite-element/level-set/operator-splitting (FELSOS) approach for computing two-fluid unsteady flows with free moving interfaces. *Int. J. Num. Meth. Fluids* **48**, 231.

VON SMOLUCHOWSKI, M. (1906). Zur kinetischen Theorie der Brownschen Molekularbewegung und der Suspensionen. *Annalen der Physik, Folge IV* **21**, 756–780. Reprinted in Einstein and von Smoluchowki (2001).

SOLONNIKOV, V. A. (1995). On some free boundary problems for the Navier–Stokes equations with moving contact points and lines. *Math. Ann.* **302**, 743–772.

SQUIRES, T. M. AND QUAKE, S. R. (2005). Microfluidics: Fluid physics at the nanoliter scale. *Rev. Mod. Phys.* **77**, 977.

SRITHARAN, K., STROBL, C. J., SCHNEIDER, M. F., GUTTENBERG, Z., AND WIXFORTH, A. (2006). Acoustic mixing at low Reynolds numbers. *Appl. Phys. Lett.* **88**, 054102.

STABEN, M. E., ZINCHENKO, A. Z., AND DAVIS, R. H. (2003). Motion of a particle between two parallel plane walls in low-Reynolds-number Poiseuille flow. *Phys. Fluids* **15**, 1711.

STONE, H. A. AND KIM, S. (2001). Microfluidics: Basic Issues, Applications, and Challenges. *AIChE Journal* **47**, 1250–1254.

STONE, H. A., STROOCK, A. D., AND AJDARI, A. (2004). Engineering Flows in Small Devices: Microfluidics Toward a Lab-on-a-Chip. *Annu. Rev. Fluid Mech.* **36**, 381.

STROBL, C. J. (2001). Flüssigkeitstransport mit aktustischen Wellen auf Kristalloberflächen. Diplomarbeit, Fakultät für Physik der Ludwig-Maximilians-Universität, München.

STROBL, C. J., FROMMELT, T., GUTTENBERG, Z., AND WIXFORTH, A. (2006). Particle Separation in a SAW-driven microfluidic system with continuous flow. *(submitted)*.

STROBL, C. J., SCHÄFLEIN, C., BEIERLEIN, U., EBBECKE, J., AND WIXFORTH, A. (2004). Carbon nanotube alignment by surface acoustic waves. *Appl. Phys. Lett.* **85**, 1427.

STROOK, A. D., ISMAGILOV, R. F., STONE, H. A., AND WHITESIDES, G. M. (2003). Fluidic Ratchet Based on Marangoni–Bénard Convection. *Langmuir* **19**, 4358–4362.

SUTHERLAND, W. (1905). A dynamical theory of diffusion for non-electrolytes and the molecular mass of Albumin. *Philos. Mag. Ser. 6* **9**, 781.

TAYLOR, G. (1953). Dispersion of soluble matter in solvent flowing slowly through a tube. *P. Roy. Soc. Lond. A* **219**, 186.

THIELE, U. (2003). Open questions and promising new fields in dewetting. *Eur. Phys. J. E* **12**, 409.

WALKLEY, M. A., GASKELL, P. H., JIMACK, P. K., KELMANSON, M. A., AND SUMMERS, J. L. (2004). On the calculation of normals in free-surface problems. *Commun. Numer. Meth. Engng.* **20**, 343.

WIXFORTH, A., STROBL, C. J., GAUER, C., TOEGL, A., SCRIBA, J., AND GUTTENBERG, Z. (2004). Acoustic manipulation of small droplets. *Anal. Bioanal. Chem.* **379**, 982.

ZIENKIEWICZ, O. C. AND TAYLOR, R. L. (2000). *The Finite Element Method* (5 ed.), Volume 3: Fluid Dynamics. Oxford: Butterworth-Heinemann.

ZINCHENKO, A. Z., ROTHER, M. A., AND DAVIS, R. H. (1997). A novel boundary-integral algorithm for viscous interaction of deformable drops. *Phys. Fluids* **9**, 1070.

Acknowledgements

I would like to thank Prof. Dr. Peter Hänggi for giving me the possibility to work on the fascinating topic of microfluidics. His lively and dedicated manner of doing physics, and his attentive and supportive way of leading the group has always been encouraging for me. Being the first PhD student on the topic of microfluidics gave me the chance to learn not only the subject but also how to explore a scientific field. I am deeply grateful to Prof. Dr. Peter Talkner for supervising the present thesis. This work would have been impossible without his constant support. Discussing with him has always been a source of insight. In particular, I benefited from his profound knowledge in various fields of physics and from his dauntlessness concerning physical and mathematical difficulties.

I would also like to thank Prof. Dr. Achim Wixforth and Prof. Dr. Roland Netz for acting as referees for this thesis.

My special thanks go to our experimental partners Prof. Dr. Achim Wixforth, Thomas Frommelt, Christoph Strobl, and Dr. Matthias Schneider for the fruitful collaboration, the valuable discussions and for providing the experimental pictures for this thesis. For insight into current microfluidic topics I would like to thank Dr. Uwe Thiele and the organisers and participants of the summer school “Complex Motion in Fluids” at Krogerup Højskole, Denmark.

For the careful proof-reading of the present work I am indebted to Prof. Dr. Peter Talkner, Maximilian Schultz, Dr. Eric Lutz, Dr. Sigmund Kohler, Dr. Martijn Wubs, and Franz Kaiser. Their suggestions and complaints concerning language and clarity of the presentation surely have made the manuscript more readable.

During the last years, I much enjoyed the atmosphere among the former and present members of the “Theorie 1” group in Augsburg, especially with Jörg Lehmann, André Wobst, Martijn Wubs, Gert-Ludwig Ingold, Sigmund Kohler, Michael Straß, Gerhard Schmid, Marcin Kostur, Łukasz Machura, Ralf Utermann, and Roland Doll.

This work has been financed by the *Deutsche Forschungsgemeinschaft* by means of project B13 of the SFB 486 (“Manipulation von Materie auf der Nanometerskala”) and by means of the Graduiertenkolleg 283 (“Nichtlineare Probleme in Analysis, Geometrie und Physik”).

Publications

During the preparation time of the present thesis I (co)-authored the following publications:

- M. Schindler, P. Talkner, and P. Hänggi. *Firing Time Statistics for Driven Neuron Models: Analytic Expressions versus Numerics*. Phys. Rev. Lett. **93** (2004) 048102.
- Z. Guttenberg, A. Rathgeber, S. Keller, J. O. Rädler, A. Wixforth, M. Kostur, M. Schindler, and P. Talkner. *Flow profiling of a surface-acoustic-wave nanopump*. Phys. Rev. E **70** (2004) 056311.
- M. Schindler, P. Talkner, and P. Hänggi. *Escape rates in periodically driven Markov processes*. Physica A **351** (2005) 40.
- P. Talkner, L. Machura, M. Schindler, P. Hänggi, and J. Luczka. *Statistics of transition times, phase diffusion and synchronization in periodically driven bistable systems*. New J. Phys. **7** (2005) 14.
- M. Kostur, M. Schindler, P. Talkner, and P. Hänggi. *Chiral separation in microflows*. Phys. Rev. Lett. **96** (2006) 014502.
- M. Schindler, P. Talkner, and P. Hänggi. *Computing stationary free-surface shapes in microfluidics*. submitted to Physics of Fluids.
- M. Schindler, P. Talkner, and P. Hänggi. *Accumulating particles at the boundaries of a laminar flow*. in preparation
- M. Kostur, M. Schindler, P. Talkner, and P. Hänggi. *Neuron firing in driven nonlinear integrate and fire models*. in preparation.

Lebenslauf von Michael Schindler

Geburtsdatum:	13. Oktober 1976
Geburtsort:	Basel (Schweiz)
Familienstand:	ledig
Eltern:	Barbara Schindler, geb. Katzer (Apothekerin) und Hansgeorg Schindler (Professor für experimentelle Biophysik, gestorben am 28. August 2001)
Geschwister:	Thomas und Julia Schindler

1983 – 1987:	Besuch der Grundschule in Basel und in Linz
Sept. 1987 – Juni 1995:	Besuch des Gymnasiums in Linz
Okt. 1995 – Juli 1996:	*Studium Generale* am Leibniz Kolleg in Tübingen
Okt. 1995 – Juli 1998:	Grundstudium der Physik an der Eberhard-Karls-Universität Tübingen
Okt. 1998 – Nov. 2001:	Hauptstudium der Physik und Diplomarbeit an der Ludwig-Maximilians-Universität München
April 1999 – Nov. 2001:	Stipendiat der Friedrich-Ebert-Stiftung
Dez. 2001 – Okt. 2002:	Zivildienst in Berlin
Okt. 2002 – April 2006:	Wissenschaftlicher Mitarbeiter an der Universität Augsburg